MODIFICATION OF MESOPOROUS SILICAS

Shehla Altaf Sheikh

Submitted for the degree of Doctor of Philosophy

UNIVERSITY OF SOUTHAMPTON

Department of Chemistry

September 2000

UNIVERSITY OF SOUTHAMPTON

ABSTRACT

FACULTY OF SCIENCE

CHEMISTRY

Doctor of Philosophy

MODIFICATION OF MESOPOROUS SILICAS

by Shehla Altaf Sheikh

Mesoporous silicas were post-synthetically modified with organometallic complexes in order to produce well defined supported metal centres.

The first part of this thesis describes the synthesis of mesoporous silicas MCM-41(A), MCM-41(B) and AlMCM-41 using surfactant templates, MESLC using liquid crystal templates and KMES from an aged gel mixture. The mesoporous materials were characterised by a combination of methods (PXRD, IR spectrometry, MAS NMR, TEM and BET surface area measurements) which resulted in the identification of porous silicas with a hexagonal lattice of pores of 22 - 36 Å and internal surface areas of 848 - 1646 m^2g^{-1}.

The second part of this thesis describes the post-synthetic modification of mesoporous silicas with the organometallic species trimethylgallium, diethylzinc, Pd(allyl)cp, $Pd(CH_3CN)_2(NO_2)Cl$ and $Pd(PPh_3)_4$. MCM-41(A) was modified with trimethylgallium in a direct and indirect vapour phase reaction. MCM-41(B), KMES and MESLC were modified with trimethylgallium via vapour phase reactions. The interaction of trimethylgallium with mesoporous silicas was monitored by EXAFS and led to the loss of one methyl group and surface attachment of dimethylgallium via two silanol groups for MCM-41(A) at 100°C, and one silanol group for MCM-41(A), MCM-41(B) and KMES at 200°C, and via two silanol groups for MESLC at 200°C. The modification of MCM-41(A), MCM-41(B), KMES and MESLC by diethylzinc resulted in the loss of one ethyl group and interaction of the monoethylzinc species with the silica surface via three silanol groups for MCM-41(A), MCM-41(B) and KMES, and via two silanol groups for MESLC.

MCM-41(A), KMES and MESLC were modified by Pd(allyl)cp leading to the formation of Pd-cp subunits attached to the silica surface via two silanol groups for MCM-41(A) and KMES, and via one silanol group for MESLC. MCM-41(A) was also modified with $Pd(CH_3CN)_2(NO_2)Cl$ leading to the loss of two acetonitrile groups and the anchoring of a $Pd(NO_2)Cl$ subunit to the surface of the silica via two silanol groups. The addition of trimethylgallium at 100°C resulted in metallic palladium being deposited on the silica surface and some interaction between the trimethylgallium species and the silica surface as well.

MCM-41(A) was functionalized with the phosphine ligand tri(hydroxypropyl)phosphine. Characterisation showed the retention of a hexagonal lattice and the presence of a mixture of phosphorus environments. The functionalized silica was further reacted with $Pd(PPh_3)_4$ and studied by EXAFS.

Contents

Chapter One - Introduction

Chapter Two - Experimental Techniques

Chapter Three - Synthesis and Characterisation of Mesoporous Silicas

Chapter Four - Metal-alkyl Modified Mesoporous Silicas

Abbreviations

AAS	Atomic Absorption Spectroscopy
AlMCM-41	Aluminosilicate mesoporous silica
BET	Brunauer, Emmett and Teller method of measuring surface area
cp	Cyclopentadiene
EXAFS	Extended X-ray Absorption Fine Structure
IR	Infra-red
KMES	Mesoporous silica made according to the Klinowski method
LCOS	Laboratoire de Chimie Organometallique de Surface
MAS	Magic Angle Spinning
MCM-41(A)	Mesoporous silica made with surfactant $C_{12}H_{25}(CH_3)_3NCl$
MCM-41(B)	Mesoporous silica made with surfactant $C_{14}H_{29}(CH_3)_3NBr$
MESLC	Mesoporous silica made with liquid crystalline surfactants
NMR	Nuclear Magnetic Resonance
$Pd(PPh_3)_4$	Tetrakis(triphenylphosphine)palladium
PXRD	Powder X-ray Diffraction
TEM	Transmission Electron Microscopy
TMOS	Tetramethylorthosilicate
XAS	X-ray Absorption Spectroscopy
XRD	X-ray Diffraction

Acknowledgements

I would like to thank my supervisors, the late Dr Judith Corker for her advice and support during my time in Southampton and Prof John Evans for all his help and patience in the two years since.

Many thanks go to all my colleagues (past and present) in the Chemistry department for making my time there memorable, and all the various people who shared a lab with me during the course of my studies, especially, Kathryn, Richard and Clive as well as Julie, Darryl and Steven. Also a special thanks to all those of my friends in Southampton who shared the burden when I needed it; Rosie, Aasia, Sam, Bec and Lynn...thank you all.

There have been some very dark times in the last couple of years and without a certain group of people, things would have been much more difficult than they were, so I would especially like to thank Ghazala (for always pushing), Azhar (for holding her back), Karen S. (for the endless movies), Karen J. (for making sense), Allegra (for giving me space), Javed (for sorting out all my PC problems) and last but not by any means least, Suliman, who always manages to make me smile.

I would like to thank the EPSRC for funding me through the course of my studies.

Finally, I would like to thank my family for their continued love and support. Mum and dad, this one's for you.

CHAPTER ONE

Introduction

1.0 Introduction

This thesis describes the post-synthetic modification of mesoporous materials based on the MCM-41 family. The work covers the synthesis and characterisation of a range of mesoporous materials with varying internal surface areas and pore diameters, and then examines the modification of these materials with organometallic complexes via direct and indirect methods including vapour deposition and the use of phosphine linkers to attach the organometallic species. Mesoporous materials of the MCM-41 family were chosen as supports due to the wide range of pore sizes available (10-100 Å) and the large internal surface areas (750-1800 cm^2 g^{-1}). Although zeolites and other microporous structures have been much studied as support materials, the relatively new mesoporous materials have not been as exhaustively investigated. These materials have much potential to act as molecular sieves and as supports for shape-selective catalysis. The main objective of this work is to fully characterize the mesoporous structures using a range of techniques and to thoroughly investigate the environment around the metal centres in the modified supports. This chapter serves as an introduction to this field of chemistry and also reviews the background and current literature in this area of research.

1.1 Homogeneous and heterogenous catalysis

A catalyst can be defined as a substance which increases the rate at which equilibrium is reached in a given reaction by lowering the activation energy of the process without itself being consumed in the reaction. The two categories of catalysis, homogeneous and heterogenous, have both advantages and disadvantages. Homogeneous catalysis is defined as a system where the reactants are in the same phase as the catalysts and heterogeneous catalysis is where the reactants are in a different phase to the catalyst. Both types of catalysis are found in abundant use in the chemical industry where nearly all industrial chemicals are made using one form of catalyst or the other.

In homogeneous catalysis, catalysts are normally present as solutes in a liquid reaction mixture. Catalytic mechanisms are inferred from a range of indirect evidence and so the

mechanism of homogeneous catalysis is more accessible to detailed investigation than that of heterogeneous catalysis because the interpretation of rate data is easier. Species in solution are also easier to characterize than those on a surface.[1]

Homogeneous catalysis is attractive because it is often highly selective towards the formation of the required product. In large-scale industrial processes, homogeneous catalysts have an advantage when it comes to exothermic reactions as it is easier to dissipate from a solution than from the solid bed of a heterogeneous catalyst. Heterogeneous catalysts are used extensively in industry and have more economic impact than homogeneous catalysts do. This is due in part to the ease of separation of product from the catalyst in large-scale industrial processes. Another attractive advantage is that these solid catalysts are robust at high temperatures and therefore can work in a wide range of operating conditions.

Although structural studies are often performed on single crystal surfaces, practical catalysts are generally materials with high surface areas which may contain several different phases. If the bulk of a high surface area material serves as the catalyst, then it is known as a uniform catalyst. However, if the high surface area material simply acts as the support onto which the catalyst is deposited, this is known as a multiphasic catalyst.[2]

In homogeneous catalysis, the interaction of reagents and catalysts occurs readily but in heterogeneous catalysis, it is necessary to ensure that the reactive molecules achieve contact with catalytic sites. Conventional heterogeneous catalysts are supported on amorphous inorganic oxide surfaces[3] where there is an abundance of active sites due to the amorphous structure. Dense solids are unsuitable due to low surface areas, therefore materials with high surface areas such as silica gels are widely used as supports.

Silica gel is prepared from the acidification of silicates to produce $Si(OH)_4$ which rapidly forms a hydrated gel from which the adsorbed water is easily removed by heating. Viewed through an electron microscope, the texture can be seen to be a rough gravel bed with irregularly shaped voids between the interconnecting particles. There has been a lot of interest in immobilizing catalytic species onto supports such as these, but the main problem that researchers have experienced is the failure to reproduce selectivities and activities

comparable to homogeneous catalysts. Part of the problem is the amorphous structure of the support so it has become necessary to consider better defined supports.

Research into the development of new, highly selective heterogeneous catalysts for the oxidation of alkanes, alkenes and aromatic compounds has activated much industrial interest in recent years. Efforts have been made to immobilize known homogeneous catalysts onto solid supports such as silica, alumina and polymers[4] with the intent of combining the advantages of both homogeneous and heterogeneous systems and at the same time reducing the disadvantages of both. Many examples of this can be found in literature. Examples include the study by Cannon *et al*[5] on the catalytic reaction of nitric oxide with rhodium carbonyl species attached to silica surfaces, Eisen and Marks looked at the kinetics and mechanism of facile arene hydrogenation by organotin complexes supported on dehydrated γ-alumina,[6] and Tietze *et al*[7] considered polymer-bound palladium catalysed allylic substitution reactions. The higher selectivity of homogeneous systems together with the ease of separation and purification of the reactants, products and catalysts of the heterogeneous systems provides an attractive medium for new catalysts.[8] The ability of heterogeneous systems to work at higher temperatures is also a desirable characteristic as this would overcome the diffusional problems of the catalytic species incorporated in the system and would allow reactions with higher activation energies to take place.

Homogeneous catalysis has the smallest industrial use but the potential that zeolitic-type catalysts have, has aroused much interest. As molecular sieves are able to recognize and select molecules within 0.1 Å accuracy, the attention they have received over the last twenty-five years has increased immensely and new types of molecular sieves are being discovered regularly.

1.2 Microporous materials

Zeolites were recognized as a new group of minerals over 200 years ago. In 1756, Cronstedt discovered and characterized the first zeolite, stilbite, as a hydrated aluminosilicate with alkali metal and alkaline earth cations.[9] When this material was heated, gas bubbles were

released. Cronstedt therefore combined the Greek words for "boiling" (zeo - from *zein* - to boil) and "stone" (*lithos* - stone) to name this surprising material a zeolite. The discovery of these naturally occurring minerals was mainly only of geological interest and although several workers in the 1800s noticed the ability of minerals such as chabazite (a naturally occurring zeolite) to remove odours from air, it wasn't until the early twentieth century that zeolite science came of age.

In 1932, McBain selectively adsorbed molecules into zeolite and coined the phrase "molecular sieves". This lead to an increase in the awareness of the potential industrial use of zeolites, and when in the mid 1940s, Barrer demonstrated the separation of molecules with zeolites, the race was on to find the most efficient and useful zeolitic catalyst.

Zeolites are microporous materials and are examples of uniform catalysts containing large regular channels and cages which are defined by the crystal structure. They have the general formula $M_{x/n}(AlO_2)_x(SiO_2)_y.mH_2O$, where y is greater than x and are made up of a framework of Si and Al ions each co-ordinated to four oxygen atoms.[10] The charge on the aluminium ion is counterbalanced by a cation which is situated in the cages or channels of the framework. These cations are free to move and are exchangeable with other cations. The channel sizes are determined by the number of oxygen atoms in the ring. The channel system can be one, two or three dimensional, however, the two and three dimensional systems may not have intersecting channels. The opening in these channels vary from one form to the next but are typically between 3 Å and 10 Å. Zeolites are able to absorb molecules small enough to enter the channels through the openings and exclude larger ones. This ability has lead to their being called molecular sieves and this selectivity, together with the catalytic sites inside the cages provides a degree of control over catalytic reactions that is not possible with silica gels.

Many examples of natural and synthetic zeolitic structures are now known[11,12] but it was in the 1950s when a group at Union Carbide led by Milton synthesized Linde A that synthetic zeolites became of such interest. Linde A was subsequently used extensively as an adsorbent and ion exchanger replacing phosphates in detergents. Industrial use of zeolites[13] started in the 1960s with the replacement of cracking catalysts based on amorphous aluminosilicates and zeolites such as metal-doped Y-zeolite began to be used as bifunctional catalysts in the

field of hydrocracking.[14] The discovery of the synthetic zeolite ZSM-5 in the 1970s was a major breakthrough in zeolitic chemistry. The structure of ZSM-5 (figure 1.1) consists of a three dimensional channel system made up of ten tetrahedral atoms forming a straight channel system intersected by a sinusoidal channel system with pore diameters in the order of 5.4 Å. This zeolite proved to be highly acidic, extremely shape selective and this in turn lead to new petrochemical processes such as selectoforming, olefin oligomerization and dewaxing.[15,16]

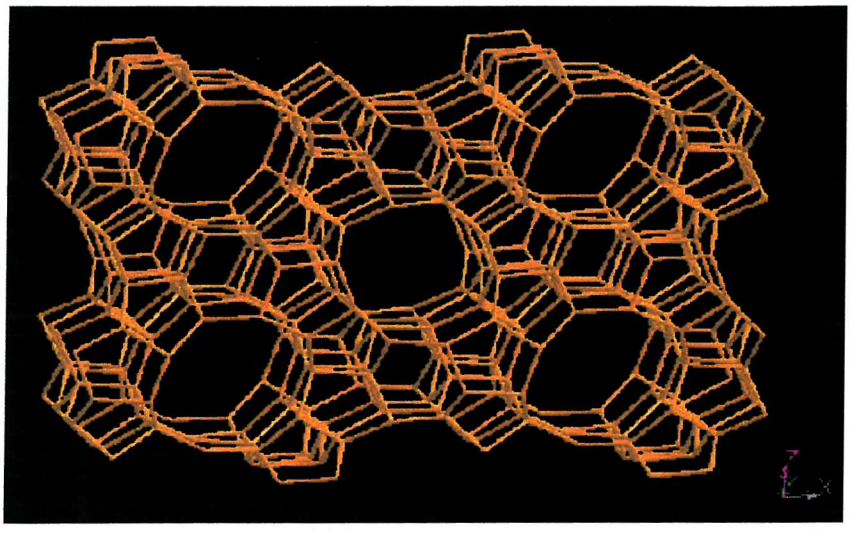

Figure 1.1 Zeolite ZSM-5

Having discovered that zeolites were fairly simple to synthesise and that they also had the advantage of being produced in a number of thermodynamically stable crystalline forms, they then began to be commercially exploited. In addition to aiding catalytic reactions, zeolitic materials have a wide variety of applications such as ion-exchange, the drying of organic compounds, the separation of hydrocarbons and the removal of species such as NH_3 and CS_2 from industrial gases. The three main commercial applications of zeolites exploits different aspects of zeolite structural chemistry:

Ion exchangers - the zeolite framework consists of Si and Al atoms connected by oxygen bridges. Changing the Si/Al ratio by the introduction of Al atoms into the framework

produces a charge imbalance due to the difference in the valence of Si and Al. This charge imbalance is countered by the introduction of mobile cations such as calcium or sodium. The presence of Al has the effect of introducing an electric field (making the zeolite more hydrophilic), introducing catalytic centres, enabling ion-exchange to take place and lowering the thermal stability of the zeolite.

Sorbents/molecular sieves - the zeolites offer hydrophylic or in siliceous materials, organophilic micropores of controlled dimensions and accessibilities. This allows diffusion of kinetically small molecules into the pores, absorption and under some conditions catalytic reactions to take place. A commercial example of this is seen in the sieving of straight- and branched-chain hydrocarbons to increase the octane number of gasoline.

Catalysis - zeolite materials provide highly active sites and the possibility of reaction outcomes being governed by shape selective constraints.

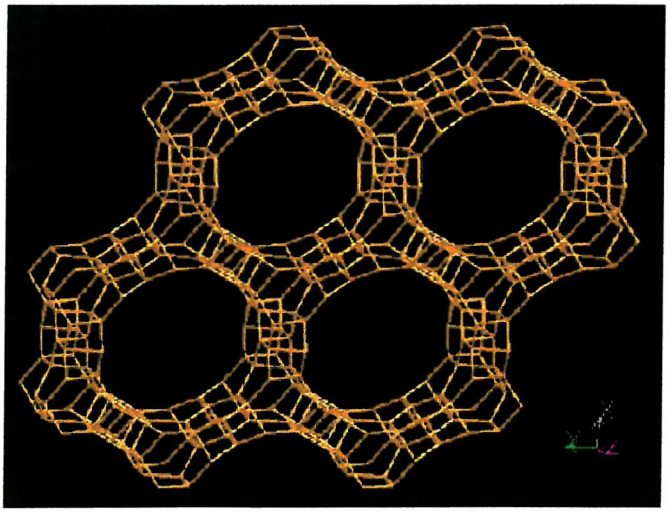

Figure 1.2 Zeolite VPI-5

After the discovery by Wilson *et al.*[17] in 1982 of the family of microporous aluminophosphates molecular sieves known as $ALPO_4$'s, many new families of microporous materials were quickly discovered. The $ALPO_4$'s, and subsequently SAPO's (silicoaluminophosphates), formed from the addition of silicon to the aluminium and phosphorus framework

elements, have been well studied and much literature is available. In most microporous materials the pore size is uniform, however, the distribution and channel dimensions are relatively small (<8 Å) which limits the diffusion of an organometallic species through the structure. The $ALPO_4$ molecular sieves have wider pore sizes and have channels ranging from 12-15 Å. For example, VPI-5 (figure 1.2), which is a member of the $ALPO_4$ family, contains rings of 18 tetrahedral atoms and consists of undimensional channels with free diameters of approximately 12 Å. Other $ALPO_4$'s with larger channels have been made but these materials seem to have limited stability. The ability to control the properties of these materials by controlling the synthetic pathways is vital to the continued industrial success of molecular sieves. As newer and newer materials with differing properties are discovered, the necessity for understanding how the zeolites are formed and how they interact with other chemicals increases.

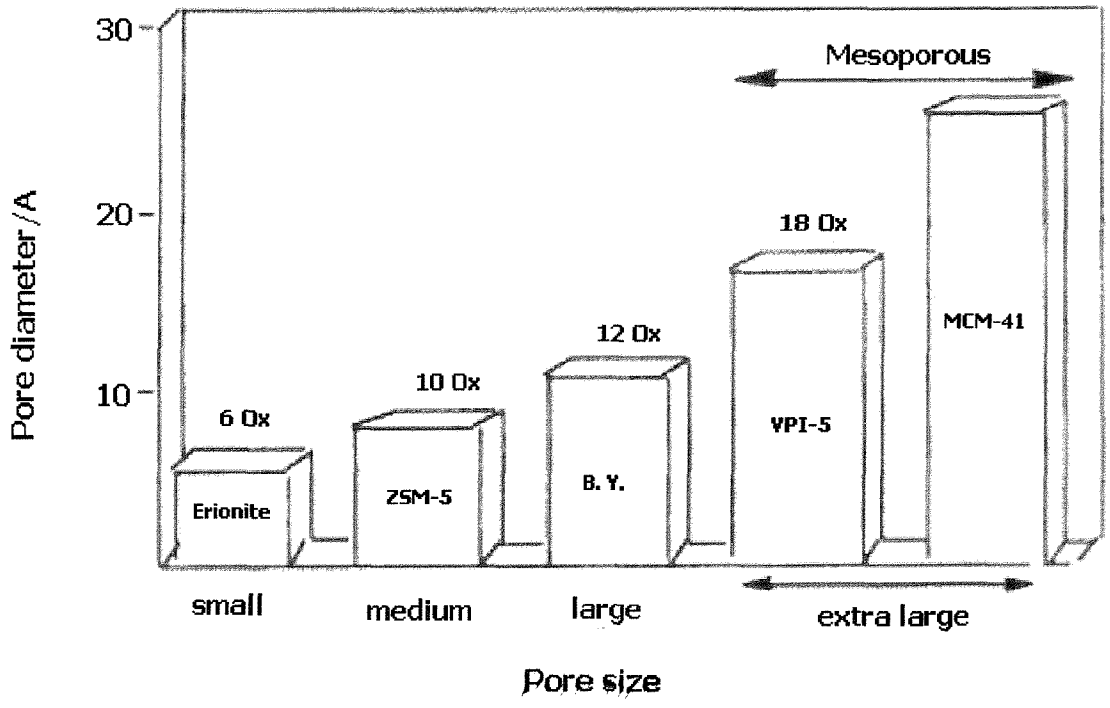

Figure 1.3 Zeolite classification by pore size.

Zeolite type materials tend to be classified according to their pore size. In recent years, the aim of many researchers has been to synthetically improve on nature and create bigger and

bigger structures which would enable more and faster industrial reactions to take place. Figure 1.3 depicts the classification of zeolite structures according to their pore size.[18] The early zeolites *e.g.* ZSM-5 had relatively small pore sizes with the pores made up of ten oxygen atoms compared to the more recent VPI-5 which has pores made up of eighteen oxygen atoms. Even larger than these are the new mesoporous range of silicas which are synthesised using surfactants as templating agents and have pores made up of more than twenty oxygen atoms depending on the length and size of the template.

1.3 Mesoporous materials

In 1992, a new family of well-defined mesoporous silicates and aluminosilicates were discovered.[19,20] These mesoporous structures, known as MCM-41 are thermally stable and have large uniform pores regularly arranged in a hexagonal array with pore-to-pore diameters ranging from 15 Å to 100 Å. These materials are amorphous with undirectional channels but contain internal silanol groups which would make them ideal for supporting catalytic organometallic species (figure 1.4).

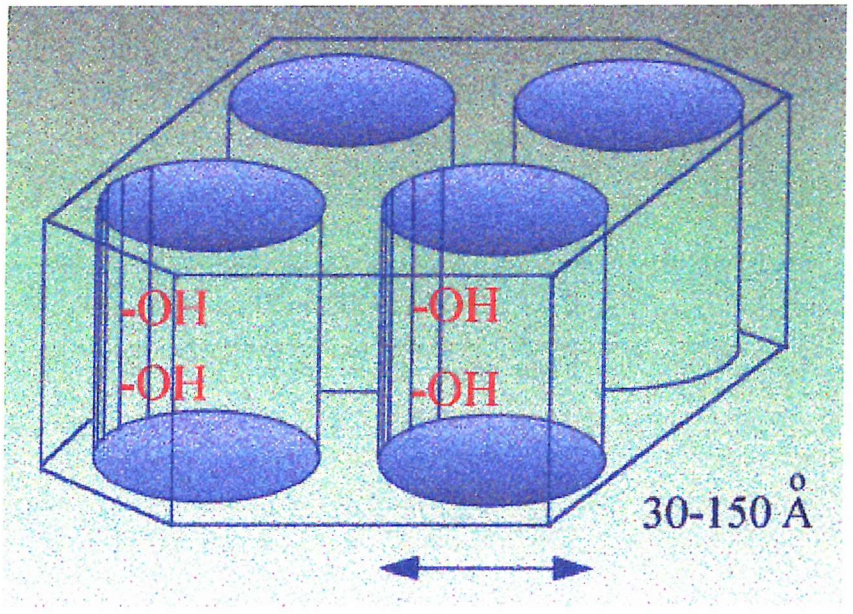

Figure 1.4 Channels of MCM-41 mesoporous silicas

Since the discovery of this family of silicas, the interest in their potential as catalytic supports has been intense. Schmidt *et al*[21] did a series of adsorption studies on MCM-41 model systems establishing reversible isotherm patterns for the materials and much is found in the literature about the synthesis of MCM-41 materials and their characterisation by various methods including XAS, NMR and microscopy.[22,23]

Over the years several alternative routes for the formation of mesoporous silicas have also been discovered. Attard *et al*[24] synthesised inorganic mesoporous silica by templating silica mesostructures from ordered liquid crystalline phases. The synthesis was quick, clean and resulted in a mesostructure of greater crystallinity than those of MCM-41. Mokaya *et al*[25] prepared large crystal MCM-41 silicas by using calcined small crystalline MCM-41 as seeds in a multistage synthesis method which resulted in thin films of mesoporous materials with thicker pore walls for greater thermal and hydrothermal stability.

Zhao *et al*[26] used a dip-coating technique to form continuous mesoporous silica thin films with three-dimensional accessible pore structures, and Yang *et al*[27] synthesised mesoporous silicas in quiescent aqueous acidic conditions. As the acidity is lowered, the growth process of the mesopores changes from a smooth continuous deposition of silicate-surfactant micellar solute species onto specific regions of the silicate liquid crystal seed to non-specific regions of the seed. The morphological control of ordered mesoporous silica by complete dissolution of both sodium metasilicate and cationic surfactants with rapid pH-adjustment to form mesoporous products was studied by Shio *et al*[28].

Improvements in the synthesis of mesoporous silicas have been suggested by various researchers using methods such as ozone treatment,[29] aqueous ammonia as a catalyst to form double mesopores[30] and the addition of cations such as tetraalkylammonium or sodium ions to the synthesis gel to improve hydrothermal stability.[31]

More recently, other new methods of forming mesoporous materials have been highlighted. Mokaya *et al*[32] described the two-step synthesis of large crystal MCM-41 via a seeded recrystallization route, and Kan *et al*[33] described the transformation of layered

aluminosilicates and gallosilicates with kanemite structures into mesoporous materials using exchange solutions.

One requirement of an industrial catalyst for the production of fine chemicals is to be as selective as possible. One way of achieving this is to specify the pore size in the catalytic material thus allowing only the desired reactant through the channels. This is however, very hard to achieve as a direct sythesis method but it is possible to modify the material after synthesis by incorporating an organometallic species within the structure thereby designing a catalyst which will selectively adsorb reacting molecules and will also influence the products by forcing steric constraints on the molecules.

Although these types of materials can impose shape selectivity during catalysis, most catalytic processes require specific pore geometries. By incorporating suitable organometallic species within a mesoporous material such as the MCM-41 family, it should potentially be possible to combine the advantages of heterogeneous catalysis with the higher selectivity of a homogeneous system and form a modified catalyst capable of selectively catalyzing alkene oxidation reactions.

1.4 Modification of mesoporous silicas

There are two main approaches to attaching metal complexes to solid supports. These are either via a direct reaction between the organometallic species and the surface of the support material or by initially functionalizing the support with phosphine or amine groups (see figures 1.5 and 1.6). Post-synthetic modification of mesoporous silicas by incorporating organometallic complexes within the porous volume can lead to active catalytic sites within the infrastructure of the silica without altering the coordination of the metal centre on deposition of the complex onto the support. This can result in hybrid catalysts with both heterogeneous and homogeneous properties.

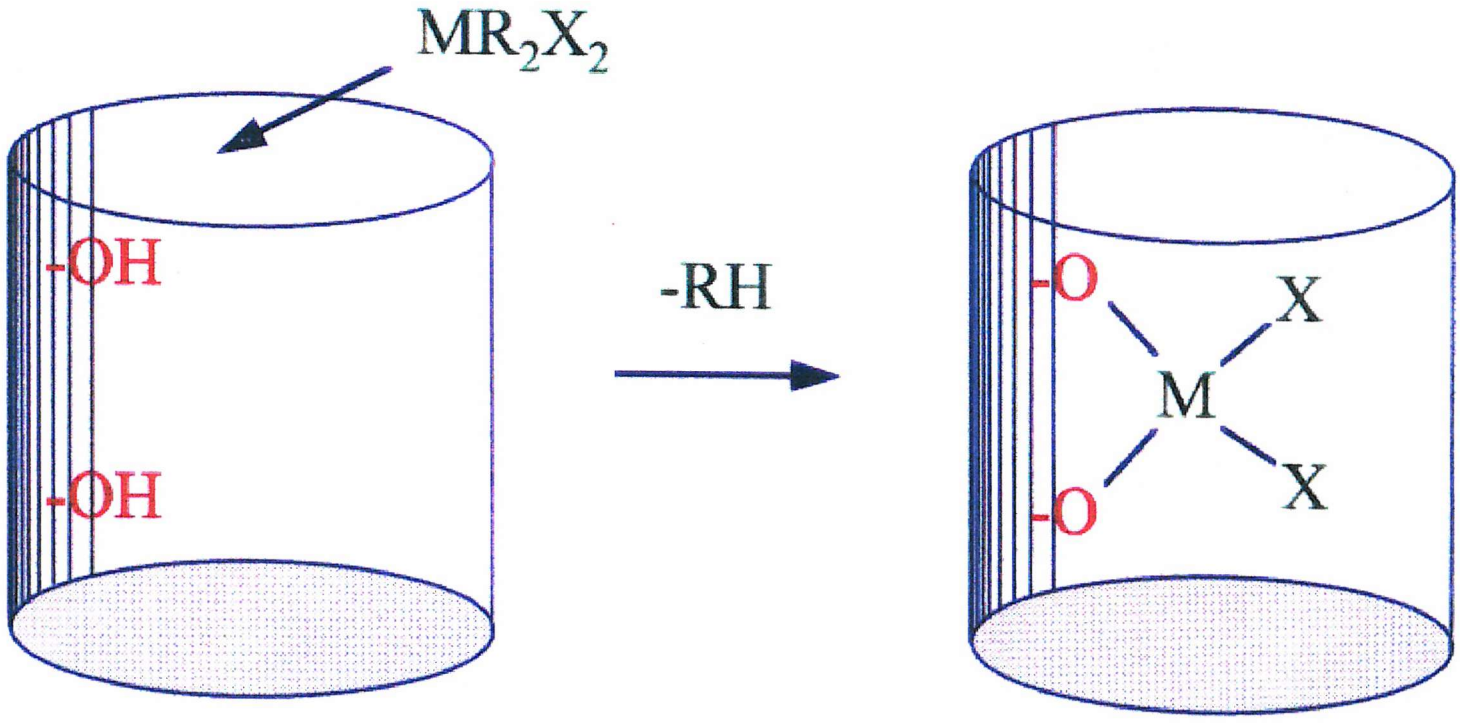

Figure 1.5 Direct reaction of metal centres with silanol groups

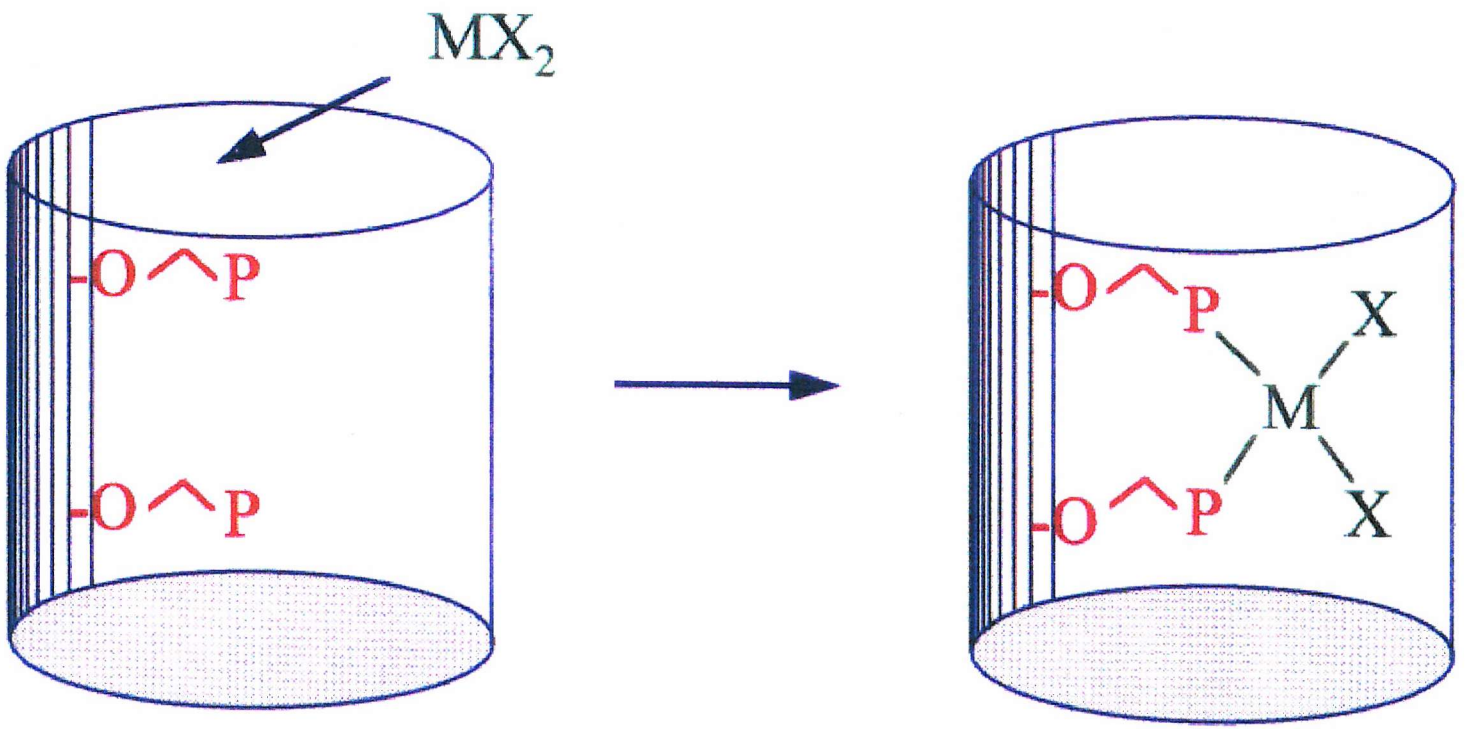

Figure 1.6 Reaction of metal complexes with phosphine functionalized silica

The formation of organometallic species within the mesoporous materials can be via one of three interactions; that of occluded species held within the pores of the silica by steric, electrostatic or chemical bonds; the formation of exchangeable cation species; and the incorporation of organometallic species within the framework of the silica structure.

Silica supported metals and metallic complexes catalyze many significant reactions such as olefin polymerization and styrene/propylene oxide syntheses. These compounds are made mainly via the direct reaction method. It is thought that although the catalyst supports do not take part in substrate transformations, they do contribute to the steric and electronic properties of the active metal centre.[34] The structure of these bound metal species have been investigated as the reactions occurring during synthesis are not well understood.

Meyer, Woerpel *et al*[35] found methods of directly attaching the complex $cp(PMe_3)(Ph)Ir$ to the silanol groups of silica and cleanly removing the complex by treatment with specific reagents so that the changes to its structural integrity could be monitored using homogeneous solution analytical methods. Another study by Nedez, Theolier *et al*[36] considered the reactivity of tetra-alkyltin complexes with the surface of high specific area silicas at low temperatures.

Since most transition metals form stable complexes with phosphines, bifunctional phosphines such as $Ph_2P(CH_2)_3Si(OEt)_3$ are often used as linkers. Phosphine complexes, prepared prior to the reaction with the silica, allows the metal/phosphine ratio to be controlled. This is, however, often difficult to achieve and an alternative method of modifying the surface of the silica with phosphine before adding the organometallic species is usually preferred.[37] Phosphine-functionalized silica-bound metal complexes have received a lot of interest over the years[38-40] and investigations into these species has mainly concentrated on spectroscopic techniques.

In research by Shyu *et al*[41], the organometallic catalyst $Rh(PPh_3)_3Cl$ was immobilized on MCM-41 silica previously modified with the anchoring ligand $(OEt)_3Si(CH_2)_3PPh_2$. This resulted in a stable hydrogenation catalyst with a turnover frequency three times higher than that of the catalyst alone in the hydrogenation of cyclohexene. The effect of molecular sieve

adsorption by organo-functionalised silica was investigated by Inumaru *et al*[42] who found that octylsilane-grafted on hexagonal mesoporous silica removed the low concentration endocrine disruptor nonylphenol from water with an efficiency comparable to that of activated carbon. Other areas of research have focused on the reactions of phenyl-functionalized microporous and mesoporous silica.[43] Sorption isotherms in these materials for *n*-butanol and *tert*-butanol were found to be stronger than those for water sorption studies. The study of Sorokin *et al*[44] concentrated on metallocyanine-functionilized silica by considering controlled procedures for anchoring iron tetraphthalocyanine onto amino-modified silicas. They were found to be selective for the oxidation of 2-methylnaphthalene to 2-methylnaphthoquinone and of 2,3,6-trimethylphenol to trimethylbenzoquinone.

In addition to these post-synthetic methods, some research has also focused on the incorporation of functionality at the synthetic level. Hall *et al*[45] synthesised organo-functionalized MCM-41 hexagonal silica mesophases and also phenyl-functionalized MCM-48 cubic silica mesophases containing binary combinations of covalently linked phenyl and amino, thiol or allyl moieties.

Mesoporous silica-supported metal complexes have potential as catalytically active species. The large pores and vast infrastructure of these materials also means that the metal complex is not only reacting with the surface but can be trapped within the channels thus increasing the number of catalytic sites and ultimately increasing the catalytic yield.

By chemically grafting a bulky organometallic species at the external surface or pore entrance of a zeolitic type material, the shape selectivity of the molecule can be adjusted. The steric hindrance provided by the organometallic fragment can be altered by altering the size of the organic section of the organometallic complex. Many examples of this type of modification to zeolites have been reported. One of the first examples of this approach to shape selectivity was by Theolier, Custodero *et al*[46] who grafted dineopentylmagnesium to the pore openings of mordenite. This was followed by many other studies of which rhodium complexes with *N*-chiral ligands anchored on USY zeolites[47] to increase enantioselectivity in the hydrogenation of *N*-acyldehydrophenylalanine derivatives and the confinement of buckminsterfullerene (C_{60}) in the one-dimensional channels of VPI-5[48] are just two examples.

To further support catalytically active metals, recent research has included replacing normal framework cations such as Si(IV), Al(III), Mg(II) and P(III) with transition metal cations such as Ti(IV)[49] to form layered silicate catalysts. This modifies the surface acidity and forms active catalysts for mild oxidations of organic molecules. The mesoporous MCM-41 materials have also become of interest in forming these hybrid catalysts as they bridge the gap between microporous (zeolites) and macroporous materials (*e.g.* amorphous aluminosilicates). However, to be catalytically active, this material has to incorporate metal ions. Investigations into the physical properties of the MCM-41 type materials have been intense[50,51] but the incorporation of metal ions or organometallic species in these materials needs to be studied further.

Incorporation of tetrahedral aluminium into the framework has been limited to a Si:Al ratio of 14:1. Schmidt, Akporiaye *et al*[52] synthesized a Si:Al ratio of 85:1 without observing any octahedral aluminium. Many examples of metals either incorporated into the framework or within the pores of MCM-41 materials can be found in the literature. One of the earliest examples was the immobilization of a highly thermostable trimethylstannyl molybdenum complex within the channels of the MCM-41 material followed by thermal transformation into supported metal clusters.[53]

More recent work has included investigations into the structural iron species in Fe-mesoporous silicas. Tuel *et al*[54] prepared a series of iron-containing mesoporous silicas with Fe contents of up to 5.7 wt.% using a neutral hexadecylamine surfactant. These materials were characterised by a combination of EXAFS, EPR and spectrophotometry which suggested that iron species were tetrahedrally co-ordinated to the non-calcined silica with calcination leading to 3-coordinate iron species which converted to 4-coordinate species in the presence of water. Another EXAFS study on mesoporous materials was that of Burch *et al*[55] who showed that manganese-oxo compounds anchored to the surface of mesoporous channels resulted in a material that was highly active for propene oxidation reactions.

Mesoporous materials such as the MCM-41 family have a number of attractive qualities which make them very suitable as support materials for organometallic complexes. They have a regular infrastructure of hexagonal channels with internal surface areas greater than

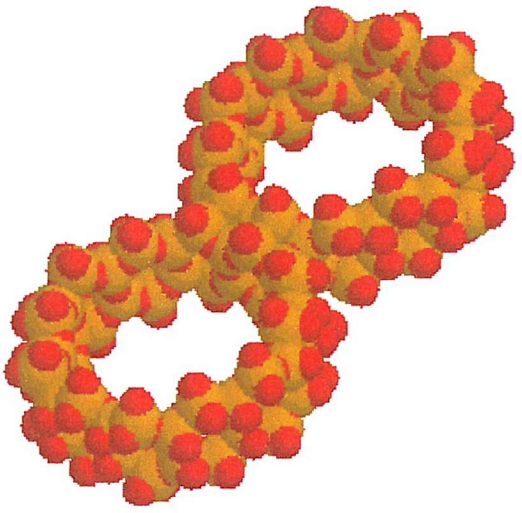

Figure 1.7 Space-filling model of two hexagonal channels of MCM-41. (Red = O, brown = Si)

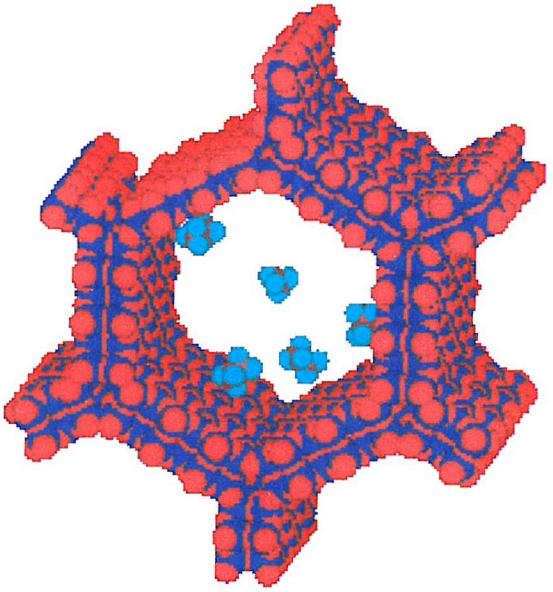

Figure 1.8 A space-filling model of methane and ethane inside a hexagonal pore of MCM-41. (Red = O, blue = Si, light blue = H, brown = C)

700 m^2g^{-1} which assumes the availability of a large number of active sites within the channels and pores. The MCM-41 silicas also have large well defined pores with diameters in the order of 15-100 Å as depicted in the space-filling model of the two hexagonal channels of MCM-41 (figure 1.7). The large pore size of the materials means that although small molecules such as methane and ethane can easily pass through the structure of the mesoporous silicas (see figure 1.8) with no hindrance, the porous volume is big enough to accommodate some very large molecules. This is one application where these types of mesoporous silicas have an advantage over smaller zeolites which cannot be used with large molecules for anything other than to exclude them. The large pores and channels also means that it would be possible for large bulky organometallic species to move into the silica structure and access more active sites within the channels.

1.5 Aims of this thesis

The aim of this work was to investigate the post-synthetic modification of mesoporous silicas with organometallic complexes with a view to forming stable anchored metallic centres. To achieve this aim, it was important to first study the various methods of synthesising mesoporous materials and then to fully characterise them. Thus this work falls into two main categories, the synthesis and characterisation of mesoporous silicas and the modification of mesoporous silicas via direct and indirect interaction with organometallic species.

Chapter three describes the synthesis of five mesoporous silicas, MCM-41(A), MCM-41(B), ALMCM-41 (synthesised using surfactant templates), KMES (synthesised from an aged gel mixture) and MESLC (synthesised using liquid crystal templates) followed by the full characterisation of each silica using a combination of PXRD, TEM, BET surface area measurements, IR spectrometry and NMR.

In chapter four, the modification of MCM-41(A) using a direct and vapour phase method for trimethylgallium and a vapour phase method for diethylzinc is described. The modifications were studied over a range of temperature conditions by continuous EXAFS and the analyses of this data is discussed in terms of model structures of the interaction of the organoalkyl

species with the surface of the mesoporous silicas. The interactions of trimethylgallium and diethyl zinc on the surface of mesoporous silicas MCM-41(B), MESLC and KMES were also investigated and the results of the interactions with all the different silicas are compared.

Chapter five describes the modification of MCM-41(A) with the organopalladium complexes Pd(allyl)cp and $Pd(CH_3CN)_2(NO_2)Cl$ using a direct and vapour phase method which was monitored by EXAFS over a range of temperature conditions and following the addition of a trimethylgallium species. This chapter also examines the potential of using trifunctional phosphine ligands such as $P(C_3H_6OH)_3$ to initially functionalize silica supports. The synthesis and characterisation of phosphine funtionalized MCM-41(A) is described and the subsequent reaction of the functionalized silica with the organopalladium complex $Pd(PPh_3)_4$ is discussed.

1.6 References

1. Shriver, D. F., Atkins, P. W., Langford, C. H., "Inorganic Chemistry", Oxford University Press, 1990, 1st Edition.
2. Thomas, J. M., *Angew. Chem. Int. Ed. Eng.*, 1988, **12**, 1673.
3. Snape, C., Affrossman, S., *Chemistry in Britain*, 1992, 1013.
4. Kawi, S., Chang, J.-R., Gates, B. C., *J. Am. Chem. Soc.*, 1993, **115**, 4830.
5. Cannon, K. C., Jo, S. K., White, J. M., *J. Am. Chem. Soc.*, 1989, **111**, 5064.
6. Eisen, M. S., Marks, T. J., *J. Am. Chem. Soc.*, 1992, **114**, 10358.
7. Tietze, L. F., Hippe, T., Steinmetz, A., *J. Chem. Soc. Chem. Commun.*, 1998, 793.
8. Ozin, G. A., Gil, C., *Chem. Rev.*, 1989, **89**, 1749.
9. Kokkotailo, G. T., Fyfe, C.A., *J. Phys. Chem. Solids*, 1989, **50**, 441.
10. Newsham, J. M., *Science*, 1986, **231**, 1093.
11. Davis M.. E., Lobo, R. F., *Chem. Mater.*, 1992, **4**, 756.
12. Suib, S. L., *Chem. Rev.*, 1993, **93**, 803.
13. Stiles, A. B., "Catalyst Supports and Supported Catalysts, Theoretical and Applied Concepts", Butterworths, 1987, 233.
14. Hoelderich, W., Hesse, M., Naemann, F., *Angew. Chem. Int. Ed. Eng.*, 1988, **27**, 226.
15. Parrillo, D. J., Gorte, R. J., Farneth, W. E., *J. Am. Chem. Soc.*, 1993, **115**, 12441.
16. Garcia, S. F., Weisz, P. B., *J. Catal.*, 1993, **144**, 109.
17. Wilson, S. T., Lok, B. M., Messina, C. A., Cannon, T. R., Flanigen, E. M., *J. Am. Chem. Soc.*, 1982, **104**, 1146.
18. Corma, A., Garcia, H., *J. Chem. Soc. Dalton Trans.*, 2000, 1381.
19. Beck, J. S., Vartuli, J. C., *J. Am. Chem. Soc.*, 1992, **114**, 10834.
20. Beck, J. S., Vartuli, J. C., US Patent 5108725, 1992.
21. Schmidt, R., Stocker, M., Hansen, E., Akporiaye, D., Ellestad, O. H., *Microporous Mater. 3*, 1995, 443.
22. Rey, F., Sankar, G. Maschmeyer, T., Thomas, J. M., Bell, R. G., *Topics in Catalysis*, 1996, 121.

23. Navrotzky, A., Petrovic, I., Hu, Y., Chen, C. Y., Davis, M. E., *Microporous Mater. 4*, 1995, 95.
24. Attard, G. S., Glyde, J. C., Goltner, C. G., *Nature, 1995,* **378**, 366.
25. Mokaya, R., Zhou, W. Z., Jones, W., *J. Chem. Soc., Chem. Commun.*, 1999, 51.
26. Zhao, D. Y., Yang, P. D., Margolese, D. I., Chmelka, B. F., Stucky, G. D., *J. Chem. Soc. Chem. Commun.* 1998, 2499.
27. Yang, H., Vovk, G., Coombs, N., Sokolove, I., Ozin, G. A., *J. Mater. Chem.*, 1998, **8**, 743.
28. Shio, S., Kimura, A., Yamaguchi, M., Yoshida, K., Kuroda, K., *J. Chem. Soc. Chem. Commun.*, 1998, 2461.
29. Keene, M. T. J., Denoyel, R., LLlewellyn, L., *J. Chem. Soc. Chem. Commun.*, 1998, 2203.
30. Wang, X. Z., Dou, T., Xiao, Y. Z., *J. Chem. Soc. Chem. Commun.*, 1998, 1035.
31. Das, D., Tsai, C. M., Cheng, S., *J. Chem. Soc. Chem. Commun.*, 1999, 473.
32. Mokaya, R., Zhou, W. Z., Jones, W., *J. Mater. Chem.*, 2000, **10**, 1139.
33. Kan, Q. B., Fornes, V., Rey, F., Corma, A., *J. Mater. Chem.*, 2000, **10**, 993.
34. Scott, S. L., Basset, J.-M., *J. Mol. Catal.*, 1994, **86**, 5.
35. Meyer, T. Y., Woerpel, K. A., Novak, B. M., Bergman, R. G., *J. Am. Chem. Soc.*, 1993, **115**, 722.
36. Nedez, C., Theolier, A., Lefebvre, F., Choplin, A., Basset, J.-M., Joly, J. F., *J. Am. Chem. Soc.*, 1993, **115**, 722.
37. Blumel, J., *Inorg. Chem.*, 1994, **33**, 5050.
38. Lindner, E., Kemmler, M., Mayer, H. A., Wegner, P. *J. Am. Chem. Soc.*, 1994, **116**, 348.
39. Alexier, V. D., Clayden, N. J., Cook, S. L., Dobson, C. N., Evans, J., Smith, D. J., *J. Chem. Soc. Chem. Commun.*, 1986, 938.
40. Champness, N. R., Levason, W., Oldroyd, R. D., Gulliver, D. J., *J. Organometallic Chem.*, 1994, 465, 275.
41. Shyu, S. G., Cheng, S. W., Tzon, D. L., *J. Chem. Soc. Chem. Commun.*, 1999, 2337.
42. Inumaru, K., Kiyoto, J., Yamanaka, S., *J. Chem. Soc. Chem. Commun.*, 2000, 903.

43. Bamborough, C. M., Slade, R. C. T., Williams, R. T., *Phys. Chem. Chem. Phys.*, 2000, **2**, 3499.

44. Sorokin, A. B., Tuel, A., *New J. Chem.*, 1999, **23**, 473.

45. Hall, S. R., Fowler, C. E., Lebeau, B., Mann, S., *J. Chem. Soc. Chem. Commun.*, 1999, 201.

46. Theolier, A., Custodero, E., Choplin, A., Basset, J.-M., Raatz, F., *Angew. Chem., Int. Ed. Engl.*, 1990, **29**, 805.

47. Corma, A., Iglesias, M., Pino, C., Sanchez, F., *J. Chem. Soc. Chem. Commun.*, 1991, 1255.

48. Anderson, M. W., Shi, J., Leigh, D. A., Moody, A. E., Wade, F. A., Hamilton, B., Carr, S. W., *J. Chem. Soc. Chem. Commun.*, 1993, 533

49. Luca, V., MacLachlan, D. J., Howe, R. F., Bramley, R., *J. Mater. Chem.*, 1995, **5**, 557.

50. Branton, P. J., Hall, P. G., Sing, K. S. W., Reichert, H., Schuth, F., Unger, K. K., *J. Chem. Soc. Faraday Trans.*, 1994, **90**, 2965.

51. Schmidt, R., Hansen, E. W., Stocker, M., Akporiaye, D., Ellestad, O. H., *J. Am. Chem. Soc.*, 1995, **117**, 4049.

52. Schmidt, R., Stocker, M., Akporiaye, D., Ellestad, O. H., *J. Chem. Soc. Chem. Commun.*, 1994, 1493.

53. Huber, C., Moller, K., Bein, T., *J. Chem. Soc. Chem. Commun.*, 1994, 2619.

54. Tuel, A., Arcon, I., Millet, J. M. M., *J. Chem. Soc., Faraday Trans.*, 1998, **94**, 3501.

55. Burch, R., Cruise, N. A., Gleeson, D., Tsang, S. C., *J. Mater. Chem.*, 1998, **8**, 227.

CHAPTER TWO

Experimental Techniques

2.0 Introduction

Complete characterisation of the mesoporous materials and the organometallic modified mesoporous materials requires a combination of experimental techniques. Due to the amorphous nature of the mesoporous materials, the techniques available to characterise them and the modified materials is limited. This chapter discusses the techniques involved in the characterisation of these materials which include MAS NMR spectroscopy, transmission electron microscopy, BET surface area measurements and EXAFS spectroscopy. Other techniques used to characterise the mesoporous and organometallic-modified mesoporous materials are detailed in Appendix 1.

2.1 MAS NMR Spectroscopy

Since the discovery of nuclear magnetic resonance by Bloch and Purcell in 1946, NMR spectroscopy has become one of the strongest tools for investigating molecular systems. The transition frequency of an atomic nucleus measured in an NMR experiment is a highly sensitive probe of the structural environment of that atom. Resolving the transitions of the nuclei provides unique information on the structure and dynamics of that system. However, a solid sample placed in this traditional NMR experiment would result in broad featureless lines. New NMR techniques developed in the 1970's allowed solid samples to be analysed by NMR spectroscopy with good spectral resolution.[1,2] High resolution solid state spectroscopy has since developed to the extent that the amount of information thus obtained is comparable to solution NMR spectroscopy.[3] However, solid state NMR spectroscopy is complicated due to several reasons. The NMR interactions which give chemical information are orientation dependent. This means that they vary with the angles linking the local nuclear environments to the applied magnetic field B_o, of the NMR experiment. The other complexity is due to the movement of molecules. In solution, molecules move rapidly at a fast enough rate that the NMR parameters are averaged to their isotropic values. In solids however, the motion of these molecules is restricted and therefore such averaging cannot take place to such a degree that would result in usable data. The spectrum is thus seen as a

broad line. Line broadening in the NMR spectra of solid samples can be attributed to dipolar coupling, chemical shift anisotropy and quadrupolar interactions.[1,4]

Dipolar coupling is caused by the dipole-dipole interaction of the magnetic moments of adjacent nuclei and is dependent on the size of the magnetic moments. The magnitude of dipolar coupling is inversely proportional to the internuclear distance and is not affected by the applied magnetic field B_0. Thus the NMR spectra of molecules with small internuclear distances such as ^{1}H-^{1}H or ^{13}C-^{1}H will be more strongly affected by dipolar coupling than molecules with larger internuclear distances such as ^{13}C-^{13}C or ^{29}Si-^{29}Si.

Chemical shift anisotropy, produced by the electronic charge distribution around the nucleus of the atom, is linearly proportional to the strength of the magnetic field B_0 and can result in line broadening up to 100 ppm.

The quadrupolar interaction occurs when the electric quadrupole moment of nuclei with spin quantum number $I > ½$, such as ^{27}Al and ^{17}O, interact with electric field gradient at the nucleus. This interaction ranges to several MHz and is dominant for most quadrupolar nuclei.

To obtain usable data from the NMR of solids, it is necessary to find an equivalent to the rapid motion of molecules in solution. The chemical shift anisotropy and dipolar coupling have an angular dependence of the form $\mathbf{3\cos^2\theta-1}$ where θ is the angle between the internuclear vector and the applied field. By spinning the bulk sample about an axis forming an angle where $\theta = 54.44°$ to the magnetic field B_0, all the anisotropy effects are removed and it is then possible to extract information from the NMR spectra. This angle is known as the magic angle and thus the technique is known as magic angle spinning (MAS) NMR (figure 2.1). In MAS NMR experiments, if the spinning rate is lower than the line width (in Hertz) of the static spectrum, a series of "spinning side bands", separated by the rotational frequency is seen flanking the central signal peak.

Line broadening can be further reduced by an experimental technique known as cross polarisation where the NMR signal of dilute spin nuclei is enhanced by the transfer of

polarisation from abundant spin nuclei such as ^1H. In solid state samples, the polarisation of dilute spin nuclei is altered using the dipolar coupling to abundant spin nuclei. Cross polarisation occurs via three steps: excitation of the abundant spin nuclei ($I > ½$) by a 90° pulse; transfer of polarisation from abundant spin nuclei to dilute spin nuclei (S) by simultaneously irradiating the radio frequency fields B_{1I} and B_{1S} of the I and S spins according to the Hartmann-Hahn condition $\gamma_I B_{1I} = \gamma_S B_{1S}$ (where γ_I and γ_S are the magnetogyric ratios of the nuclei I and S); and acquisition of the FID of the S spins with continued irradiation of the I spins for heteronuclear dipolar decoupling.

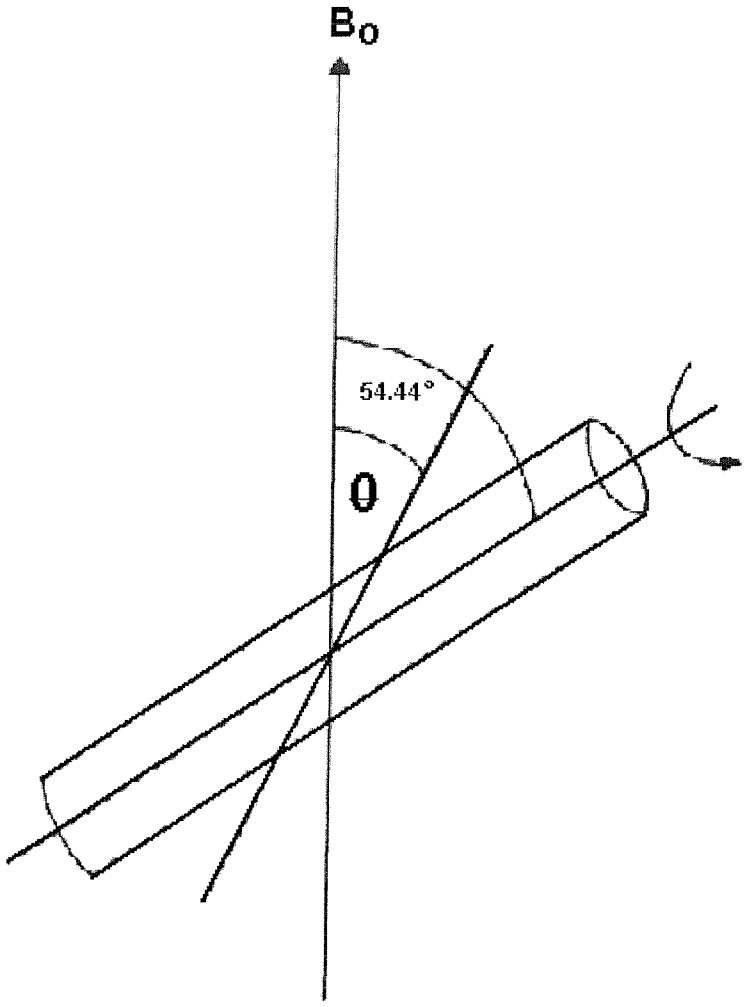

Figure 2.1 The magic angle 54.44°.

To achieve high resolution spectra with the optimum amount of line narrowing, in any particular NMR experiment, it may be necessary to use a combination of dipolar decoupling, magic angle spinning and cross-polarisation techniques.

MAS NMR is an important tool in the study of molecular sieve type materials and ^{29}Si, ^{31}P and ^{27}Al MAS NMR spectra obtained on the Bruker AM300 MHz NMR spectrometer were used to characterise the mesoporous materials and the organometallic modified supports. The samples, manipulated in a glove box, were finely ground and loaded into ZrO_2 rotors and spun at speeds of between 1-5.5 kHz.

2.2 Transmission Electron Microscopy

Transmission electron microscopy (TEM) is a sophisticated technique for magnifying images of very small objects by large amounts. It probes the internal structure of solids and gives access to microstructural or ultrastructural details which cannot be seen by the human eye.[8] An electron microscope uses lenses and condensers like a light microscope but has the advantage over a traditional light microscope by providing higher resolution, magnification, a greater depth of field and greater versatility.[9]

The image seen on a screen or on a photographic plate, is the result of two processes. The first is the interaction of the electron beam, the incoming wave function y_i, with the sample, the resultant interaction being y_o, the outgoing wave function. The second process is that of the interaction of the outgoing wave function with the microscope. In an ideal situation, the microscope would produce an enlarged image of the potential distribution in the sample, but as microscopes are aberrated optical systems, defocusing, astigmatism, spherical aberration and chromatic aberrations are present.

To understand the interaction of the electron beam with the sample it is necessary to first represent the potential seen by the electrons as:

$$V(r)=V(x,y,z)$$

If a sample is considered as consisting of several slices of thickness Δz, where z is the co-ordinate of the incoming electron beam, the motion of the beam consists of two stages: the propagation from the entrance surface, where the potential is zero to the exit of the sample; and transmission by the potential, assumed to be concentrated at the exit to the sample. Therefore, the incoming wave function $\psi_i(x,y,z)$ becomes:

$$\psi_i(x,y,z+\Delta z) = \psi_i(x,y,z) \times P_{\Delta z}(x,y)$$

where $P_{\Delta z}(x,y)$ is the free space propagator. The wave function, at the exit surface, is given by:

$$\psi_o(x,y,z+\Delta z) = \psi_i\text{-}(x,y,z+\Delta z)e^{-i\sigma Vp(x,y)}$$

where σ is the interaction constant and V_p is the projected potential of the sample. This gives an exit wave function of:

$$\psi_o(x,y,z+\Delta_z) = (\psi_i(x,y,z) \times P_{\Delta z}(x,y))e^{-i\sigma Vp(x,y)}$$

This is then considered as the input wave function for the second slice and the procedure is repeated.

The relationship between the wave function leaving the sample and the wave function after interaction with various lenses can be expressed as:

$$\psi_m(u,v) = \psi(u,v)T(u,v)$$

where ψ and ψ_m represents the Fourier transform of the wave function before and after the lenses respectively where u and v are spatial frequency variables and the function $T(u,v)$ is called the contrast transfer function factor and describes the effect of the microscope.

There are many techniques for digital image processing, most of which are based on a form of filtering. If the intensity of a micrograph is expressed as $I(x,y)$ then its Fourier transform is given by:

$$I(u,v) = \int_{-\mu}^{\mu} I(x,y) e^{-2\pi i(ux+vy)} dx dy$$

This is computed numerically by sampling I and using fast Fourier transform techniques. The filtering function S has values of:

$$S(u,v) = \{1 \text{ for } (u,v) \varepsilon \text{ a given region } R;\ 0 \text{ for } (u,v) \text{ outside } R\}$$

Filtering occurs by multiplying $I(u.v)$ by $S(u,v)$ and then performing an inverse Fourier transform to get the filtered image $I'(x,y)$ given by:

$$I'(x,y) = F^{-1}[I^{*}(u,v)S(u,v)]$$

where F^{-1} is the inverse Fourier transform. In practice, the electron micrograph is digitised and the digitised image is Fourier transformed. Filtering masks are designed to obstruct specific spatial frequencies removing noise and creating a contrast image. This picture can then be relayed to a screen.

In modern electron microscopes, the use of electromagnetic lenses and deflection coils means that it is possible to obtain images to a wide range of magnifications, (up to 1 000 000x), without physically changing or moving lenses.

Figure 2.2 shows a cross section of a typical, modern, transmission electron microscope. Early microscopes used one condenser lens as a collimator and one or two objective and projector lenses to magnify the image. A modern TEM consists of two condenser lenses which act as a collimator to control the electron beam before it reaches the sample, and four or five projector lenses to magnify the subsequent image. The system consists of five parts:

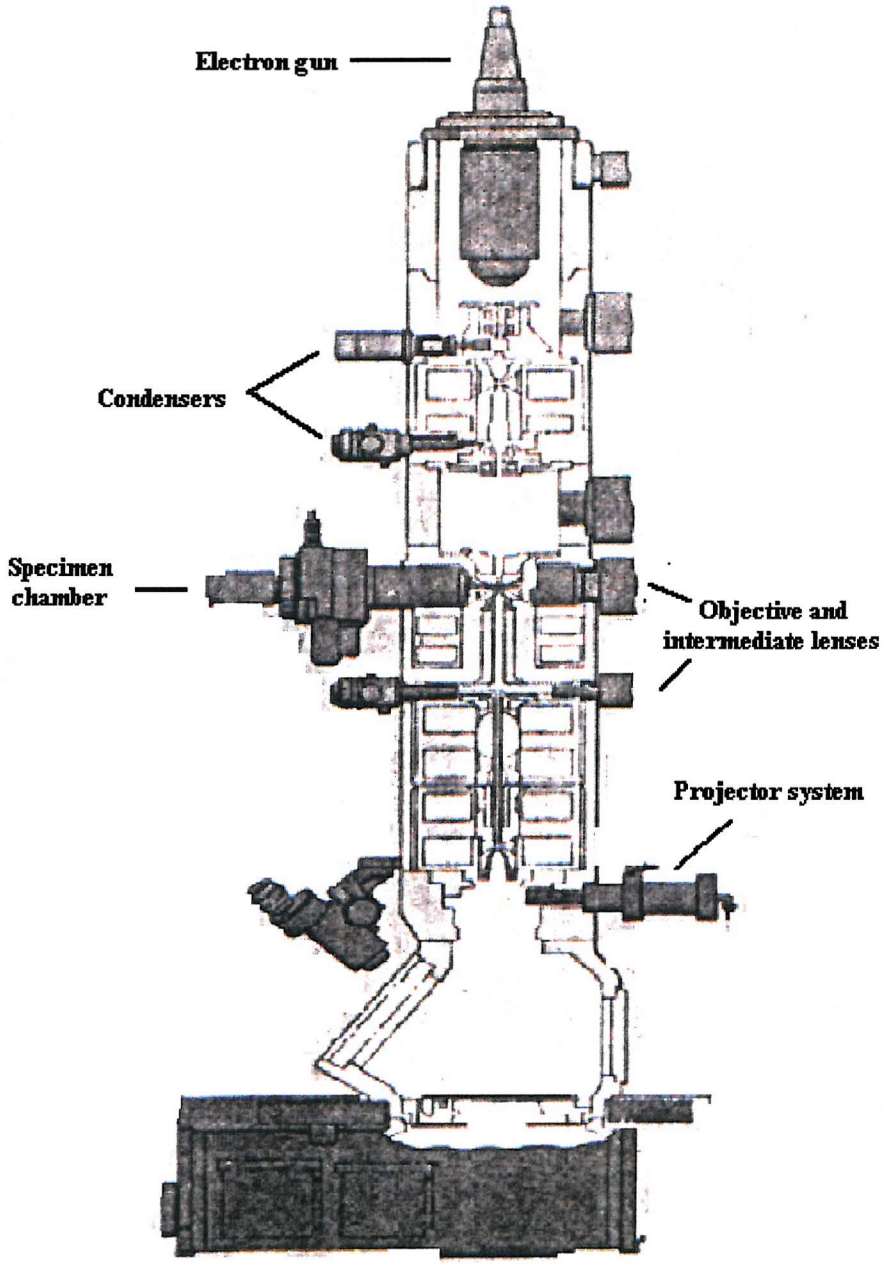

Figure 2.2 Schematic cross-section through a transmission electron microscope.

i) *The electron gun* is situated at the top of the instrument. This is a thermionic gun capable of accelerating the electrons through a selected potential in the range of 60 to 120 or 200 kV. The appropriate energy depends upon the nature of the sample and the required information. For a relatively thick sample or one which requires high resolution, using higher electron energies is a distinct advantage.

ii) *The condenser system* consisting of two or more condenser lenses, lies below the electron gun. Its main function is to demagnify the beam emitted by the gun and control its diameter and convergence angles as it hits the sample. The first condenser lens sets the demagnification of the gun crossover, the spot size, and the second lens gives direct control of the intensity of the spot size. This allows the operator to specify the area of the sample which is hit by the beam, thereby also controlling the intensity of the illumination.

iii) *The specimen chamber* lies below the condenser. A very small sample must be held in exactly the correct position but should also be able to be moved and be tilted by large amounts. This is very important so that the sample can be correctly orientated in the *x*,*y* and *z* directions for maximum effect.

iv) *The objective and intermediate lenses* are situated below the specimen chamber. The objective lens is usually so strong that the specimen sits within its pole pieces. This forms the first intermediate image which is enlarged by the projector lens and displayed on the screen. The magnification of the final image is controlled by the strength of this projector lens. An important aspect of the objective system is the aperture holder, which allows one of three or four small apertures to be inserted into the back focal planes of the column. This defines the angular range of scattered electrons which can travel down the column and add to the image. The diameter of the aperture controls the ultimate resolution (the larger the aperture, the higher the resolution) and also controls the contrast of the ensuing image.

v) *The projector system* controls the image magnification. The first image produced by the objective lenses usually has magnification of 50-100 times. This is then further magnified by a series of intermediate and projector lenses and is finally projected onto the fluorescent screen.

By using three or four lenses, each providing a magnification of up to twenty times, a total magnification of up to one million is easily achieved.

Transmission electron microscopy is an important technique for determining the hexagonal phase of mesoporous materials. Figure 2.3 shows a typical transmission micrograph of a mesoporous silica. Samples were prepared by coating carbon backed discs (5 mm diameter) with a suspension of the sample in a non-ionic medium and allowing to dry in a vacuum dessicator for a minimum of 24 hours. All TEM pictures were obtained on the JEOL 2000FX TEM operating at electron energies of 20-60 keV.

Figure 2.3 Typical TEM picture at 200 kV of energy and 120,000 magnification.

2.3 BET surface area measurements

The specific surface area of a powdered sample, *i.e.*, the surface area per gram of material, is a useful parameter, usually determined during the characterisation of a powder.[10] One of the most popular methods of determining this is that due to Brunauer, Emmett and Teller (BET),[11] giving rise to the name of the technique, BET surface area measurements. The principle of this method is that if the amount of gas covering the surface of a particular sample with a complete monolayer of adsorbate can be evaluated, then the surface area of the sample can be calculated if the area occupied by a single adsorbate molecule is known.

The BET equation is a theoretical description of the adsorption of a gas on a solid; how the amount of gas adsorbed v, an equivalent volume at standard temperature and pressure, varies with the equilibrium pressure p. The equation is expressed as:

$$\frac{p}{v(p_0-p)} = \frac{1}{v_m C} + \frac{C-1}{v_m C} \times \frac{p}{p_0}$$

where p_0 is the saturation vapour pressure of the adsorbate, v_m is the equivalent volume of gas at STP, and C is a constant characteristic of the system.

Most experimental systems can be described by the BET equation against a relative pressure range of 0.05 - 0.35 atm. Nitrogen gas is the most commonly used as the adsorbate at liquid nitrogen temperatures of 77.5 K. The area occupied by a single nitrogen molecule at this temperature is 16.2 Å.

Samples were prepared for BET surface area measurements by dehydrating the silica at a minimum temperature of 200°C under vacuum, and transferring to a sealed sample tube in a glove box. All BET surface area measurements were performed on a Micromeritics Gemini 2375 analyser. Samples were loaded into pre-weighed tubes under an argon flow and the surface area was measured relative to an empty tube at 77.5 K.

For each point designated for surface area calculations, the Gemini 2375 BET transformation is calculated as follows:

$$B_I = \frac{Pre1_I}{(1.0-Pre1_I)(Nads_I)}$$

where B_I represents the units of g cm^{-1} at STP, $Pre1_I$ is the relative pressure adsorbed after equilibrating the I^{th} dose (cm^3 STP), and $Nads_I$ represents the amount of gas adsorbed. A least squares fit is performed on the designated pairs (B_I, $Pre1_I$) where B_I is the dependent variable and $Pre1_I$ is the independent variable. The Gemini 2375 allows calculations of:

- slope (S g cm^{-1} STP)
- Y-intercept (Y_{INT} g cm^{-1} STP)
- Error of the slope (S_{err} g cm^{-1} STP)
- Correlation coefficient (C_c)

Using the results of the above calculations, the BET surface area (m^2g^{-1}) can be calculated:

$$SA_{BET} = \frac{(CSA)(6.023x10^{23})}{(22414\ cm^3\ STP)(10^{18}\ nm^2m^2)(S+Y_{INT})}$$

where CSA is the analysis gas molecular cross-sectional area (nm^2).

Figure 2.4 shows a schematic diagram of the Gemini 2375. The gas enters the system and is admitted into two reservoirs, the sample reservoir and the balance reservoir. From there it travels into the sample and balance tubes. The flow of the gas through the system is controlled by three transducers and a series of valves. An example of a data printout from the Gemini 2375 for an mesoporous material can be found in Appendix 2.

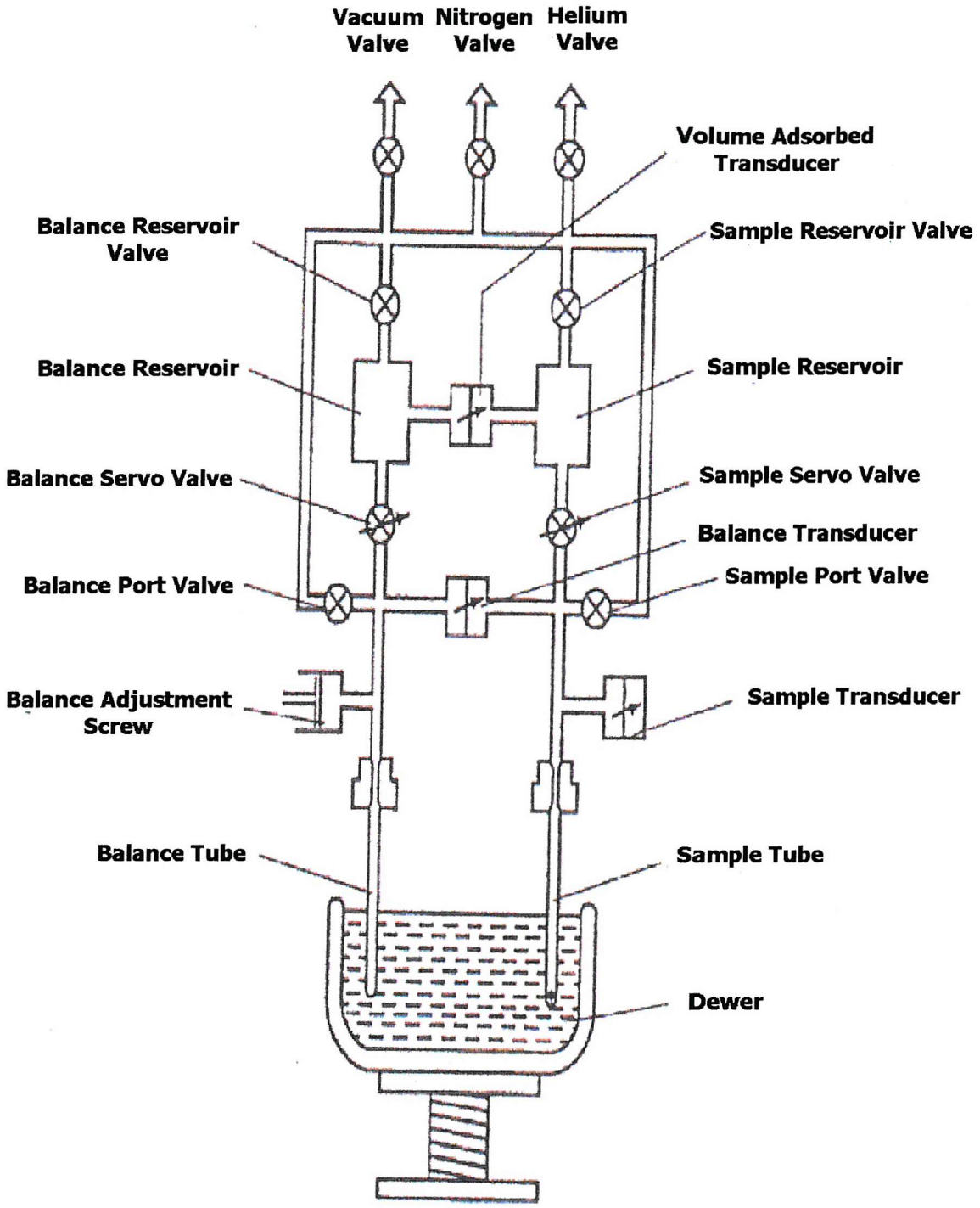

Figure 2.4 Schematic diagram of the plumbing system of Gemini 2375.

2.4 X-ray Absorption Spectroscopy

As a structural tool, X-ray absorption spectroscopy (XAS) can be fine-tuned to a specific element in a sample, and can then be used to extract structural data about a sample. This makes XAS an important tool in probing the structural environment of crystalline and amorphous solids. The XAS experiments can be used to estimate the type and number of atoms around the absorbing atom to a distance of 4-5 Å. This data comes from the local environment around the absorbing atom and is thus useful for materials such as mesoporous silicas which lack long-range order. Interatomic distances can be determined to 1% accuracy and coordination environments to 20% accuracy.

2.4.1 EXAFS Theory

EXAFS (Extended X-ray Absorption Fine Structure), is the name given to the high energy oscillations of an X-ray absorption edge for a particular element. As a beam of electrons travels through a material, the intensity of the beam decreases as interaction with the atoms of the material occurs. This decrease in absorption has a corresponding increase in energy which is characterised by sharp steps. The position of these steps corresponds to the atom types in the sample and are caused by electrons being ejected from core electronic states. The shell from which the electron is ejected is used to label the type of edge seen in the EXAFS spectrum, thus a K-edge results from 1s excitation and L-edges result from 2s or 2p excitation and so forth. These oscillations were observed as far back as 1920 by Fricke[12] and Hertz[13], but the full potential of the technique as a structural probe was only truly recognised in the late 1960s and early 1970s by Stern, Lytle and Sayers[14,15,16] with the EXAFS plane wave expression. These studies showed that the phase shift corrected Fourier transform of the EXAFS results in peaks which correspond to the distances of the nearest neighbouring atoms. This theory was then superceded by the current spherical wave theory developed by Gurman, Binsted and Ross[17,18] in recent years.

The final state interference effect involving the scattering of an outgoing photoelectron beam from a X-ray absorbing atom by the neighbouring atoms results in a sinusoidal variation of

the X-ray beam with energy. The probability of a core electron absorbing an X-ray photon is dependent on the electrons initial and final state. For a single atom, the final state is an outgoing spherical wave which has a wavelength λ, where $\lambda=2\pi/k$. k is the photoelectron wave vector calculated as:

$$k=[8\pi^2m/h^2\ (E-E_0)]^{1/2}$$

where m = mass of the electron

h = Planck's constant

E = X-ray photon energy

E_0 = threshold energy of the absorption edge.

In a sample with neighbouring atoms, back scattering from the outgoing electron wave with the neighbouring atoms causes an incoming wave. The sum of the interaction of the outgoing and incoming waves gives rise to the EXAFS oscillations which can be expressed as:

$$\chi = (\mu - \mu_0) / \mu_0$$

where μ is the absorption coefficient as a function of photon energy, and μ_0 is the normalising coefficient.

The EXAFS coefficient χ is plotted as a function of the photoelectron wave vector *k*, and this results in a decrease in intensity with increasing *k*. In practice, to prevent the domination of the strong oscillations at low *k* when determining structural parameters, the EXAFS spectra is weighted by a function of *k*, usually k^3 which enhances the oscillation at high *k*. The Fourier transform results in peaks corresponding to interatomic distances with the size and number of neighbouring atoms determined by the intensities of the peaks.

The Plane Wave Theory

The plane wave equation can be described as the sum of a series of dampened sine waves. If neighbouring atoms are present, back-scattering of the photoelectronic wave occurs (figure 2.5) which causes the final state to be modified by the interference effect of outgoing and back-scattered photoelectron waves.

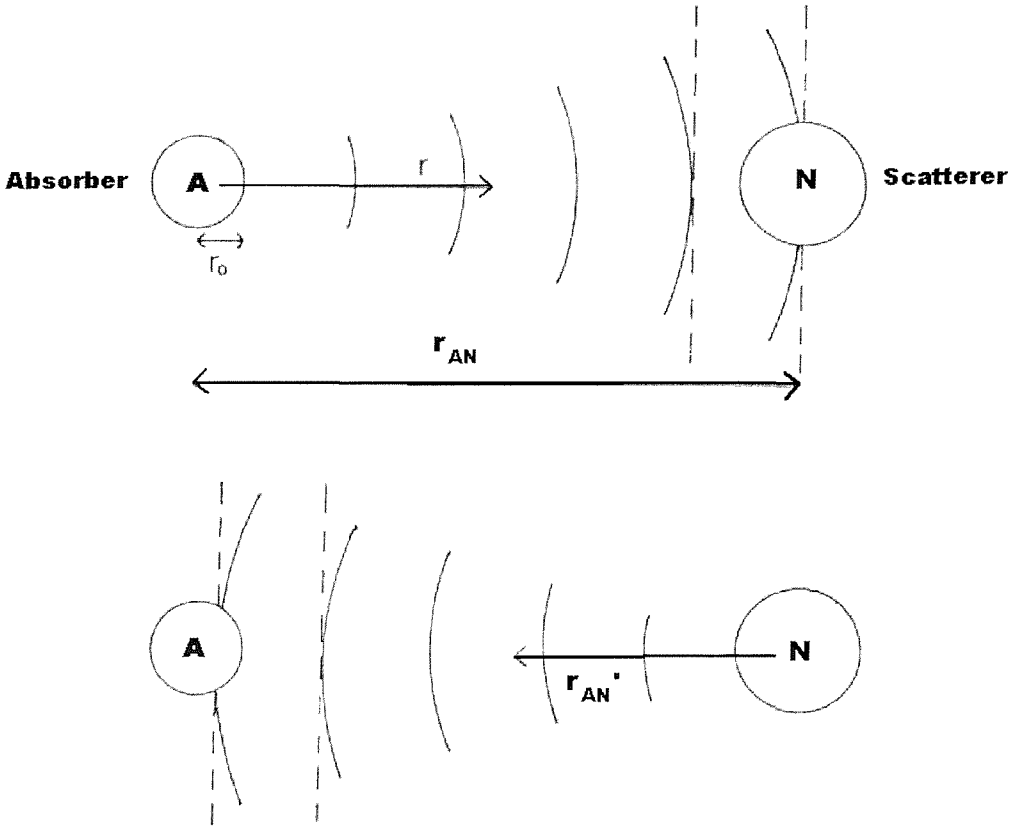

Figure 2.5 Back-scattering of the photoelectron wave caused by the neighbouring atom, N, at a distance r_{AN} from the absorbing atom, A.

The work of Stern, Lytle and Sayers[16] led to the recognition of structural EXAFS spectroscopy and was based on a simple single electron, single scattering theory. The derivation of the EXAFS equation as formulated by Lee and Pendry[19] led to the plane wave equation. This derivation assumed an interaction between the initial state and the final

interference state wave function based on the approximation that the outgoing spherical photoelectron wave could be treated as a plane wave in the presence of backscatterers. This approximation, known as the small atom approximation, holds true if it is assumed that the radius of the back scatterer is significantly smaller than the interatomic distance between the absorbing atom and the backscatterer. The EXAFS intensity, χ, as a function of the photoelectron wave, k can then be expressed mathematically as:

$$\chi(k) = \frac{1}{k}\sum_{s} S_i N_s \frac{|f_s(\pi,k)|}{R_{AN}^2} \exp(-2\sigma_{AN}^2 k^2) \exp\left(\frac{-2R_{AN}}{\lambda}\right) \sin(2kR_{AN} + 2\delta_i + \alpha_s)$$

where: S_i is an amplitude reduction factor due to multiple excitations of the absorber;

N_s is the number of equivalent back scattering atoms in each shell s;

R_{AN} is the interatomic distance between absorbing atom and back scattering atom;

$f_s(\pi,k)$ is the amplitude of the back scattering atom;

σ_{AN}^2 is the mean square variation of R_{AN};

λ is the elastic mean free path;

δ_i is the phase shift due to the absorbing atom;

α_s is the phase shift due to the back-scattering atom.

Each shell of equivalent atoms produces a unique interference pattern in the form of a dampened sine wave which has an overall magnitude proportional to the number of scattering atoms in the shell. The wave frequency is dependent on the distance between the absorbing and scattering atoms and the phase is affected by the phase shifts of the absorbing and scattering atoms. As the amplitude of the sine wave is inversely proportional to R_{AN}^2, for neighbouring atoms at longer interatomic distances, this amplitude is reduced.

The plane wave equation is a mathematical expression of the EXAFS intensity and consists of several parameters which are essential to EXAFS analyses.

Phase shifts

On leaving the absorbing atom and travelling to a backscattering atom, the photoelectron wave, k, undergoes a phase shift due to the potential of the absorbing atom, δ_i, which is expressed as $kR_{AN} + \delta_i$. If the photoelectron wave is backscattered by the neighbouring atom, a second phase shift, α_s, occurs. The back-scattered photoelectron wave, returning to the absorbing atom, experiences another phase shift of $kR_{AN} + \delta_i$ due to the absorbing atom giving a total phase shift of:

$$\sin(2kR_{AN} + 2\delta_i + \alpha_s)$$

The phase shift of an absorbing atom is caused by an electron being diffracted as it leaves the absorbing atom. The ejection of an electron leaves a positive charge on the absorbing atom. At low kinetic energies, the photoelectron is shielded by the valence electrons of the atom and at high kinetic energies, this screening is incomplete. However, at high kinetic energies, the positive charge on the atom is assumed to affect the passage of the photoelectron only lightly. In calculating the phase shift of a given atom with an atomic number of Z, the potential for a Z+1 atom is used to account for the effects of the positive charge on the atom. In an EXAFS experiment, phase shifts are calculated for all the different types of atoms present in the sample and these are then used to fit theoretical models to EXAFS data.

The term $F_s(\pi,k)$ is the amplitude of the backscattered wave. Its phase shift is reliant on the electron potential from which scattering occurs. This potential consists of contributions from electrostatic and quantum mechanical effects and is used to calculate phase shifts.[20,21] In general, the amplitude of a back-scattered wave increases with the increasing atomic number of back-scattering atoms.

Phase shifts are dominated by inner shell electrons which, being strongly bound together, are chemically insensitive and thus transferable between samples.

Debye-Waller Factors

The Debye-Waller factors, expressed in the plane wave equation as $\exp(-2\sigma_{AN}^2 k^2)$ is the term used to describe the dampening of the EXAFS oscillation caused by static disorder and thermal vibrations. EXAFS gives averaged interatomic distances for the absorbing and back-scattering atoms. In reality, in any given shell, there will be a varied distribution of interatomic distances. When two atoms are close together, their thermal motions are sympathetic and the mean square variation in the separation distances, σ_{AN}^2, is less, resulting in a smaller Debye-Waller factor. For two atoms at longer interatomic distances, there is less correlation between the atoms giving a larger mean square variation and resulting in larger Debye-Waller factors.

Mean Free Path

The mean free path term, $\exp(-2R_{AN} / \lambda)$, is dependent on the lifetime of the photoelectron. Travelling to and from the absorbing atom, the photoelectron wave loses energy via inelastic scattering processes, leading to a limited path-length and lifetime. This means that the interaction of the outgoing and back-scattered waves are reduced and therefore the interference effects are also reduced. This reduction in the EXAFS oscillation is dependent on the ratio of R_{AN}, the interatomic distance and the elastic mean free path, λ.

Amplitude Reduction Factor of Multiple Excitations

The amplitude reduction factor S_i, is due to multiple excitations of the absorbing atom. On ejection of a photoelectron, some of the excess energy present causes excitation and even further ejection of other electrons in the atom. This reduces the energy of the ejected photoelectron and leads to a shift in the photoelectron's phase and energy and a reduction in the EXAFS oscillation. This is assumed to be independent of the chemical environment of the absorbing atom[22] and therefore, the dampening of the EXAFS oscillation by multiple excitations can be treated as a constant energy factor.

The Curved Wave Theory

As the plane wave equation does not allow for the spherical nature of the photoelectron wave function, the curved wave theory developed by Lee and Pendry[19] has to be applied. This theory allows for the size of the absorbing atom and the affects of the scattering atom. As this theory involves solving a matrix function which is complicated and time-consuming, a modified version using computationally fast algorithms in iterative processes is used.[17,18]

2.4.2 Data Acquisition

The spectra presented in this thesis were obtained using the Synchrotron Radiation Source at the CLRC Daresbury Laboratory on XAS stations 7.1, 8.1 and 9.2 in either transmission mode or fluorescence mode for more dilute samples.

Synchrotron radiation is produced by accelerating electrons close to the speed of light in an ultra high vacuum. These electrons are injected into a storage ring where they are kept circling at this speed by the use of bending magnets. When these electrons interact with the magnetic fields of the magnets, intense white electromagnetic radiation is emitted which exits the storage ring via ports which carry the radiation through the beam lines to the experimental stations.

The XAS experiment measures the X-ray absorption coefficient μ, as a function of the monochromator steps. The monochromator is used to select the correct wavelength to align the beam incident on the sample. Station 7.1 uses a silicon (111) double crystal monochromator and station 9.2 uses a silicon (220) double crystal monochromator to select the required wavelengths. The fundamental wavelength is selected in accordance with the Bragg equation. In addition to the chosen fundamental wavelength, the monochromator also allows higher order harmonics through. If these are not removed, they can lead to significant distortion of the EXAFS as they are not absorbed by the sample in the same way as the fundamental wavelength is. The higher harmonic wavelengths are removed by offsetting the angle of the first crystal with respect to the second crystal. This causes a greater loss in the

intensity of the harmonic wavelengths than the intensity of the fundamental wavelength. An ion chamber, I_0, measures the intensity of the beam of light passing through the monochromator with a maximum intensity when the crystals are parallel and a minimum intensity when the crystals are offset. This angular dependency of the intensity, termed the rocking curve, is steeper for higher harmonic wavelengths than for the fundamental wavelength. Thus if the crystals are offset correctly to allow only 50% of the maximum intensity through to the sample, then most of the higher harmonic wavelengths are rejected and 50% or more of the fundamental wavelength is retained.

The size of the beam is also determined by entrance and exit slits situated before and after the monochromator which can be adjusted to narrow or widen the beam as required. Of the two, the entrance slit defines the size of the beam whilst the exit slit functions primarily to stop any scattered light from the monochromator reaching the sample.

In transmission mode, the absorption is measured via two ion chambers filled with inert gases. One ion chamber, I_0, is placed before the sample and the second ion chamber, I_t, is placed after the sample. The mixture of gases in each is chosen so that I_0 absorbs 20% of the beam and I_t absorbs 80% of the beam. The absorbance is then calculated from the log of the ratio of the measurements from the two ion chambers, $\ln I_0/I_t$.

In fluorescence mode, the sample is placed at an angle of 45° to the beam to maximise the fluorescence signal. A solid state detector, placed perpendicular to the beam and at the same distance along the beam is used to detect the fluorescence signal. The intensity of the fluorescence, I_f, is a direct measure of the probability of the absorption of the k shell at a particular energy[23] (for dilute samples) and is calculated by plotting I_f/I_0.

Sample Preparation

Standard solid state samples were prepared for EXAFS analysis by finely grinding the sample with boron nitride and securing this to an aluminium sample holder with Kapton tape. The quantities of sample to boron nitride were measured to give a 10% concentration

by weight of the absorbing element. Air or moisture sensitive samples were prepared similarly in a glove box using dehydrated boron nitride.

All *in-situ* experiments were performed in fluorescence mode in a specially designed cell consisting of an adjustable steel plunger which was fitted inside a steel cell with a Kapton window. The cell had ports to allow in various gases and to allow a vacuum to be maintained. It was found that coating the plunger surface with thin layers of aluminium foil prevented spurious readings from the nickel atoms in the steel. Samples for *in-situ* experiments were prepared in a glove box. The sample was slurried with a dehydrated solvent to form a suspension. This suspension was then applied to the surface of the plunger via a pipette and the solvent was allowed to evaporate off leaving an even layer of the sample. This was repeated several times to obtain maximum coverage on the surface of the plunger. The plunger was then sealed inside the cell ready for the experiment.

2.4.3 Data Analysis

The EXAFS experiment gives an average of the different environments within any particular sample. Each shell of atoms gives rise to a dampened sine wave, the sum of which is seen as the EXAFS spectrum. Analysis of the data takes the form of two stages. The first is a background subtraction which extracts the EXAFS oscillations from the raw data which also contains data from the absorbing matrix and the interference of any backscattered waves. Background subtraction was achieved via the application of a computational program called PAXAS.[24] The second stage of the analysis involves fitting the background subtracted spectra to theoretical models of the sample using the EXCURV92[25] program from which structural information about the sample is obtained.

PAXAS

The PAXAS program allows the EXAFS oscillations to be separated from total absorption

via a series of background subtractions. The raw data from the experiment is initially recorded as the absorption versus the monochromator steps. This data is converted to absorption versus energy (eV) with respect to the monochromator d-spacing which depends upon whichever EXAFS station the data was recorded at. For spectra obtained in transmission mode, one data scan is deemed sufficient. For spectra obtained in fluorescence mode, multiple scans need to be averaged to increase the signal to noise ratio.

By subtracting a 2^{nd} or 3^{rd} order polynomial from the absorption spectra, a pre-edge background subtraction is achieved. This is seen as a curve which passes along the pre-edge and extends to a point P1 at the end of the post-edge region which is weighted and defined by the user (figure 2.6A). Points L1, at the beginning of the pre-edge region, and U1, at the end of the pre-edge region, are used to define the polynomial. By weighting the polynomial to make it pass through the Y-coordinate of P1, the background subtracted absorption (BSA) is normalised and seen as an approximately horizontal line.

Post-edge background subtraction (figure 2.6B) is calculated by using higher order polynomials of 6, 7 or 8, inverse polynomials, cubic splines or two linked polynomials. The post-edge subtraction curve passes through the centre of the oscillations, post-edge, and can be weighted at the top of the edge which affects the quality of the subtraction. The post-edge subtraction is used to remove the background noise which affects the oscillations of the EXAFS spectra and are seen as features in the Fourier Transform of the spectra at low radii of less than 1 Å. These features are removed by defining a window around the real data shells and calculating the EXAFS contributions from these shells. An iterative process refines the variables of the polynomial expression to minimise the differences between the calculated and experimental EXAFS. The window can be moved to include or exclude shells to obtain the EXAFS contributions from all reasonable shells and to remove as many of the background features as possible (figure 2.7).

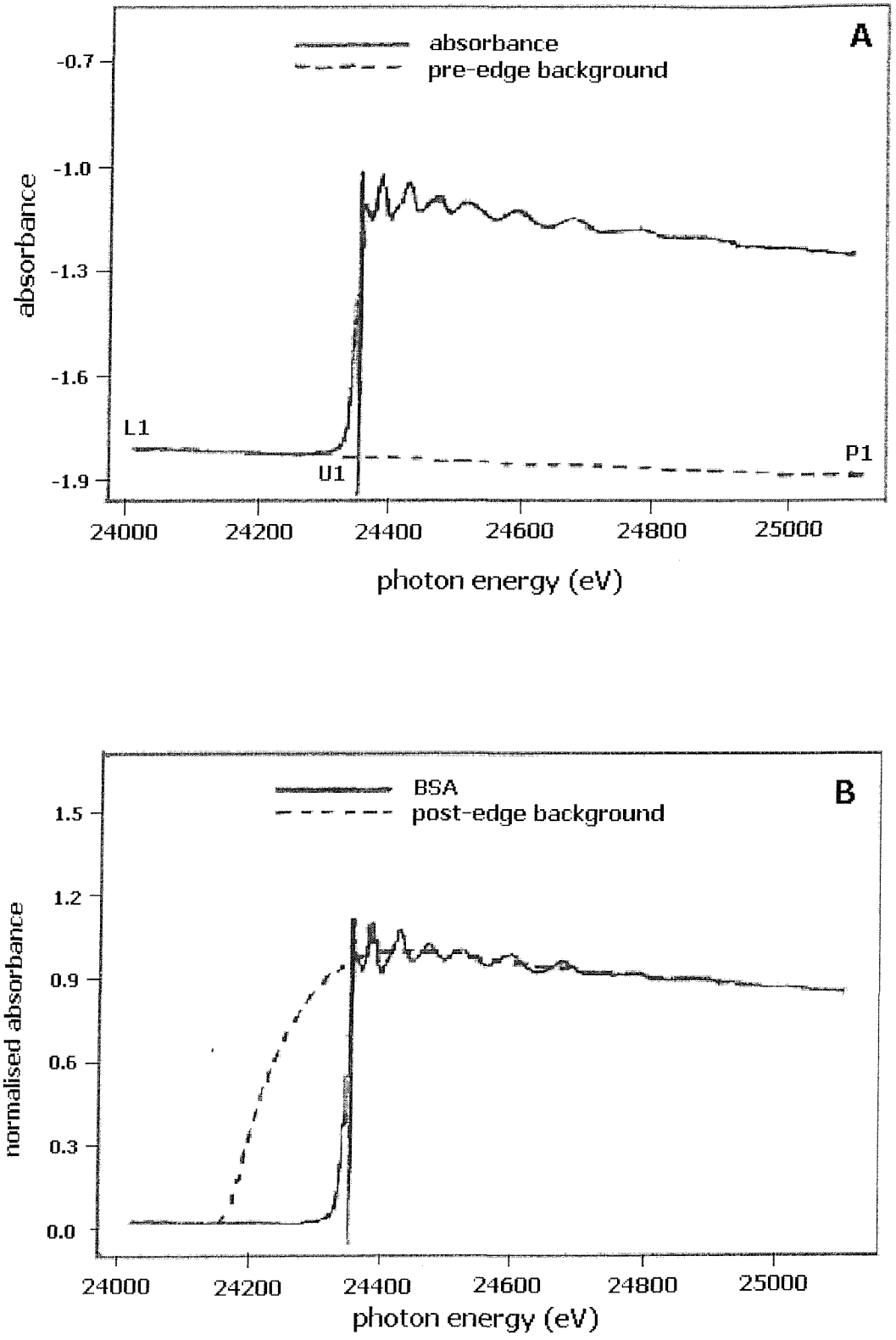

Figure 2.6 Pre-edge background subtraction (A) and post-edge background subtraction (B) of X-ray absorption spectra of $PdCl_2$.

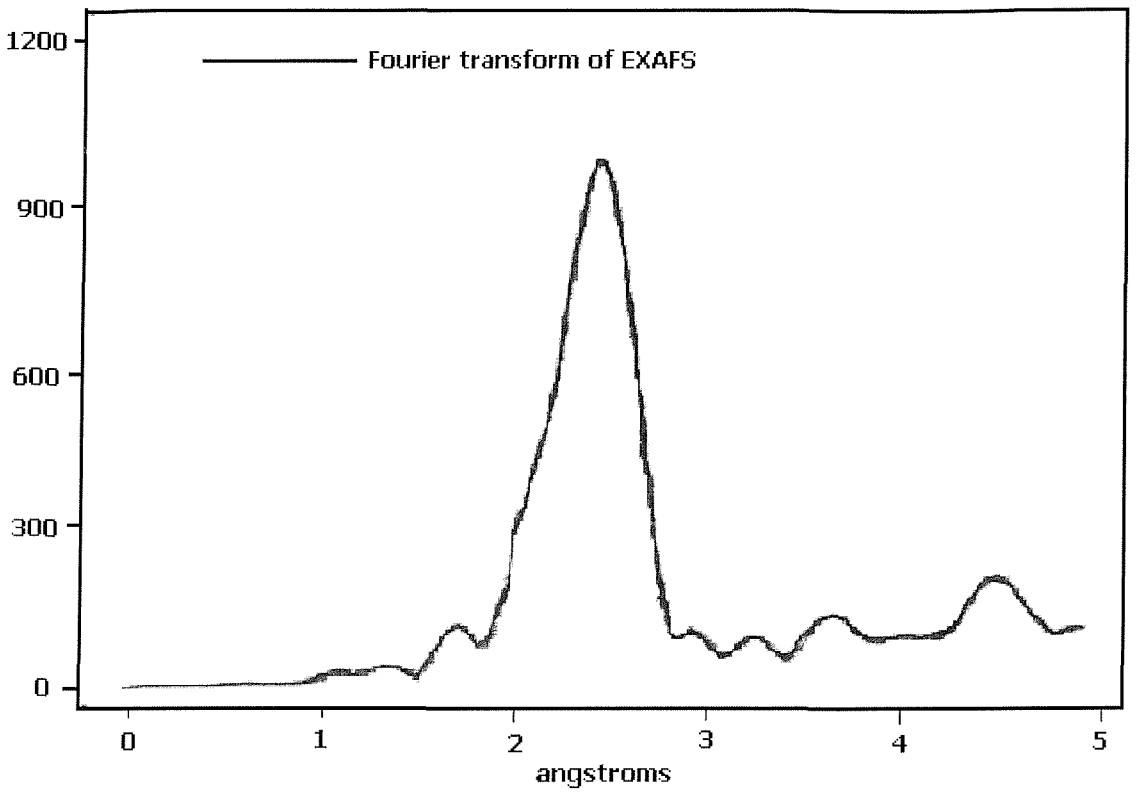

Figure 2.7 Background subtracted Fourier Transform of EXAFS spectra of $PdCl_2$.

EXCURV92

EXCURV92 is an interactive program designed to calculate a theoretical EXAFS spectrum based on a theoretical model defined by the user. The program is based on the curved wave theory and uses a number of variable parameters in a least-squares iterative procedure to optimise the fit between an experimental spectrum and a theoretical spectrum of any particular sample. Phase shifts for all the elements present in any given sample are calculated via *ab initio* methods which use Von-Barth ground state potentials and Hedin-Lundqvist exchange potentials. A definition of the parameters is as follows:

Ns	The number of shells for which the theory is calculated
Nn	The number of atoms, N, in shell n
Rn	The distance of shell n from the central atom
Tn	The type of atom for shell n; the central atom is designed as shell 1
An	The Debye-Waller factor for shell n
Emin	The minimum energy value for calculating the theoretical spectrum
Emax	The maximum energy value for calculating the theoretical spectrum
E_0	The magnitude of the photoelectron energy at zero wavenumber
E_f	The difference between calculated Fermi-level energy and the known energy value for the element
Kmin	The wave vector corresponding to (Emin + E_0)
Kmax	The wave vector corresponding to (Emax + E_0)
Lmax	The maximum angular momentum used in calculating the theoretical spectrum
AFAC	The energy independent amplitude factor intended to account for the reduction in the amplitude due to multiple excitations
WPI	This allows for experimental broadening as the imaginary potential constant for the lifetime of the photoelectron (VPI) cannot be specified by the user.

During the iteration procedure, shell distances, Debye-Waller factors and E_f are refined. The co-ordination numbers are initially set at reasonable values and adjusted to improve the fit as necessary. The fit between theoretical and experimental spectra is measured by the R-factor and the Fit Index (FI). The R-factor calculates the sum total of the errors between all the data points and shows this as a percentage against the experimental spectrum. The Fit Index calculates the sum of the square of the difference between experimental and theoretical data points. In standard samples, the R-factor is not expected to exceed 30% but for dilute samples (obtained in fluorescence mode), the data tends to be noisy and thus keeping the R-factor below 30% becomes unfeasible. Good Fit Indexes can achieve values below 5 $x10^{-4}$.

Theoretical models are obtained by adding one shell of variables at a time using statistical tests such as that of Joyner, Martin and Meehan[26] to assess the validity of the shell. This test suggests that if, on addition of a new shell, $FI_{n+1}/FI_n < 0.96$, then the new shell is significant.

The calculation of χ^2 can also be used to prove statistical significance; if $\chi^2_{n+1} < \chi^2$, then the shell is statistically significant. Procedures for both these tests are possible within the EXCURV92 program. A shell can also be rejected on the basis of anomalous interatomic distances or very low or very high Debye-Waller factors. Interatomic distances for the first coordination sphere can be calculated to an accuracy of ±0.01 Å and coordination numbers to ±10%. EXCURV92 calculates statistical errors and does not make allowance for any experimental errors.

For the purpose of this work, theoretical spectra were generated for unknown systems using chemically sensible models. The coordination numbers were set to reasonable values and A_n, R_n and E_f were refined in the iterative process. Statistical tests and common sense was used to assess the significance of the shells. Where possible, the organometallic species were compared to known models and chemically inconsistent shells were disregarded.

2.5 References

1. Engelhardt, G., *Stud. Surf. Sci. Catal.*, 1991, **58**, 285.
2. Sanders, J. K. M., Hunter, B. K., *Modern NMR Spectroscopy - a guide for Chemists*, Oxford University Press, Oxford, 1987, 260.
3. Harris, R. K., *Chemistry in Britain*, 1993, **29**, 601.
4. Klinowski, J., *Chem. Rev.*, 1991, **91**, 1459.
5. Davis, M. E., Robo, R. L., *Chem. Mater.*, 1992, **91**, 1459.
6. Parise, J. B., MacDougall, J. E., Herron, N., *Inorg. Chem.*, 1988, **27**, 221.
7. Fyfe, C. A., Feng, Y., Groudey, H., Koktailo, G. T., Guis, H., *Chem. Rev.*, 1991, **95**, 9620.
8. Goodhew, P. J., Humphreys, F. J., *Electron Microscopy and Analysis*, Taylor & Francis, London, 1988, 2nd Ed.
9. Jose-Yacaman, M., Diaz, G., Gomez, A., *Catalysis Today*, 1995, **23**, 161.
10. Jaycock, M. J., *Experiments in Physical Chemistry*, 337.
11. Brunauer, S., Emmett, P. H., Teller, E., *J. Am. Chem. Soc.*, 1938, **60**, 309.
12. Fricke, H., *Phys. Rev.*, 1920, **16**, 202.
13. Hertz, G., *Z. Phys.*, 1920, **3**, 19.
14. Lytle, F. W., Sayers, D. E., Stern, E. A., *Phys. Rev.*, 1971, **27**, 1204.
15. Stern, E. A., *Phys. Rev. B*, 1974, **10**, 3027.
16. Lytle, F. W., Sayers, D. E., Stern, E. A., *Phys. Rev. B*, 1975, **11**, 4825.
17. Gurman, S. J., Binsted, N., Ross, I., *J. Phys. C*, 1984, **17**, 143.
18. Gurman, S. J., Binsted, N., Ross, I., *J. Phys. C*, 1986, **19**, 1845.
19. Lee, P. A., Pendry, J. B., *Phys. Rev. B*, 1975, **11**, 2795.
20. Lee, P. A., Teo, B. K., *J. Am. Chem. Soc.*, 1979, **101**, 2815.
21. Chan, S. K., Knapp, G. S., McKale, A. G., Paulikas, A. P., Veal, B. W., *J. Am. Chem. Soc.*, 1988, **110**, 3763.
22. Eisenberger, P., Lengeler, B., *Phys. Rev. B*, 1980, **22**, 3551.
23. Jaklevic, J., Kirby, J., Klein, M., Robertson, A., Brown, G., Eisenberger, P., *Solid State Commun.*, 1977, **23**, 679.

24. Binsted, N., *PAXAS, Program for the analysis of X-ray Absorption Spectra*, University of Southampton, 1997.

25. Binsted, N., Gurman, S. J., Campbell, J. W., *EXCURV92*, SERC Daresbury Laboratory program, 1992.

26. Joyner, R. W., Martin, K. J., Meehan, P., *J. Phys. C*, 1987, **20**, 4005.

CHAPTER THREE

Synthesis and Characterisation of Mesoporous Silicas

3.0 Introduction

In order to use mesoporous silicas as supports for organometallic complexes, it is essential that the support is first fully characterised and understood. It must also be free of impurities which could react with the organometallic species and affect the anchoring of the species. This chapter describes the synthesis and characterisation of various mesoporous silicas including MCM-41 and MESLC. Due to the amorphous nature of these materials, a combination of techniques was used to obtain full characterisation including transmission electron microscopy, powder X-ray diffraction, magic angle spinning NMR spectroscopy, BET surface area measurements and infra-red spectroscopy.

3.1 MCM-41

The structure of the MCM-41 materials was first reported in 1992 by Beck and Vartuli[1,2] at the Mobil Corporation in America and was described as a regular hexagonal array of silicon atoms with pore diameters of 15-100 Å. Purely siliceous and aluminosilicate MCM-41s were reported and the common factor remained the regular array of atoms even though the material itself was amorphous in nature. The pore sizes were controlled by the length of the template used and the mechanism is thought to be via the interaction of inorganic ions with discrete template aggregates (figure 3.1).[3,4,5]

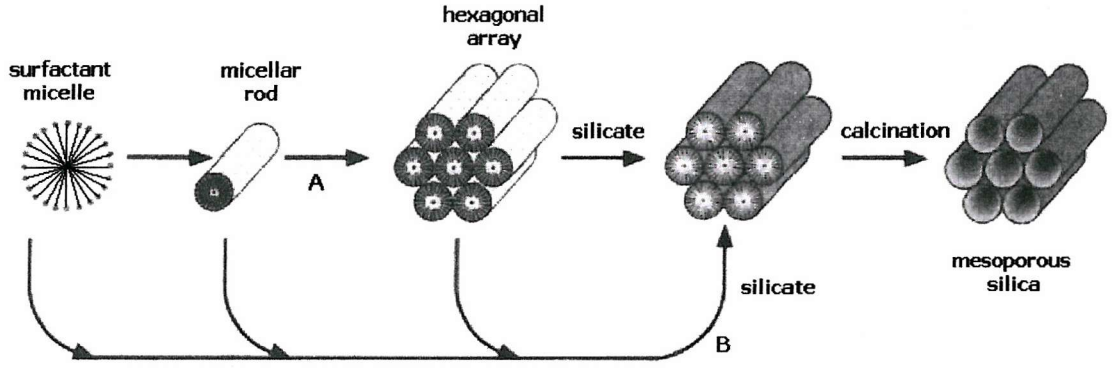

Figure 3.1 Possible mechanistic pathways for the formation of mesoporous silicas; (A) liquid crystal phase initiated and (B) silicate ion initiated.[1]

3.1.1 Synthesis of MCM-41(A)

Sodium silicate solution (9.35 g, 6.72 ml, 0.03 mol), sulphuric acid (0.6 g, 6.12×10^{-3} mol) and deionised water (20 g, 1.11 mol) was stirred vigorously for 10 minutes. The template solution, $C_{12}H_{25}(CH_3)_3NCl$ (7.09 g in 21.3 g water) was added and the solution stirred for 0.5 h. Water (10 g) was added and the mixture was refluxed at 100°C for 144 h. The product was filtered hot, washed with water (10 cm^3) and dried under vacuum. The white powdered product (2.89 g) was calcined in compressed air at 450°C for 24 h followed by 48 h in a stream of flowing oxygen.

3.1.2 Characterisation of MCM-41(A)

Calcined MCM-41(A) was characterised by PXRD, MAS NMR, infra-red spectroscopy, BET surface area measurements and TEM.

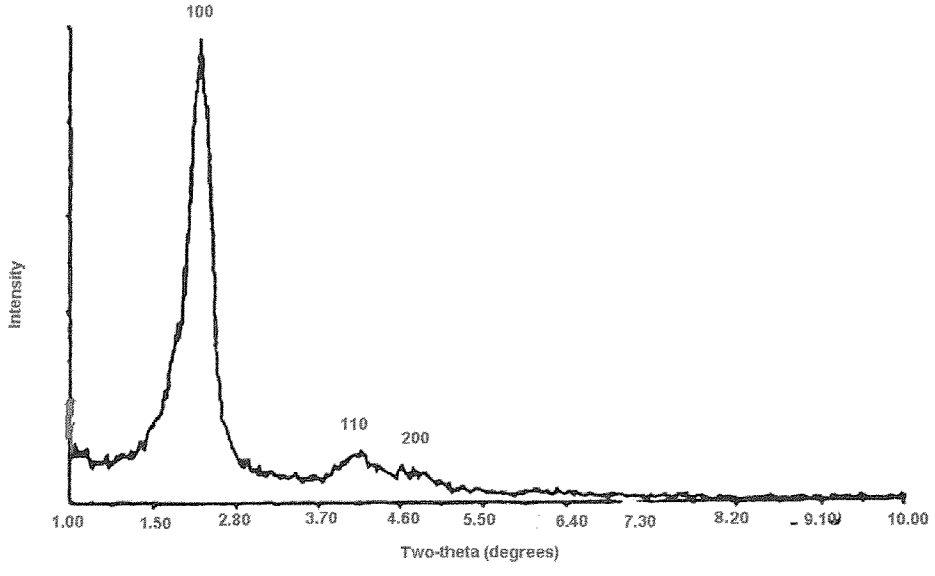

Figure 3.2 PXRD pattern of MCM-41(A)

Powder X-ray Diffraction

For X-ray diffraction techniques, long range order is needed. As there is a lack of long-range order in the MCM-41 materials, powder X-ray diffraction (PXRD) gives minimal information. With these types of materials, it is used as a fingerprint technique.[6,7] The PXRD pattern for MCM-41(A) can be seen in figure 3.2 and shows three peaks which are characteristic of a hexagonal lattice[8] with a unit cell of approximately 35 Å.

MAS NMR Spectroscopy

^{29}Si MAS NMR spectra of MCM-41(A) were recorded, at a spinning speed of 5 kHz and the spectrum (figure 3.3) shows several peaks which overlap to give a broad unsymmetrical band centred around -100 ppm. This closely resembles the spectra for amorphous silica and suggests a broad range of Si-O-Si bond angles.[9,10,11]

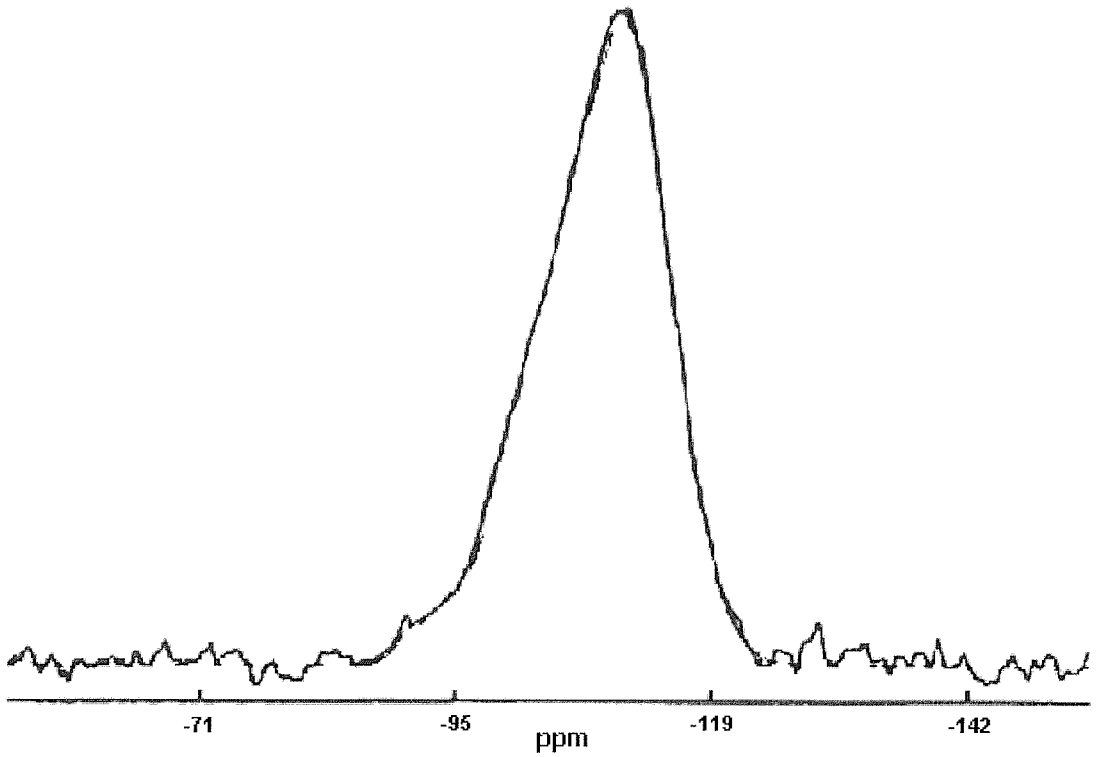

Figure 3.3 ^{29}Si 5 kHz MAS NMR of MCM-41(A)

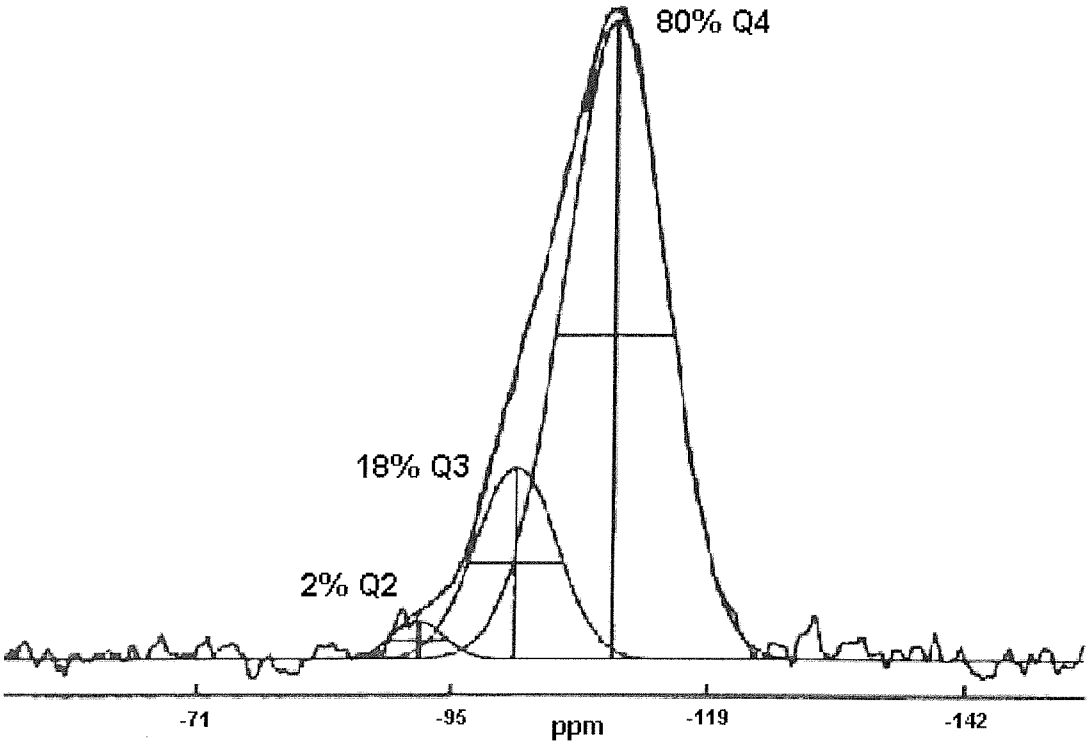

Figure 3.4 ^{29}Si 5 kHz MAS NMR of MCM-41(A) with curve-fitting

On applying a curve-fitting program to the spectra, it is possible to determine the ratio of silica sites within the material (figure 3.4). This gives percentage Q4:Q3:Q2 ratios of 80:18:2 where Q4 is the bulk silica [$Si(OSi)_4$], Q3 is mono-hydroxylated silica [$Si(OSi)_3OH$] and Q2 is dihydroxylated silica [$Si(OSi)_2(OH)_2$]. The amount of Q1 silica is negligible. Therefore, 20% of all of the silica is available as silanol groups for potential attachment to organometallic species.

Transmission Electron Microscopy

An enlarged transmission electron micrograph (figure 3.5) shows the hexagonal array of uniform channels with pore diameters measuring 22.3 Å and wall thickness of approximately 12 Å which is consistent with the unit cell parameters and literature values.[12]

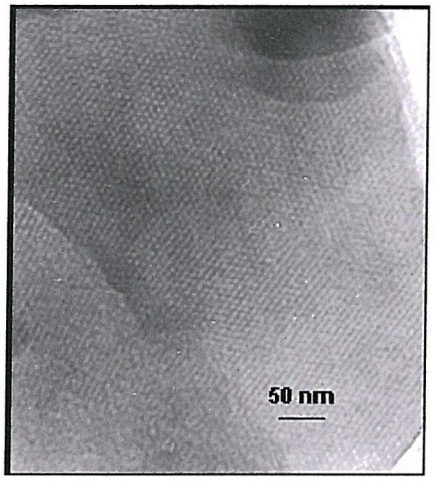

Figure 3.5 TEM of MCM-41(A)

BET Surface Area Measurement

BET surface area measurements were performed on dehydrated samples of the MCM-41(A). Measurements obtained from the Gemini 2375 gave a surface area of 1422 m^2g^{-1} with a maximum sorption of N_2 at 228.3 mmHg pressure. This is higher than the literature value[1] quoted at 1040 m^2g^{-1}. Figure 3.6 shows the hysteresis of the absorption and desorption of N_2 from the sample.

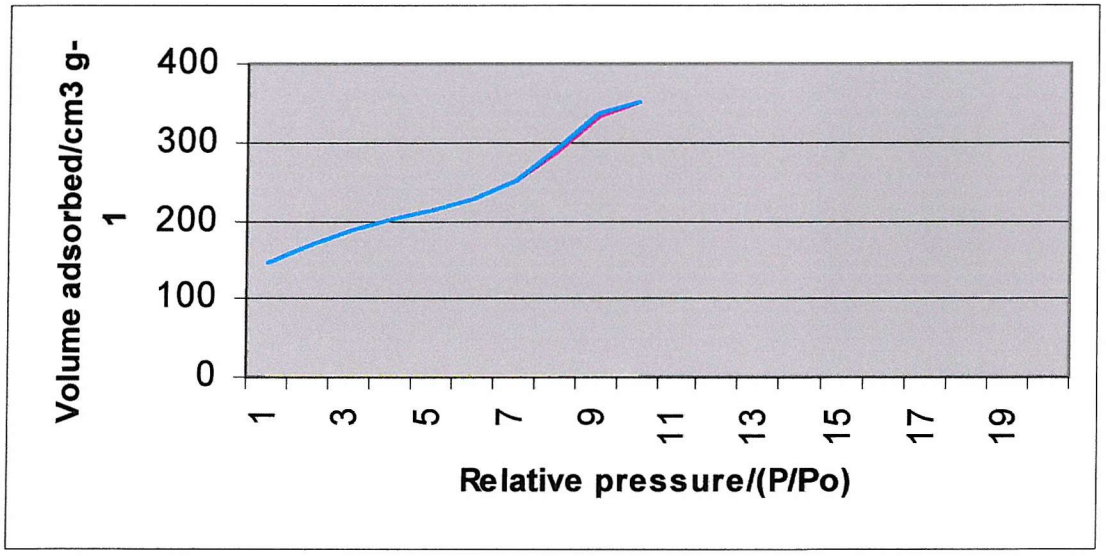

Figure 3.6 Hysteresis curve for BET surface area measurement of MCM-41(A)

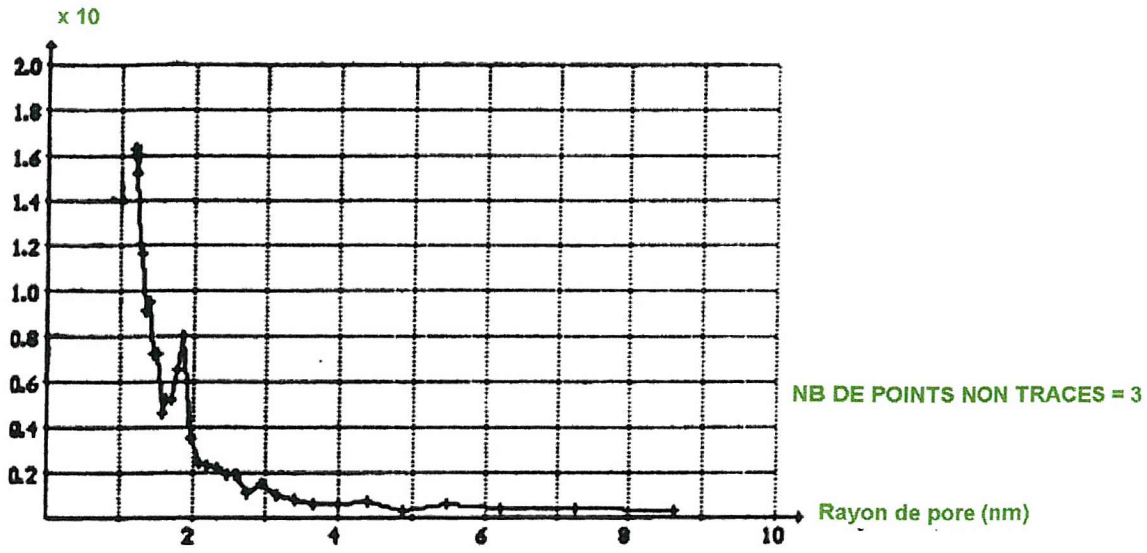

Figure 3.7 Pore size distribution graph for MCM-41(A)

Results obtained from the Laboratoire de Chimie Organometallique de Surface, Villeurbanne, France, gave a BET surface area measurement of 1646 m^2g^{-1}. From these experiments, it was also possible to find out the porous volume which is a more useful measurement. For this material, the porous volume was calculated to be 65.6 cm^3g^{-1}. From a pore size distribution graph (figure 3.7), the pore diameter of the sample was determined to be 18.8 Å. This is smaller than the 22.3 Å determined from the TEM but falls within the unit cell parameters.

Infra-red Spectrometry

The synthesis of the MCM-41 materials involves a large amount of water which is trapped within the mesoporous structure as it is formed. Even after calcination at 450°C in flowing oxygen, the large water content is apparent (figure 3.8). In order to monitor a reaction between the MCM-41 materials and a complex via infra-red spectrometry, it is necessary to see the silanol peak at 3747 cm^{-1} in the spectrum.[13] This is hidden by the broad water band and therefore the water has to be removed before any reactions can take place.

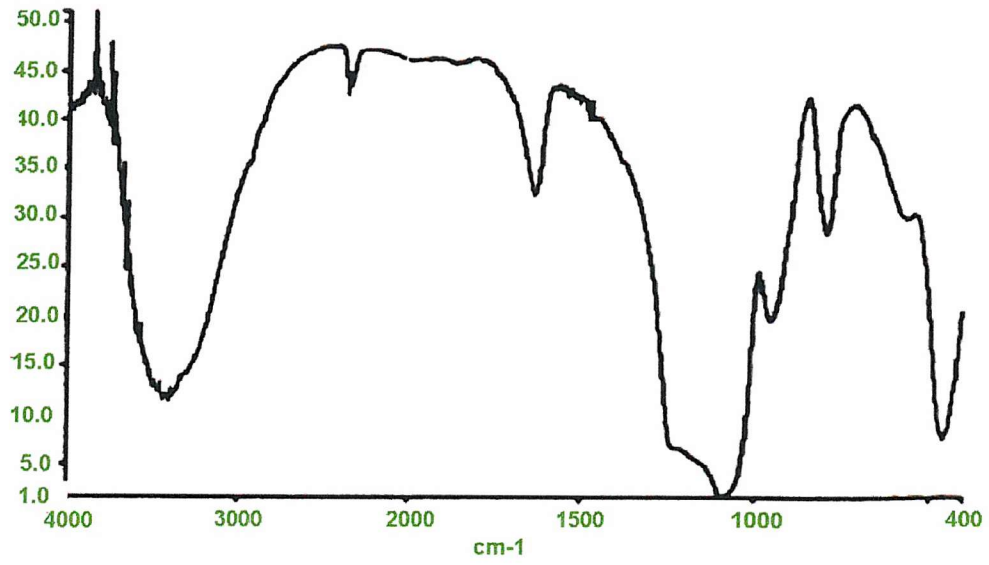

Figure 3.8 Infra-red spectrum of calcined MCM-41(A)

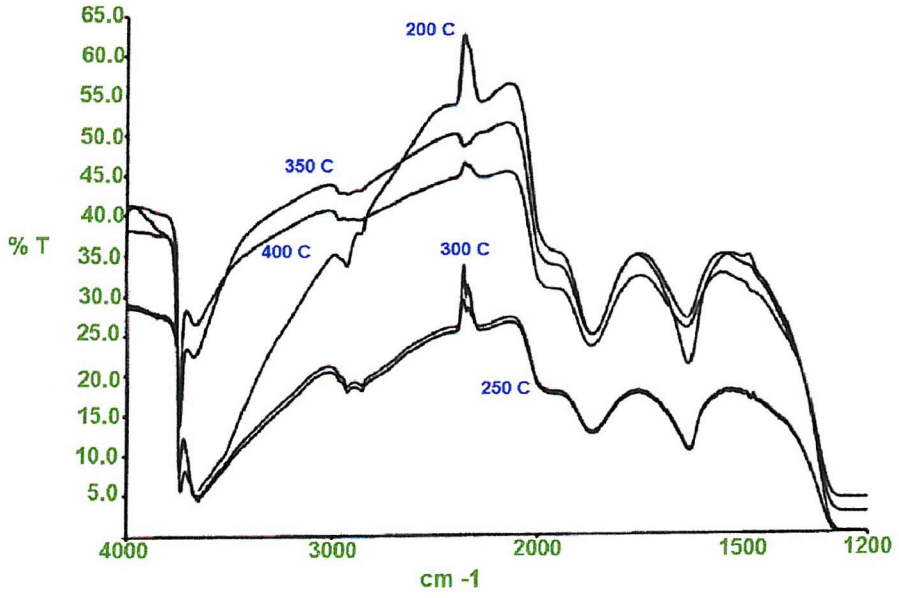

Figure 3.9 Infra-red spectra of MCM-41(A) from 200-450°C

A compressed disk was made of the MCM-41(A) material. This was placed in a sealed infra-red cell which has CaF_2 windows. The cell was heated to 200°C for 5 h. At this temperature, most surface water should evaporate off. After 5 h an IR spectrum was measured. In increments of 50°C, the temperature was increased to calcination temperature (450°C) and held there for 5 h. An IR spectrum was measured at each increment. A comparison of all the spectra (figure 3.9) shows the change in the water content.

IR signal/cm^{-1}	Assignment
3747	ν(SiO-H)
3600-3700	H-bonding of H_2O ν(SiO-H-O)
1865	overtone of ν(Si-O)
1632	ν(OH_2)

Table 3.1 Assignment of infra-red spectrum

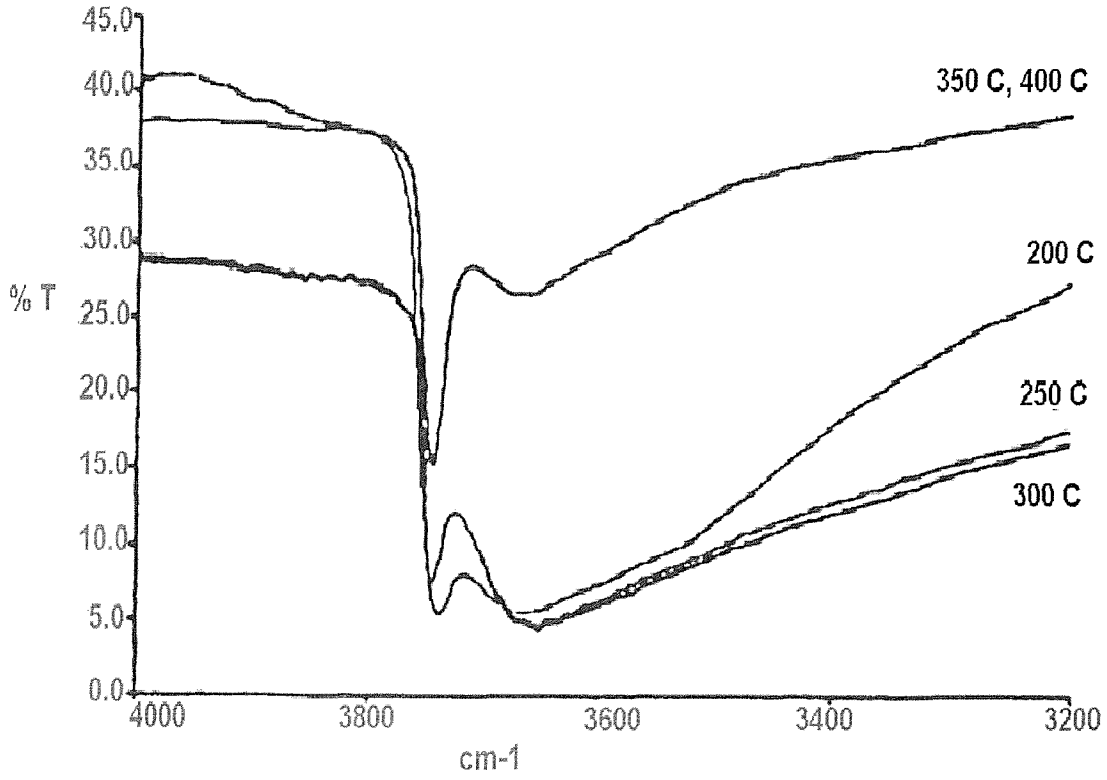

Figure 3.10 Expanded IR spectra of ν(OH) region

Table 3.1 shows the assignment of infra-red signals. Between 200-300°C, no significant decrease is noticeable in the broad band at 3600-3700 cm^{-1}. At 350°C, this band decreased drastically to leave a fairly sharp silanol peak at 3744 cm^{-1}. The band at 1632 cm^{-1} is due to water and the band at 1865 cm^{-1} is due to an overtone of Si-O stretches. At 350°C, the band at 1632 cm^{-1} also decreased significantly. The band corresponding to Si-O stretches is relatively unchanged. The spectra at 350°C and 400°C are practically indistinguishable from each other.

On expansion of the region between 3200-4000 cm^{-1} (figure 3.10), a band at 3650 cm^{-1} is seen masked by the bulk water band. This is due to silanol groups (Si-OH) hydrogen bonding to the H_2O molecules.[14] This is only seen between 200-300°C. As the temperature is increased, the water is removed and this band is lost.

A second disk of the same material was heated under vacuum directly to 450°C and was found to have changed colour. On removal from the heat, the disk had turned black. Therefore it is possible that either this sample retained some template that charred on heating or that heating over a long period of time at increasing temperatures has a tempering effect on the material.

3.1.3 Synthesis of MCM-41(B)

Sodium silicate solution (9.35 g, 6.72 ml, 0.03 mol), sulphuric acid (0.6 g, 6.12×10^{-3} mol) and water (20 g, 1.11 mol) was stirred vigorously for 10 minutes. The template solution, $C_{14}H_{29}(CH_3)_3NBr$ (7.74 g in 23.2 g water) was added and the solution stirred for 0.5 h. Water (10 g) was added and the mixture was refluxed at 100°C for 144 h. The product was filtered hot, washed with water (10 cm^3) and dried under vacuum. The white powdered product (5.07 g) was calcined in compressed air at 450°C for 24 h followed by 48 h in a stream of flowing oxygen.

3.1.4 Characterisation of MCM-41(B)

This material was characterised by PXRD, TEM, MAS NMR, IR and BET surface area measurements.

Powder X-ray Diffraction

The PXRD pattern for MCM-41(B) can be seen in figure 3.11 and shows the three peaks characteristic of a hexagonal lattice corresponding to a unit cell of approximately 40 Å

.

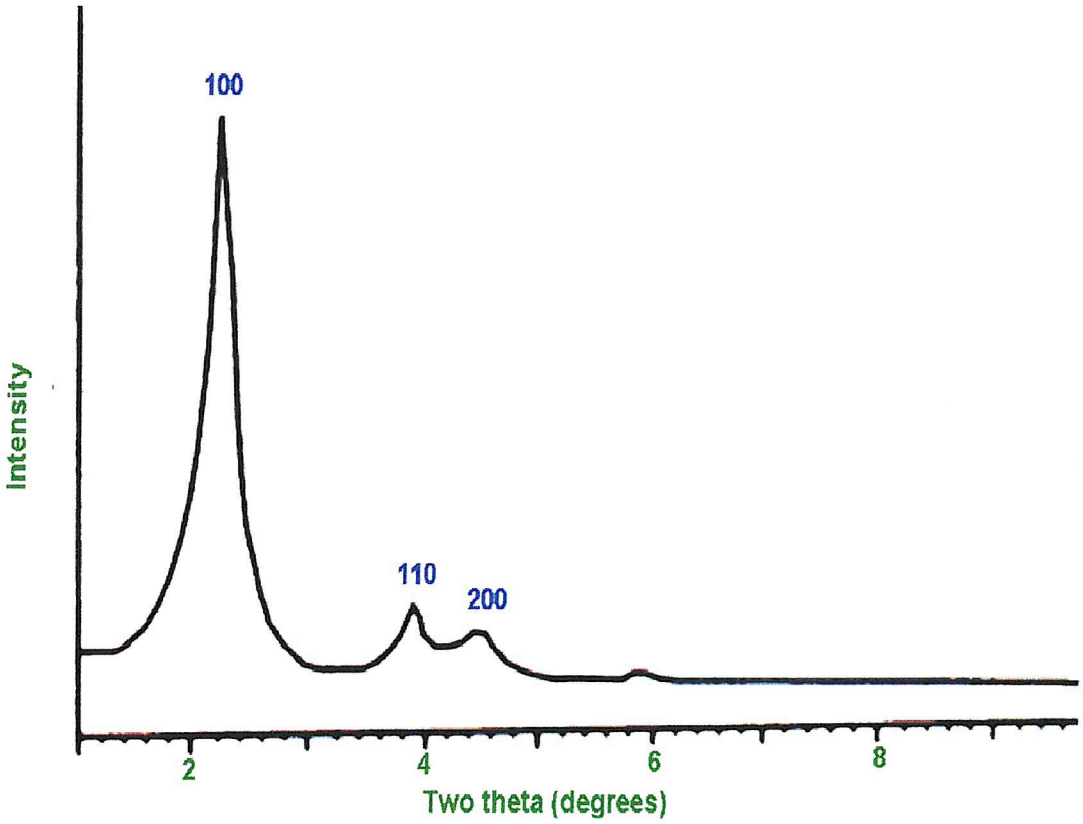

Figure 3.11 PXRD pattern of calcined MCM-41(B)

MAS NMR Spectroscopy

^{29}Si MAS NMR spectra of this compound, recorded at a spinning speed of 5 kHz, were very similar to the ones for other siliceous MCM-41 materials. In the spectra of the as-synthesised samples, differences in the positions of the template can be seen. However, for the ^{13}C NMR spectra, once calcined, there is very little difference between the two materials. The ^{29}Si MAS NMR spectrum (figure 3.12) shows a single unsymmetrical broad peak centred around -100 ppm with a partially visible shoulder suggesting a distribution of Si-O-Si bond angles.[15]

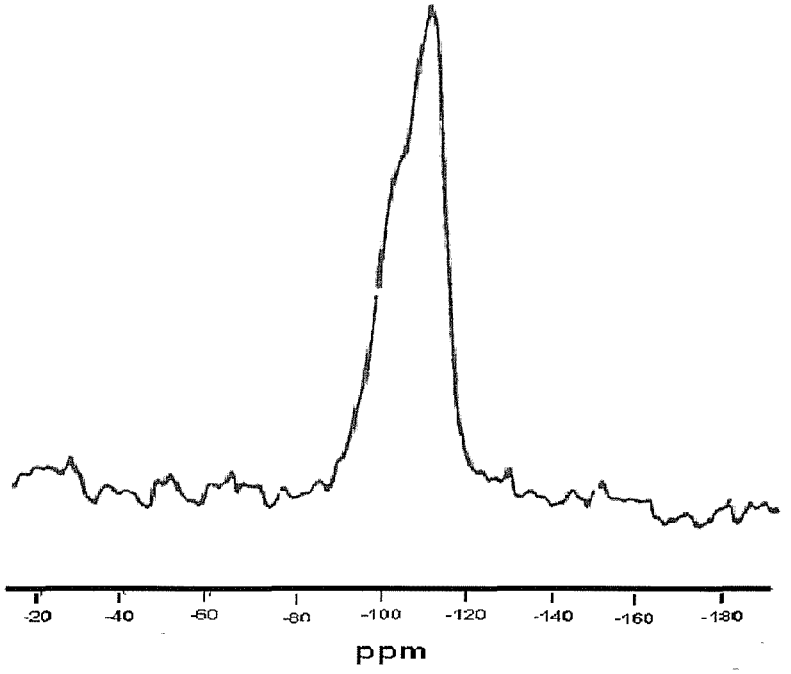

Figure 3.12 ^{29}Si 5 kHz MAS NMR of MCM-41(B)

Transmission Electron Microscopy

The photograph of the transmission electron micrograph of this material shows a hexagonal array of uniform channels as expected (figure 3.13). Enlarged photographs of these channels allowed a pore diameter of 24.3 Å to be determined with the pore wall thickness measuring 14 Å.

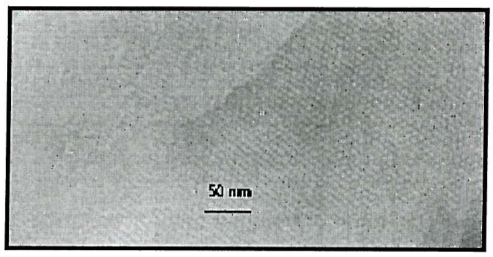

Figure 3.13 TEM of MCM-41(B)

BET Surface Area Measurements

Porosity measurements obtained from the Gemini 2375 gave a surface area of 1182 m^2g^{-1} with a maximum sorption of 351 cc g of N_2 at 228.3 mmHg.

The results from experiments at the Laboratoire de Chimie Organometallique de Surface, Villeurbanne, France, gives a BET surface area of 1481 m^2g^{-1}. The porous volume was calculated to be 44.9 cm^3g^{-1} and the pore size distribution graph (figure 3.14) determined a pore size of 18.9 Å.

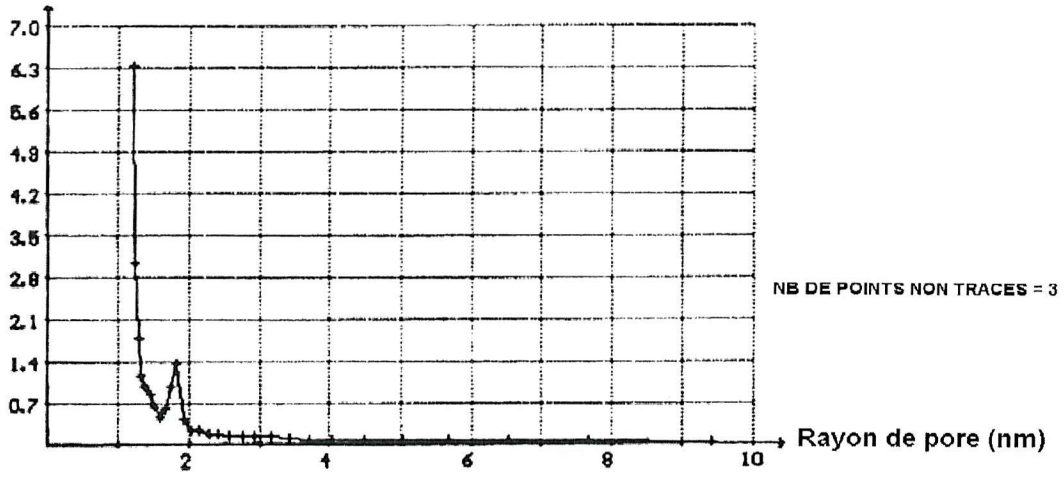

Figure 3.14 Pore size distribution graph for MCM-41(B)

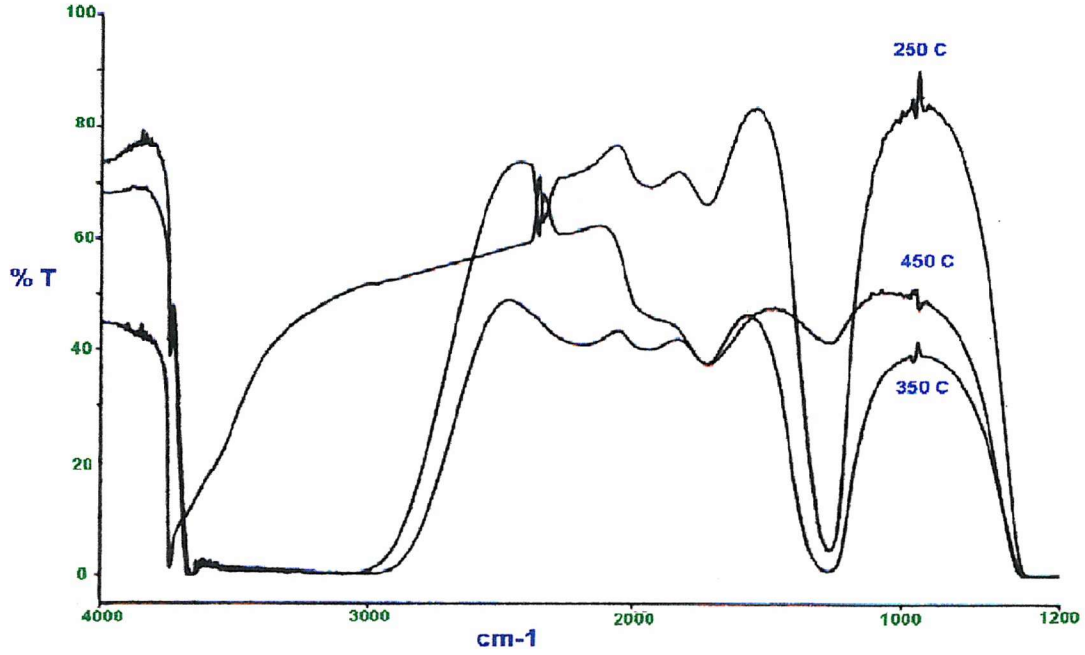

Figure 3.15 Infra-red spectra of MCM-41(B) from 250°C-450°C

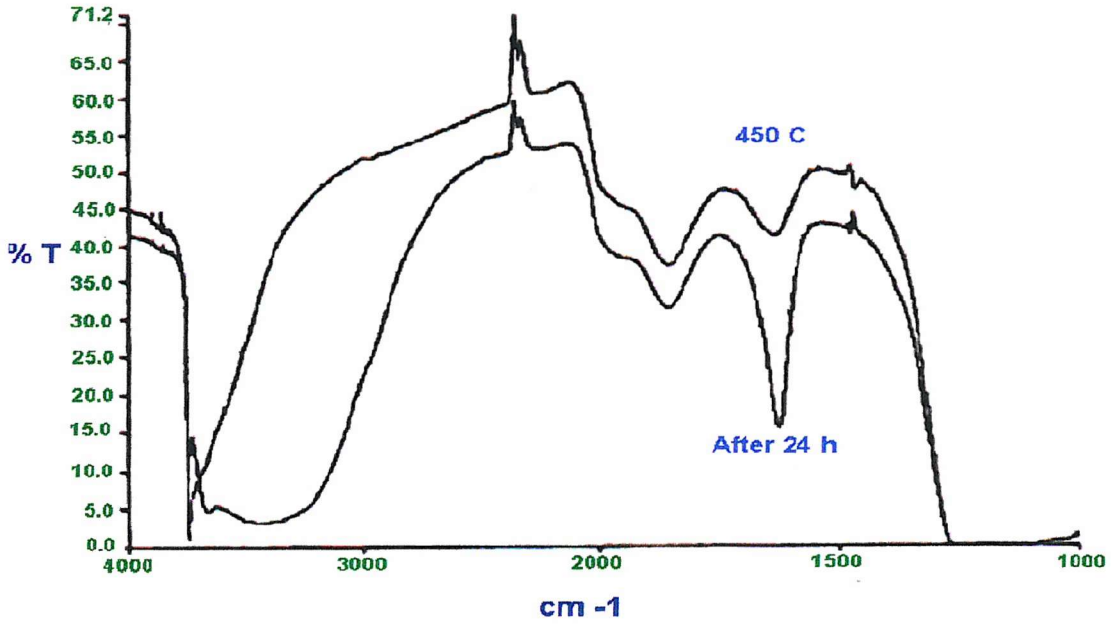

Figure 3.16 IR of MCM-41(B) after 24 h

Infra-red Spectrometry

A compressed disk was made of some of the material and this was placed in the infra-red cell. This was heated to calcination temperature (450°C) in increments of 100°C for a period of 5 h each time and an IR spectrum measured at each increment (figure 3.15). From the IR, it can be seen that no noticeable reduction in the water content is apparent until 450°C at which point the water band decreases significantly. The band at 1860 cm^{-1} is relatively unchanged throughout the experiment but the band at 1630 cm^{-1} shows a significant decrease in intensity.

The sample was left for 24 h and it was noted that water had reabsorbed onto the material (figure 3.16) with a broad band between 3650-2800 cm^{-1} and the band at 1630 cm^{-1} increasing in intensity. On reheating at 450°C, the dehydrated spectrum was again obtained.

3.1.5 Synthesis of AlMCM-41

Sodium aluminate ($NaAlO_2$), (0.53 g) was added to the template solution of $C_{14}H_{29}(CH_3)_3NBr$ (2.0 g in 12.5 g of water). Tetramethylammonium silicate solution (12.5 g), HiSil silica (3.13 g) and tetramethylammonium hydroxide solution (1.78 g) were added with stirring. The mixture was transferred to an autoclave and was heated with stirring for 24 h at 100°C. The resulting solid product was filtered, washed with water and dried under vacuum. The white powdered product (4.52 g) was calcined as before in compressed air for 24 h followed by 48 h in flowing oxygen.

3.1.6 Characterisation of AlMCM-41

This material was characterised by PXRD, MAS NMR spectroscopy, TEM and BET surface area measurements.

Powder X-ray Diffraction

The PXRD pattern for AlMCM-41 can be seen in figure 3.17 and shows the three characteristic peaks of a hexagonal lattice[16] array with a unit cell of approximately 40 Å.

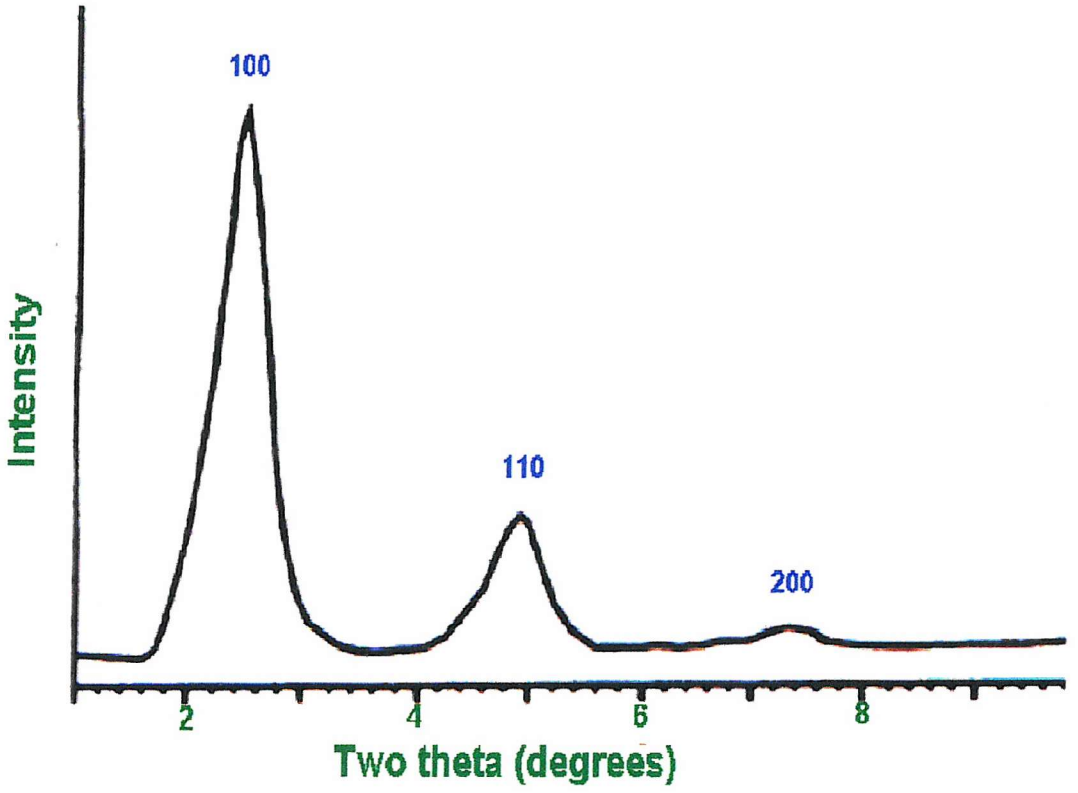

Figure 3.17 PXRD pattern of calcined AlMCM-41

MAS NMR Spectroscopy

The ^{29}Si MAS NMR spectrum (figure 3.18) shows a broad peak centred around -100 ppm which, as with the other MCM-41 materials, is typical of an amorphous structure. The ^{27}Al spectrum (figure 3.19) has two broad peaks in an approximate 3:1 ratio. The larger one at 63.3 ppm indicates tetrahedral co-ordination of the aluminium to the silicon and the smaller peak at 3.5 ppm is indicative of octahedral co-ordination.[17] The 6 co-ordinated aluminium

could be due to hydrated Al^{3+} cations formed in the reaction mixture and would remain within the pores to neutralise any framework charge but might be removed on washing and heating.

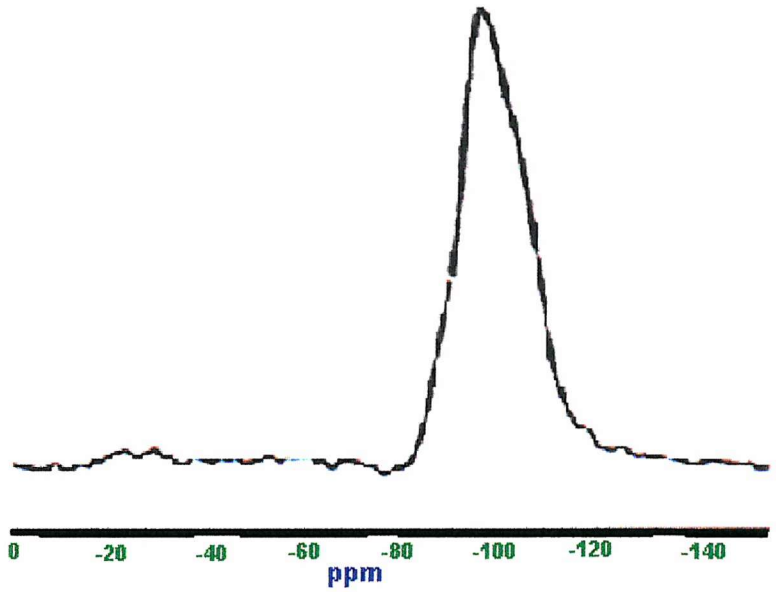

Figure 3.18 ^{29}Si 4.5 kHz MAS NMR spectrum of AlMCM-41

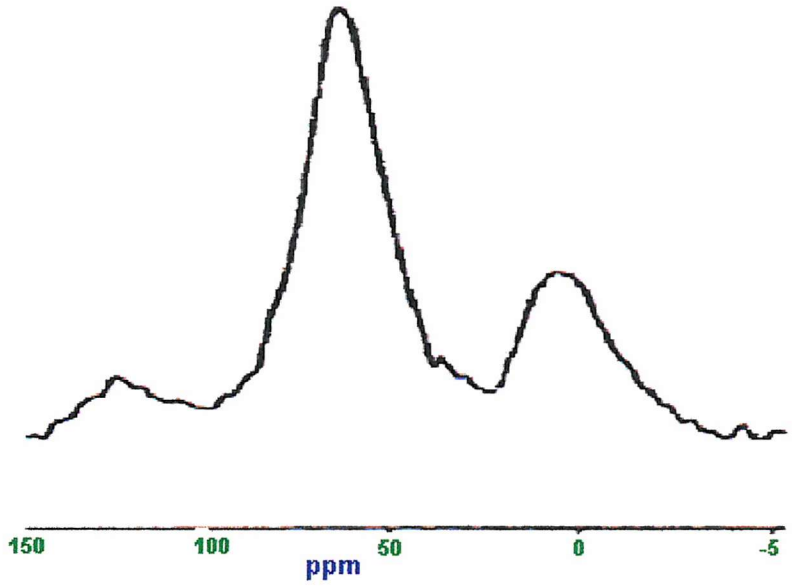

Figure 3.19 ^{27}Al 4.5 kHz MAS NMR spectrum of AlMCM-41

Transmission Electron Microscopy

The transmission electron micrograph of this material (figure 3.20) shows a clear hexagonal array of channels, each pore being surrounded by six others. Direct measurement from enlarged photographs gave a pore diameter of 21.9 Å with a wall thickness of 13.5 Å.

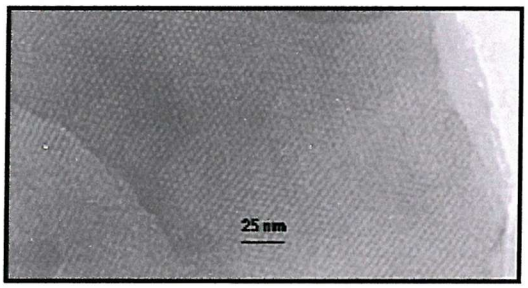

Figure 3.20 TEM of AlMCM-41

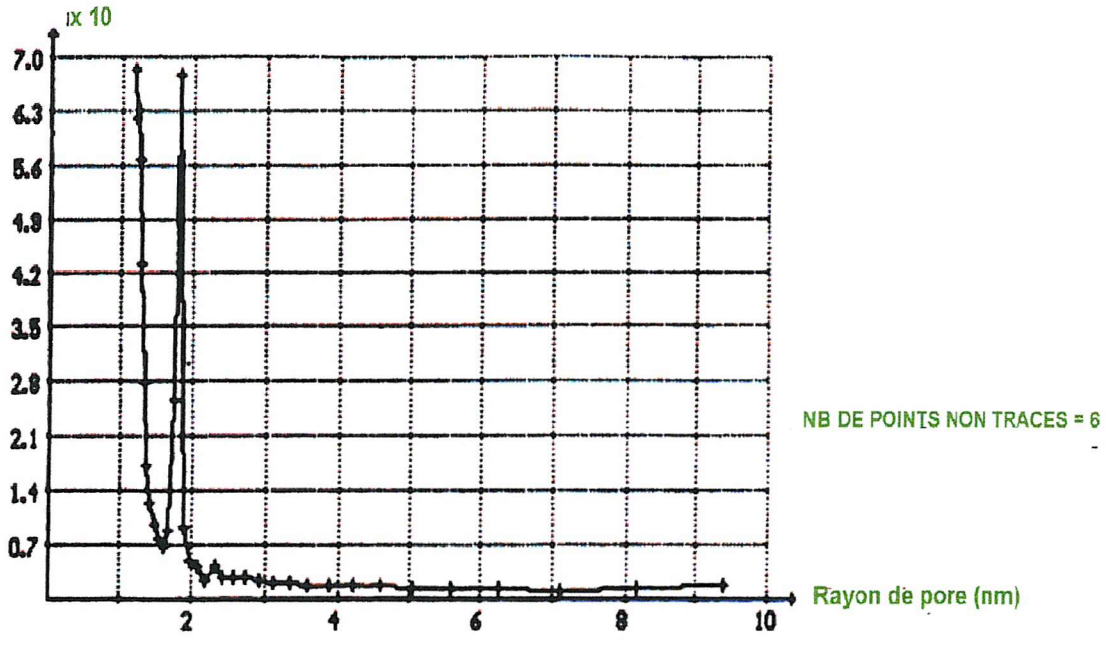

Figure 3.21 Pore size distribution graph for AlMCM-41

BET Surface Area Measurements

Porosity measurements from the Gemini 2375 gave a surface area of 758 m^2g^{-1} with a maximum sorption of 233 cc g^{-1} of N_2 at 228.3 mmHg.

The results from the experiments at the Laboratoire de Chimie Organometallique de Surface, Villeurbanne, France, gave a BET surface area of 848.8 m^2g^{-1}. The porous volume was calculated to be 27.8 cm^3g^{-1} and the pore size distribution graph (figure 3.21) allowed a pore diameter of 18.5 Å to be determined.

3.2 MESLC

The previous synthesis of mesoporous materials have used low template concentrations and a templating mechanism of cations and aggregates.[1] MESLC is a mesoporous material formed by templating silica mesostructures from ordered liquid crystalline surfactants[18] with the pores being formed by the organic mesophase.[19] At high template concentrations, the template/silica/water phase diagram is similar to that of template/water alone and this allows a degree of predictability in the synthesis. This technique also has the advantage of much faster production of the crude product (hours instead of days) and the resultant material is more crystalline than the MCM-41 materials.

3.2.1 Synthesis of MESLC

The octaethylene glycol monohexadecyl ether ($C_{16}EO_8$) template, (800 mg), TMOS (400 mg) and acidified H_2O (pH = 2; 400 mg) in a 2:1:1 molar ratio were swirled together in a small reaction vessel. Methanol was released and this was removed on a rotary evaporator over water at approximately 30°C. The crude product was then calcined in compressed air for 24 h followed by oxygen for 24 h. The resultant materials (0.45 g) were hard translucent crystals.

3.2.2 Characterisation of MESLC

Calcined MESLC was characterised by PXRD, MAS NMR spectroscopy, BET surface area measurements and Transmission electron microscopy.

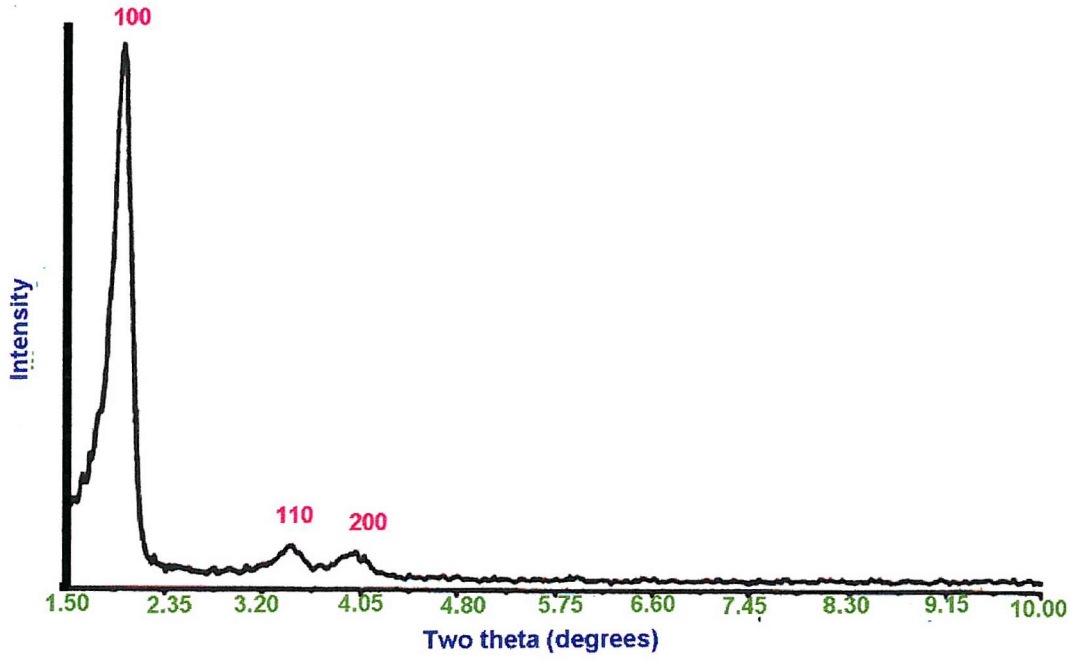

Figure 3.22 PXRD pattern of MESLC

Powder X-ray Diffraction

The PXRD spectrum (figure 3.22), shows the three characteristic peaks for a mesoporous material with a unit cell of approximately 40 Å. The increased crystallinity of this material allows a more resolved spectrum to be obtained. This also suggests that, to some extent, this material has some long range order.

BET and Transmission Electron Microscopy

BET surface area measurements were performed on powdered, dehydrated samples of the calcined material. Measurements obtained from the Gemini 2375 gave a surface area of 1388 m^2g^{-1} which is comparable with literature values for other mesoporous materials.[20,21,22]

The transmission electron micrograph (figure 3.23) shows a hexagonal array of channels which give a pore diameter of 28.4 Å and a wall thickness of approximately 11 Å. This material was found to be sensitive to high beam intensities and the structure was seen to disintegrate at very high magnifications.

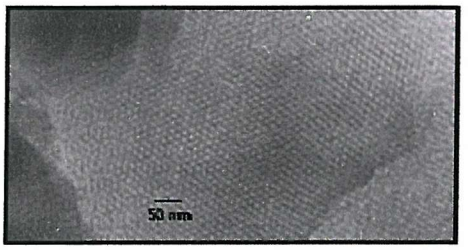

Figure 3.23 TEM of MESLC

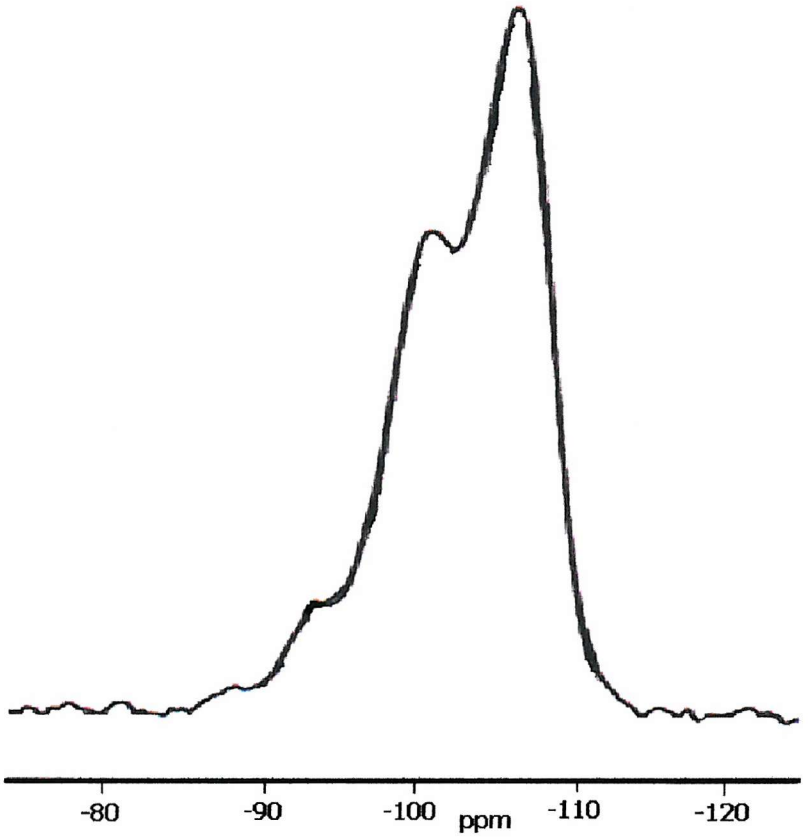

Figure 3.24 ^{29}Si 5 kHz MAS NMR of MESLC

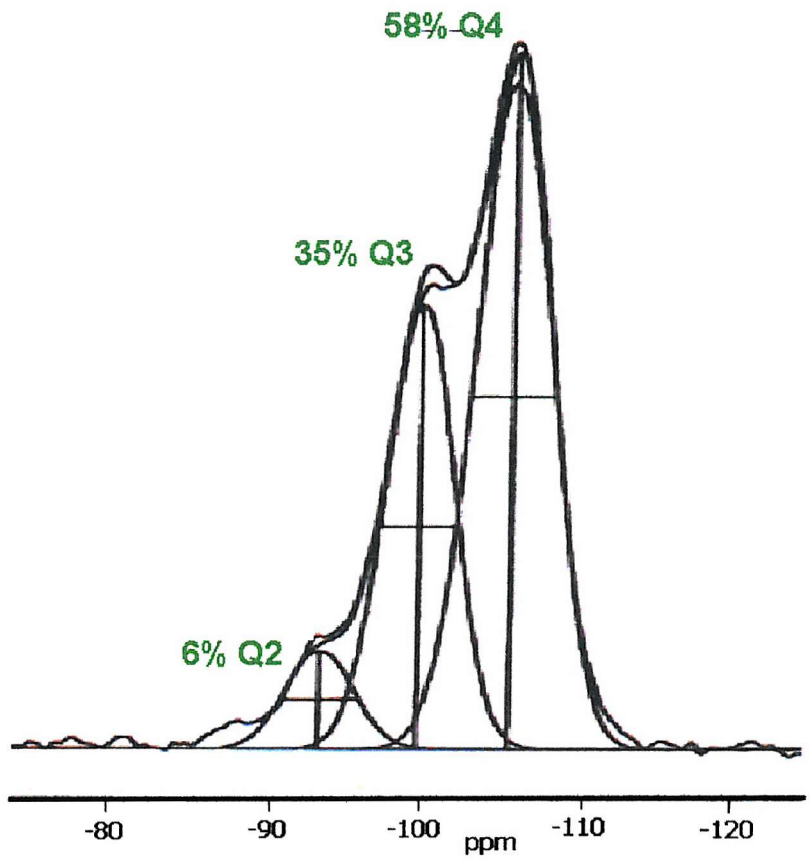

Figure 3.25 ^{29}Si 5 kHz MAS NMR of MESLC with curve-fitting

MAS NMR Spectroscopy

The ^{29}Si MAS NMR spectrum (figure 3.24) shows a broad band centred around -105 ppm with a definite shoulder at -100 ppm. The spectrum resembles that of amorphous silica, but on application of a curve-fitting program (figure 3.25), the ratios of silica sites, Q4:Q3:Q2 were determined to be 58:35:6 which suggests that this material contains less bulk silica and more silanol groups, *i.e.*, a greater number of $Si(OSi)_x(OH)_x$ (where x = 1 or 2) per square metre than the MCM-41 materials.

3.3 KMES

This mesoporous material was made according to the Klinowski method[23] where the channel diameters are controlled using an aged gel mixture.[24] Channel diameters of MCM-41 type materials are controlled by using templates with alkyl chains of differing lengths, but ageing the products in the original reaction mixture has been used to increase channel sizes. Using this concept, siliceous mesoporous silica was prepared resulting in a thick-walled MCM-41 silica with higher stability (withstanding calcination up to 1000°C) but having a lower surface area.

3.3.1 Synthesis of KMES

Trimethylammonium hydroxide, [(TMA)OH] (0.95 g, 1.23×10^{-2} mol) and cetyl trimethylammonium bromide, [(CTA)Br] (1.35 g, 0.15 mol) were added to de-ionised water (200 ml) with stirring at 30°C until the solution became clear. Fumed silica (5.2 g) was added with stirring for 2 h and then the mixture was aged for 24 h. The mixture was transferred to an autoclave and heated to 70°C for 48 h. The white powdery product was filtered hot, washed with distilled water and calcined at 550°C for 24 h in compressed air followed by 24 h in oxygen resulting in 6.2 g of the calcined silica.

3.3.2 Characterisation of KMES

This material was characterised by PXRD, MAS NMR spectroscopy, TEM and BET surface area measurements.

Powder X-ray Diffraction

Figure 3.26 is the powder X-ray diffraction pattern for KMES showing the three characteristic peaks of a hexagonal lattice with a unit cell of approximately 40 Å.

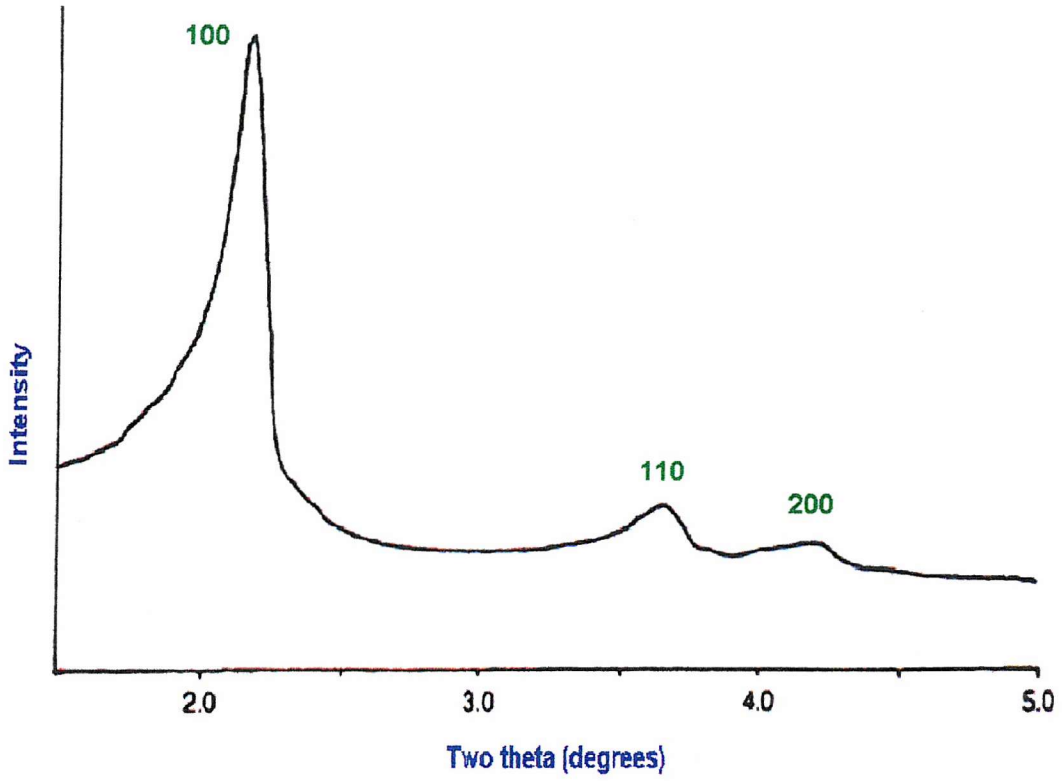

Figure 3.26 PXRD pattern of KMES

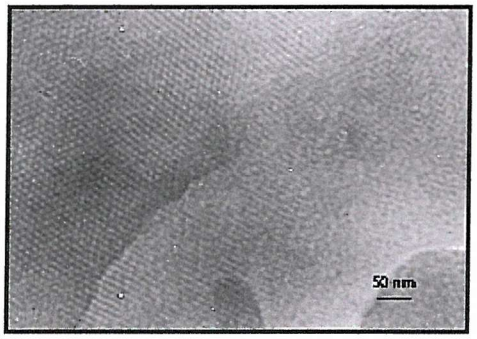

Figure 3.27 TEM of KMES

BET and Transmission Electron Microscopy

Measurements made on the Gemini 2375 on dehydrated samples gave a surface area of 1455 m^2g^{-1} which is very close to literature values for this material.

The transmission electron micrograph, (figure 3.27) shows a hexagonal array of atoms as is expected for a MCM type material, with a pore to pore diameter of 39.2 Å, consisting of a pore diameter measuring 27.2 Å and the wall thickness measuring 12 Å. This material was very beam sensitive and became unstable above 50,000 magnification.

MAS NMR Spectroscopy

The ^{29}Si MAS NMR spectra (figure 3.28) of the material consists mainly of two distinct resonances at -100 ppm and -110 ppm. These can be attributed to Q4 sites [$Si(OSi)_4$] and Q3 sites [$Si(OSi)_3OH$]. The resemblance to amorphous silica is evident and the proportion of silanol units per square metre would be small.

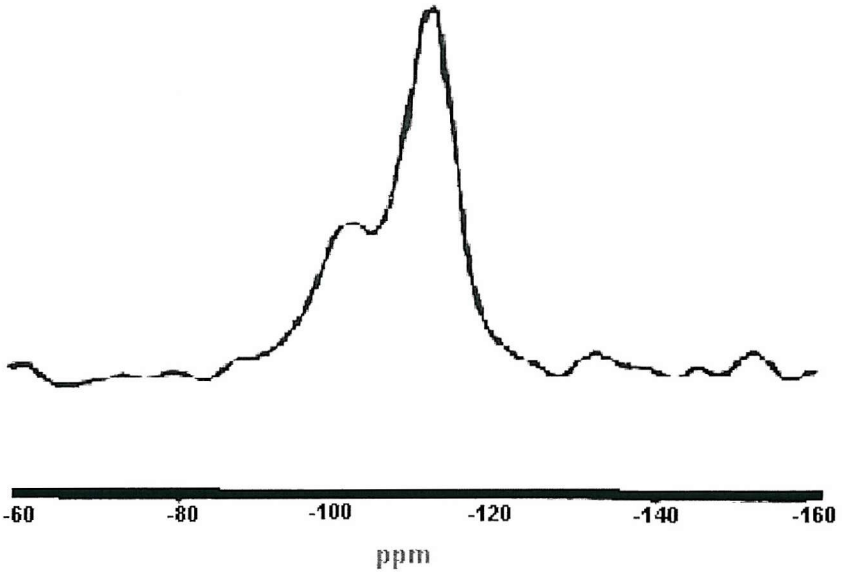

Figure 3.28 ^{29}Si 4.8 kHz MAS NMR of KMES

3.4 Discussion

All the mesoporous materials synthesised have regular hexagonal pores which can clearly be seen in the TEM pictures. The pore diameters and the results of the BET surface area measurements differ from results quoted in literature.

Table 3.2 shows the difference in pore diameters obtained from three different MCM-41 syntheses. The diameters quoted in literature by Beck *et al*[1,2] for these compounds are far larger than were noted for any of the like compounds made here in this research. MCM41(B), made from the larger template is expected to have a larger pore width and does so in both experiments used in this research, however the pore size distribution graphs from the Laboratoire de Chimie Organometallique de Surface (LCOS), Villeurbanne, do not give significantly different pore diameters. On the contrary, the difference between the three materials is negligible. The pore diameters as measured from the TEM pictures are significantly different with MCM41(A) made from the smaller template, having a smaller pore diameter as expected.

	Pore diameter from TEM/Å	**Pore diameter from LCOS/Å**	**Pore diameter from literature/Å**
MCM-41(A)	22.3	18.8	22
MCM-41(B)	24.3	18.9	30
AlMCM-41	21.9	18.5	34

Table 3.2 Pore diameters of the MCM-41 silicas.

MCM41(B) was made with a template with a longer chain length and has a larger pore size therefore, as expected, from table 3.3 it can be seen that this material has a smaller surface area than the other siliceous material MCM41(A). The larger the chain length, the larger the pore size and therefore, the less channels there are going through the material. With less channels, the surface area will be less. This is confirmed by the difference in the sorption of N_2 by both materials at maximum pressure. MCM41(A) having a smaller pore size and more internal channels, absorbs more gas than MCM41(B).

	Surface area from Gemini II/m^2g^{-1}	Surface area from LCOS/m^2g^{-1}	Porous volume /cm^3g^{-1}
MCM-41(A)	1422	1646	65.6
MCM-41(B)	1182	1481	44.9
AlMCM-41	758	848	27.8

Table 3.3 BET surface area and porous volume values for the MCM-41 materials.

There is little literature to compare the surface area of the aluminosilicate to but a surface area above 700 m^2g^{-1} is a good indication that a mesoporous rather than microporous material has been formed.

The difference between the two sets of data could simply be due to different experimental techniques. However, Branton *et al*[25] performed physisorption experiments on MCM-41 materials and found a surface area of 655 m^2g^{-1}. This is lower than the patented value and lower than the values noted in this research. They also noted effective pore diameters in the range of 33 - 43 Å. This is closer to the values quoted by Beck *et al.*[1] Branton *et al*[25] obtained their samples of MCM-41 from the patent source and thus the results are similar. It can be assumed that the pore size is highly sensitive to the reaction conditions. Slight variations can lead to alternative pore sizes which is what is seen here.

As the data from both this research and from the results from the Laboratoire de Chimie Organometallique de Surface verify that the samples are mesoporous materials with a hexagonal arrangement of channels, pore sizes above 15 Å and surface areas above 700 m^2g^{-1}, both can be considered valid.

The data from the Laboratoire de Chimie Organometallique de Surface does have the advantage of giving porous volume measurements. This could be very useful when modification of the mesoporous materials takes place as a change in porous volume could easily indicate adsorption or chemical grafting of complexes within the channels.

Table 3.4 shows the pore diameters and surface areas for the MESLC and KMES materials. There is less literature available for comparison as the techniques are different but both

materials have pore diameters and surface areas which fall within the mesoporous range.

	Pore diameter from TEM/Å	Pore diameter literature value/Å	Surface area/m^2g^{-1}	Surface area literature value/m^2g^{-1}
MESLC	28.4	28	1388	1400
KMES	27.2	26-36	1455	1462

Table 3.4 Pore diameters and BET surface area values for MESLC and KMES

These two mesoporous silicas have larger pore sizes than the MCM-41 materials but this could simply be due to the use of larger templates. However the surface area values for these materials is very close to the literature values which suggests that in these reactions, the pore size is not as sensitive to the reaction conditions as it is for the MCM-41 materials. Both these materials are more stable at higher calcination temperatures but both were found to be fairly sensitive to beam intensity during TEM experiments. Although the KMES silica was relatively stable, the NMR spectra showed a high amount of bulk silica. The MESLC silica is more of interest due to its increased crystallinity and also as the analysis of the NMR showed a higher amount of Q3 and Q2 silica which together with its large surface area would be useful in the anchoring of organometallic species.

3.5 Conclusions

Five types of mesoporous silicas have been synthesised and characterised by TEM, BET surface area measurements, powder X-ray diffraction, MAS NMR spectroscopy and infra-red spectroscopy. Synthesis with varying template chain lengths leads to varying pore diameters. All the mesoporous silicas are formed of hexagonal arrays of channels with wall thicknesses between 10-12 Å and pore diameters of 16-30 Å. BET studies have shown that the surface areas of these materials fall well within the range for mesoporous silicas, ranging from 700 - 1500 m^2g^{-1}. All the materials contain bulk Q4 silica but there is a significant amount of Q3 and Q2 silica within the structures to use them as hosts for organometallic species. The rest of this work will concentrate on MCM-41(A), MESLC and KMES as support materials.

3.6 References

1. Beck, J. S., Vartuli, J. C., *et al.*, *J. Am. Chem. Soc.*, 1992, **114**, 10834.
2. Beck, J. S., Vartuli, J. C., *et al.*, US Patent 5108725, 1992.
3. Kresge, C. T., Leonowicz, M. E., Roth, W. J., Vartuli, J. C., Beck, J. S., *Nature*, 1992, **359**, 710.
4. Monnier, A., *Science*, 1993, **261**, 1299.
5. Cheng, C.-F., Luan, Z., Klinowski, J., *Langmuir*, 1995, **11**, 2815.
6. Smith, J. V., Dytrych, W. J., *Nature*, 1984, **309**, 607.
7. Barrer, R. M., Villager, H. Z., *Krystallogr.*, 1969, **128**, 352.
8. Oster, G., Riley, D. P., *Acta Crystallogr.*, 1952, **5**, 272.
9. Klinowski, J. *Chem. Rev.*, 1991, **91**, 1459.
10. Maher, J. M., Cooper, N. J., *J. Am. Chem. Soc.*, 1980, **102**, 7606.
11. Brunner, E., *J. Catal.*, 1991, **127**, 34.
12. Bagshaw, S. A., Prouzet, E., Pinnavaia, T. J., *Science*, 1995, **269**, 1242.
13. Huber, C., Moller, K., Bein, T., *J. Chem. Soc., Chem. Commun.*, 1994, 2619.
14. Nedez, C., Ph. D. Thesis, l'Universite Claude Bernard-Lyon I, 1992.
15. Engelhardt, E., Michel, D., High Resolution Solid State NMR of Silicates and Zeolites, Wiley, Chichester, 1987.
16. Cheng, C.-F., Zhou, W., *J. Chem. Soc., Faraday Trans.*, 1997, **93**, 359.
17. Anderson, M. W., Klinowski, J., Xinsheng, L., *J. Chem. Soc., Chem. Commun.*, 1984, 1596.
18. Mitchell, D. J., Tiddy, G. S., *J. Chem. Soc., Faraday Trans.*, 1983, **79**, 975.
19. Attard, G. S., Glyde, J. C., Goltner, C. G., *Nature*, 1995, **378**, 366.
20. Behrens, P., *Adv. Mater.*, 1993, **5**, 127.
21. Behrens, P., Stucky, G. D., *Angew. Chem. Int. Ed. Engl.*, 1993, **32**, 696.
22. Alfredsson, V., *J. Chem. Soc., Chem. Commun.*, 1994, 921.
23. Cheng, C.-F., Klinowski, J., *Chem. Phys. Letters*, 1996, **263**, 247.
24. Kushalani, D., Kuperman, A., Ozin, G. A., Tanaka, K., Garces, J., Olken, M. M., Coombes, N., *Adv. Mater.*, 1995, **7**, 842.

25. Branton, P. J., Hall, P. G., Sing, K. S. W., Reichert, H., Schuth, F., Unger, K. K., *J. Chem. Soc., Faraday Trans.*, 1994, **90**, 2965.

CHAPTER FOUR

Metal-alkyl Modified Mesoporous Silicas

4.0 Introduction

This chapter describes the preparation and characterisation of mesoporous silicas MCM-41(A) modified with trimethylgallium and diethylzinc using a direct and an indirect method of metal-alkyl introduction to investigate the interaction of simple metal alkyl species with mesoporous-type silicas. The vapour phase interaction of trimethylgallium and diethylzinc with MCM-41(B), MESLC and KMES mesoporous silicas are also described.

Organometallic compounds of aluminium, gallium and zinc are of interest due to a wide range of possible uses; for example, as precursors in ceramics, as reagents in organic syntheses[1,2] or as highly active co-catalysts for the metathesis of alkenes and alkynes and the polymerisation of olefins.[3-6] Trialkylgallium compounds are mild Lewis acids and tend to be monomeric containing tri-coordinate gallium in solution and in the gas phase but can become four-coordinate species under certain conditions. They react with weak Brønsted acids such as water, alcohols and thiols but the reactivity toward these weak acids is less than that of corresponding alkylaluminium compounds. Similarly, alkylzincs are also mild Lewis acids and are generally found as a dimer in the liquid form. Their reactivity is similar to alkylaluminium compounds giving it a stronger reactivity with weak Brønsted acids than alkylgallium. The reactivity of organo-gallium type compounds has been much studied[7,8] but there is relatively little study on the simple metal alkyls such as trimethylgallium and diethylzinc. These, therefore, make ideal compounds to study the surface chemistry of silica materials being relatively small, discrete and highly reactive. The interaction of the surface silanol groups of the silica with alkyl gallium and zinc make ideal test reactions as well as paving the way for more complex interactions between alkyl-metals and complexes supported on the silicas. It is quite likely that when a supported complex is alkylated, the surface of the support will also be alkylated, thus the necessity of prior studies to clarify the two types of interaction on analysis.

As both trimethylgallium and diethylzinc are pyrophoric liquids, the safest method of study was deemed to be via EXAFS using *in situ* reactions. A specially adapted cell was designed to allow metal alkyl vapours to enter and leave the system without exposure to the air.

4.1 MCM-41(A) modified with $Ga(CH_3)_3$ - direct reaction

MCM-41(A) (0.25 g) was dehydrated under vacuum at 200°C for 2 h. Trimethylgallium (1 μl/g) was introduced to the silica in an inert atmosphere via a micro-syringe and the silica was left in the trimethylgallium atmosphere for 24 h. The reaction vessel was then placed under vacuum to remove any residual vapour, and the remaining sample was stored in argon.

4.1.1 EXAFS analysis of MCM-41(A) modified with $Ga(CH_3)_3$ - direct reaction

The XAS experiments on this sample were carried out on Station 9.2 at the Daresbury Laboratory. All manipulations of the sample took place in a glove box. The sample was attached to an EXAFS cell by slurrying in dry anhydrous pentane and then, using a pipette, the suspension was placed on the surface of the cell. Allowing the pentane to evaporate off, a thin layer of the solid sample was left on the cell. This was repeated as many times as necessary to completely coat the surface of the cell with an even layer. The cell was placed in the path of the beam and attached to a vacuum line and temperature probe. A series of temperature conditions were applied to the system to determine if any effects take place due to the temperature change.

MCM-41(A)/$Ga(CH_3)_3$ at room temperature

Figure 4.1 shows the Ga K-edge EXAFS data and Fourier transform with one main peak centred around 2.0 Å. Initially fitting the data to a model of pure trimethylgallium was not successful therefore working on the assumption that some reaction has occurred with the silica surface, the best fit was found to be one that corresponded to three shells of carbon or oxygen, silicon and gallium, respectively.

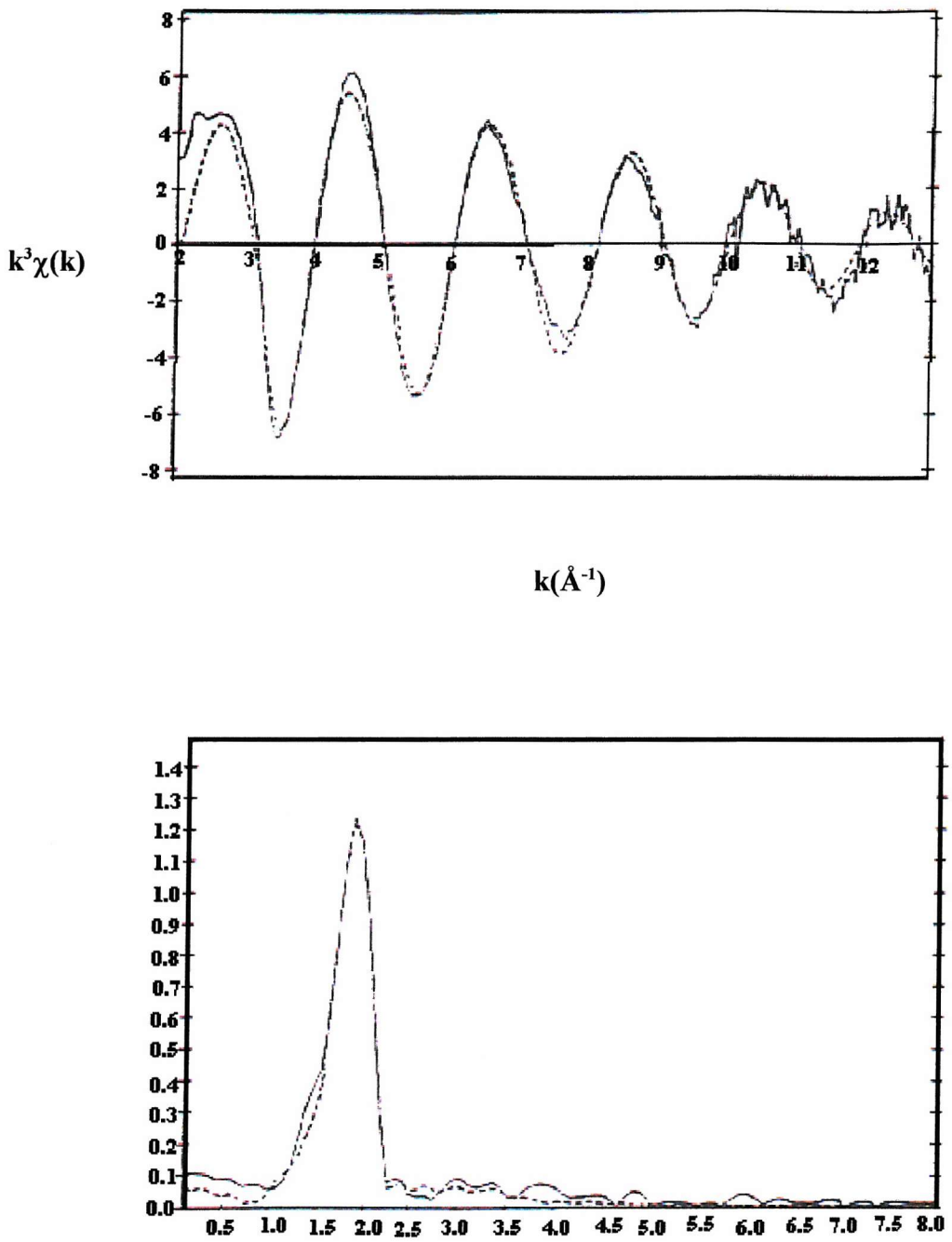

Figure 4.1 Ga k^3-weighted EXAFS data and Fourier transform of MCM-41(A)/ $Ga(CH_3)_3$/room temperature; phase shift corrected for C.

(— Experimental, ----- Theory)

The EXAFS data for this reaction was modelled to a first co-ordination sphere of four atoms of carbon at 1.938(4) Å (table 4.1). The similarities in the bond lengths of the carbon of the methyl group and the oxygen of the silanol group made it difficult to separate this data into two shells of carbon and oxygen but the detection of a second shell of one silicon at 2.521(3) Å suggests that some interaction with the surface has occurred. The presence of a third shell which was determined to be a Ga-Ga interaction of 3.211(6) Å was not wholly unexpected as this sample was untreated and was assumed to have excess trimethylgallium trapped in the pores of the silica. The silicon and gallium shells were statistically significant at the 95% probability level and the inclusion of these two shells resulted in a reduction of the R-factor from 59.2% to 48.5% to 43.4%, respectively.

N[a]	R/Å	A/Å^{2}[b]
4C	1.938(4)	0.008(1)
1Si	2.521(3)	0.022(1)
1Ga	3.211(6)	0.033(2)
R-factor = 43.4%; E_f = -7.41 eV		

[a]Coordination number; [b]Debye-Waller factor A = $2\sigma^2$, σ = mean square internuclear separation. Statistical errors derived in excurv92 given in parentheses.

Table 4.1 Ga K-edge EXAFS derived structural parameters for MCM-41(A)/Ga$(CH_3)_3$/ at room temperature.

MCM-41(A)/Ga$(CH_3)_3$ - 100°C

In the next stage of the experiment, the sample was heated up to 100°C and held at this temperature whilst the scans of the sample were run. Figure 4.2 shows the Ga K-edge EXAFS data and Fourier transform of the sample at 100°C. Analysis of the data (table 4.2) gave a first co-ordination sphere of two carbon atoms at 1.997(2) Å and a second shell of two oxygens at 1.843(1) Å. In this analysis, two separate shells were justified. This data, fitted to a single shell of four atoms, gives a high R-factor of 41 % and a highly negative Debye-Waller factor. Shifting from one to two shells reduces the R-factor drastically to 11.2%. The detection of oxygen suggests some interaction with the silica surface. A shell of silicon atoms was fitted to the data but this resulted in an increase in the R-factor and a

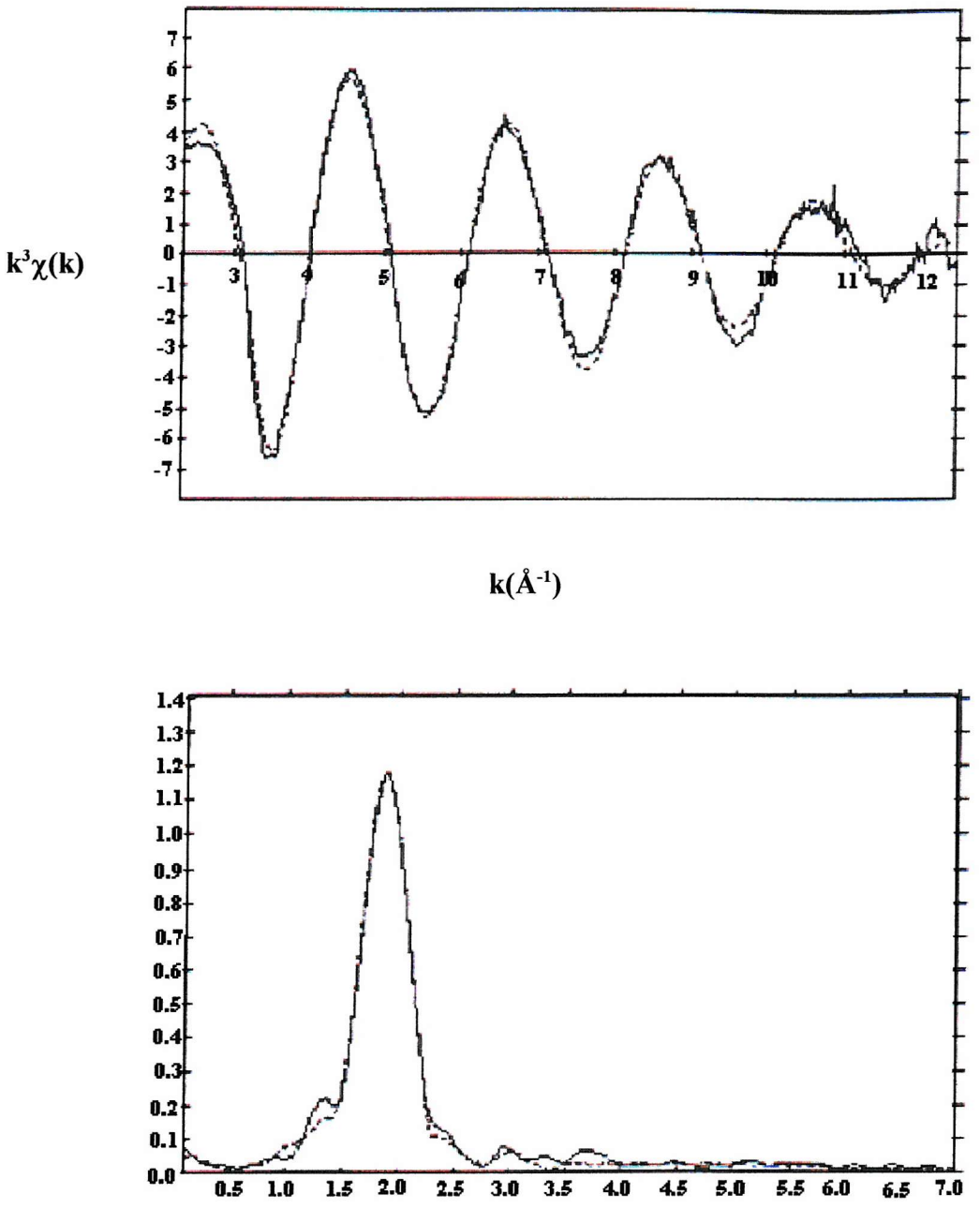

Figure 4.2 Ga k^3-weighted EXAFS data and Fourier transform of MCM-41(A)/ $Ga(CH_3)_3$/100°C; phase shift corrected for C.

(— Experimental, ----- Theory)

negative Debye-Waller factor. Gallium was also fitted to this data at 3.004 Å but this shell was statistically insignificant and is not presented

N[a]	R/Å	A/Å^{2b}
2C	1.997(2)	0.019(3)
2O	1.843(1)	0.025(2)
R-factor = 11.2%; E_f = -8.89 eV		

[a]Coordination number; [b]Debye-Waller factor A = $2\sigma^2$, σ = mean square internuclear separation. Statistical errors derived in excurv92 given in parentheses.

Table 4.2 Ga K-edge EXAFS derived structural parameters for MCM-41(A)/Ga(CH$_3$)$_3$/ 100°C.

MCM-41(A)/Ga(CH$_3$)$_3$ - 100°C, under vacuum

In this last stage of the experiment, the chamber was placed under vacuum (1.5 x10^{-3} atm) to remove any unreacted gas. Figure 4.3 shows the Ga K-edge EXAFS data and the Fourier transform. Analysis of the data (table 4.3) shows two shells of carbon and oxygen at 1.974(5) Å and 1.861(3) Å, respectively which had an R-factor of 48%. With the excess trimethylgallium removed, a shell of two silicon atoms was fitted at 3.362(2) Å with a corresponding reduction in the R-factor to 20% suggesting the loss of a single methyl group and a structure consisting of a dimethylgallium species interacting with the surface of the silica via two silanol groups. A fourth shell of one gallium atom was also fitted at 2.983(1) Å which could be due to interaction between gallium atoms in proximity to one another or possibly that some gallium species remain trapped in the structure of the silica.

N[a]	R/Å	A/Å^{2b}
2C	1.974(5)	0.005(2)
2O	1.861(3)	0.008(1)
2Si	3.362(2)	0.023(1)
1Ga	2.983(1)	0.032(2)
R-factor = 13.6%; E_f = -8.72 eV		

[a]Coordination number; [b]Debye-Waller factor A = $2\sigma^2$, σ = mean square internuclear separation. Statistical errors derived in excurv92 given in parentheses.

Table 4.3 Ga K-edge EXAFS derived structural parameters for MCM-41(A)/Ga(CH$_3$)$_3$/ 100°C/under vacuum.

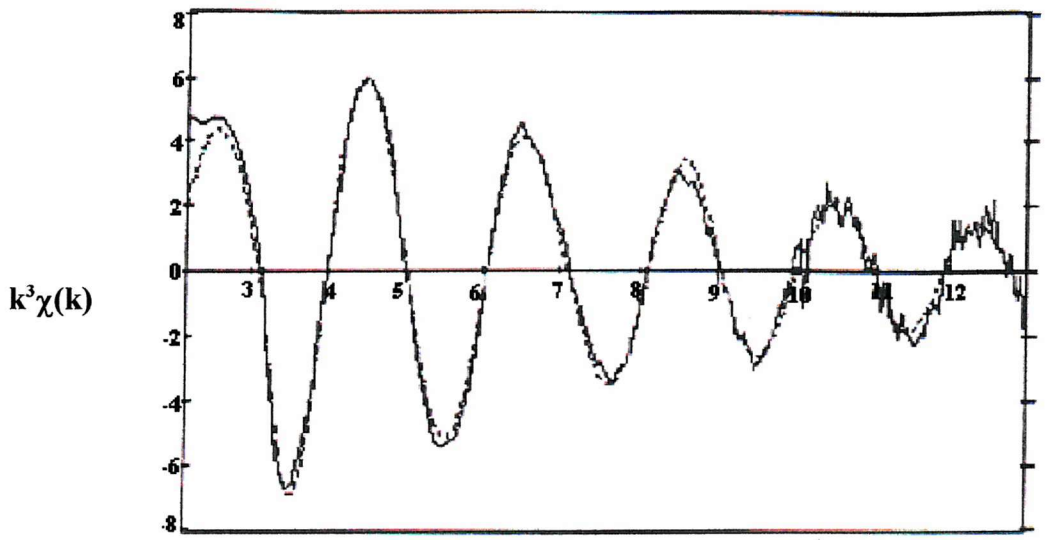

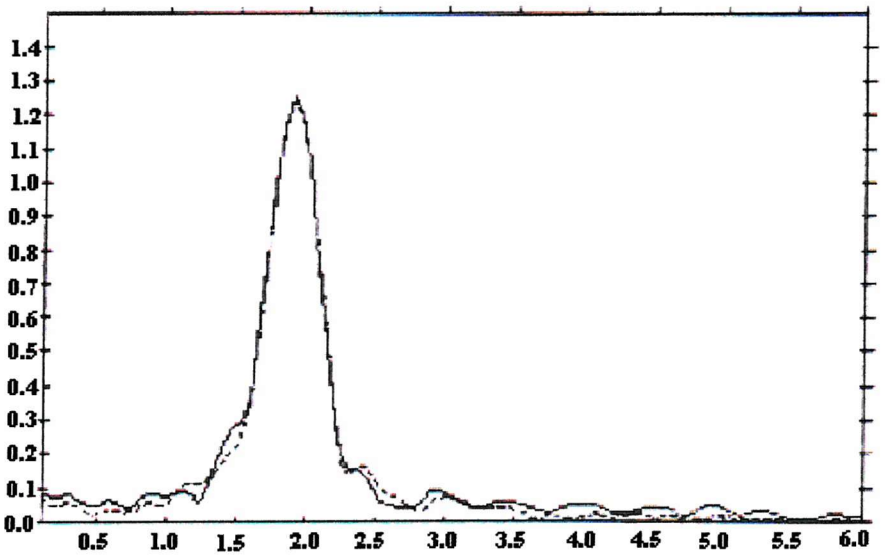

Figure 4.3 Ga k^3-weighted EXAFS data and Fourier transform of MCM-41(A)/ $Ga(CH_3)_3$/100°C/under vacuum; phase shift corrected for C. (— Experimental, ----- Theory)

4.2 MCM-41(A) modified with $Ga(CH_3)_3$ - vapour phase reaction

The XAS experiments on this sample were carried out on Station 9.2 at the Daresbury Laboratory. All manipulations of the sample took place in a glove box. MCM-41(A) (0.25 g) was dehydrated under vacuum at 200°C for 2 h. The silica was loaded onto the EXAFS cell as before, by slurrying the sample with anhydrous pentane to form a suspension and pipetting onto the surface of the cell to form an even layer. Once the sample was securely attached, the cell was placed in the path of the beam and attached to the vacuum system and a heating implement. A sealed cell containing trimethylgallium was connected to the EXAFS chamber. Figure 4.4 shows a diagram of the set-up of the apparatus. The system was evacuated and flushed with an inert gas several times to remove any contaminants.

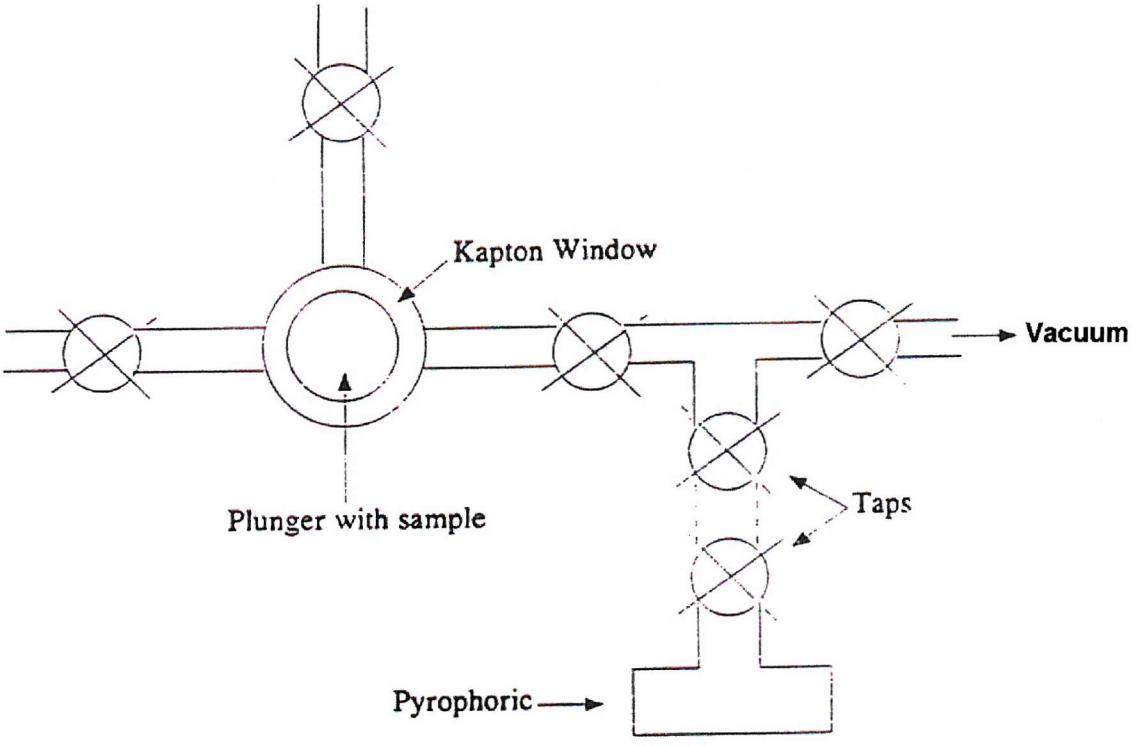

Figure 4.4 Apparatus for vapour phase reactions.

4.2.1 EXAFS analysis of MCM-41(A) modified with $Ga(CH_3)_3$ - vapour phase reaction

In the first stage of this experiment, the cell containing the trimethylgallium was heated via an air gun to vaporise the liquid. The joints leading to the EXAFS cell were also heated to facilitate movement of the vapour. The tap between the two cells was slowly opened and the silica was exposed to the vapour for 1 h before scanning the sample.

MCM-41(A)/$Ga(CH_3)_3$ vapour

Figure 4.6 is the Ga K-edge EXAFS data and the corresponding Fourier transform obtained from the silica exposed to the trimethylgallium vapour and shows a main peak centred around 2.0 Å with a second significant peak at 3.0 Å. In attempting to fit this data to the system, six models were proposed (figure 4.5). Model A assumes that surface interaction occurs via a single silanol group with loss of one methyl group and the gallium atom remaining tri-coordinate. Model B assumes surface interaction through two silanol groups with the gallium atom becoming four-co-ordinate. Model C assumes a trimethylgallium interaction with a silanol group without loss of methyl groups forming a four-coordinate gallium centre and no Ga-Ga interaction. Model D assumes that no reaction has occurred and that all that is detected is trimethylgallium. Models E and F assume interaction with silanol groups (as with A and B) but with interaction with a neighbouring gallium species.

The EXAFS data was fitted in turn to each of these models. Models A, B and C were discarded because Ga-Ga interaction was clearly prominent in all the analyses. Model D was also discarded because the data would not fit to a model of trimethylgallium vapour having a high R-factor (78%) and a negative Debye-Waller factor in the carbon shell. The data was fitted to the remaining two models, E and F, and whilst model E gave a relatively low R-factor of 43.3%, the best fit was obtained with model F (table 4.4). A first co-ordination sphere of two carbon atoms at 1.947(4) Å and a second shell of two oxygen atoms at 2.028(2) Å was fitted. Two separate shells as opposed to a single shell of four atoms was justified by a

drop in the R-factor to 31.5% (from 45%) and acceptable Debye-Waller factors. Model F was preferred over model E because despite them being very similar, a second shell of only one oxygen atom was impossible to fit well. A third shell of one gallium atom at 2.935(2) Å was also fitted which fits in with the theory of a neighbouring gallium species. Silicon, however, could not be fitted at this stage which was wholly expected due to excess trimethylgallium vapour in the chamber.

N[a]	R/Å	A/Å^{2}[b]
2C	1.947(4)	0.009(1)
2O	2.028(2)	0.031(2)
1Ga	2.935(2)	0.034(1)
R-factor = 31.5%; E_f = -8.01 eV		

[a]Coordination number; [b]Debye-Waller factor A = $2\sigma^2$, σ = mean square internuclear separation. Statistical errors derived in excurv92 given in parentheses.

Table 4.4 Ga K-edge EXAFS derived structural parameters for MCM-41(A)/Ga(CH$_3$)$_3$ vapour.

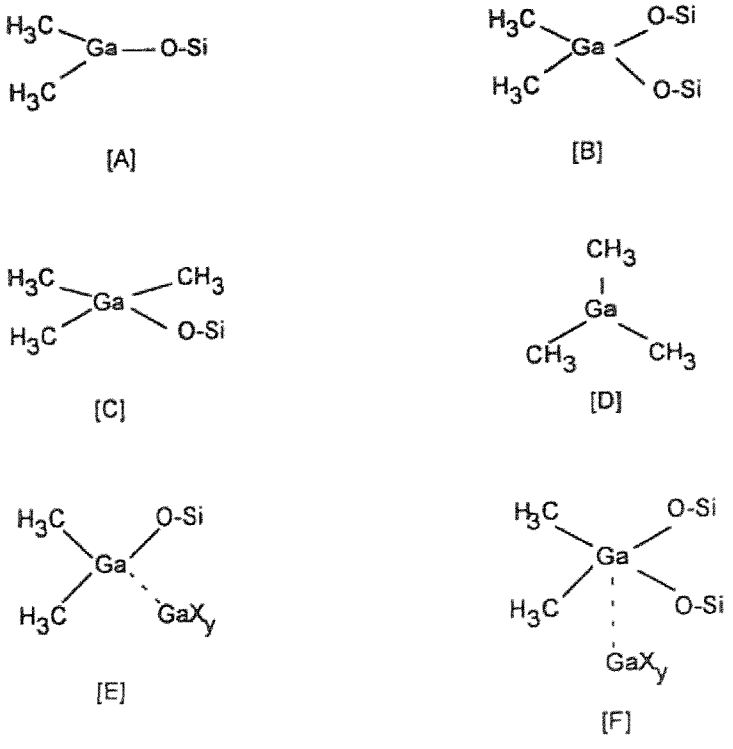

Figure 4.5 Models A - F

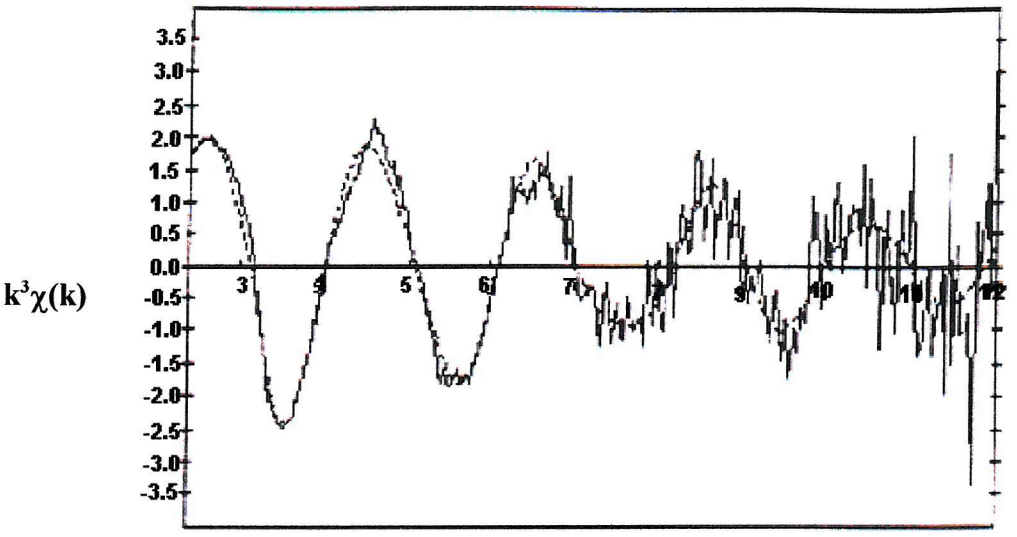

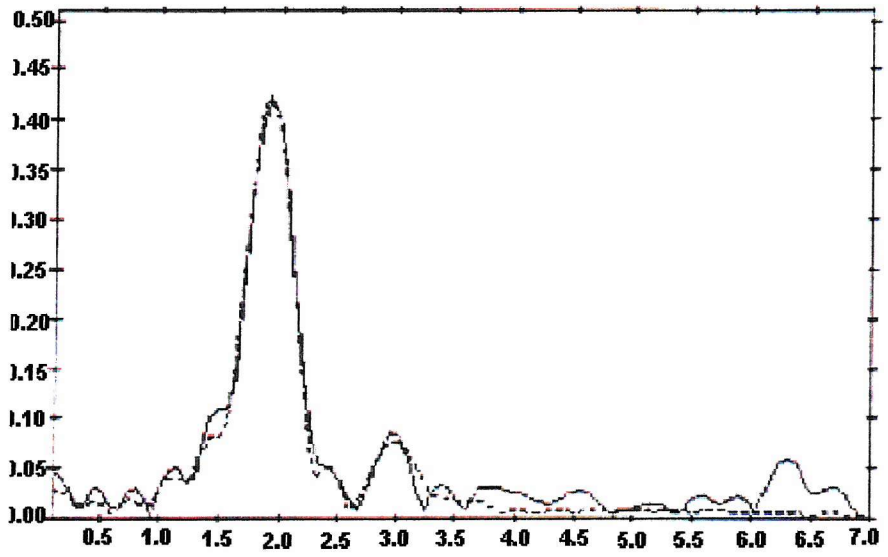

Figure 4.6 Ga k^3-weighted EXAFS data and Fourier transform of MCM-41(A)/ $Ga(CH_3)_3$ vapour; phase shift corrected for C.

(— Experimental, ----- Theory)

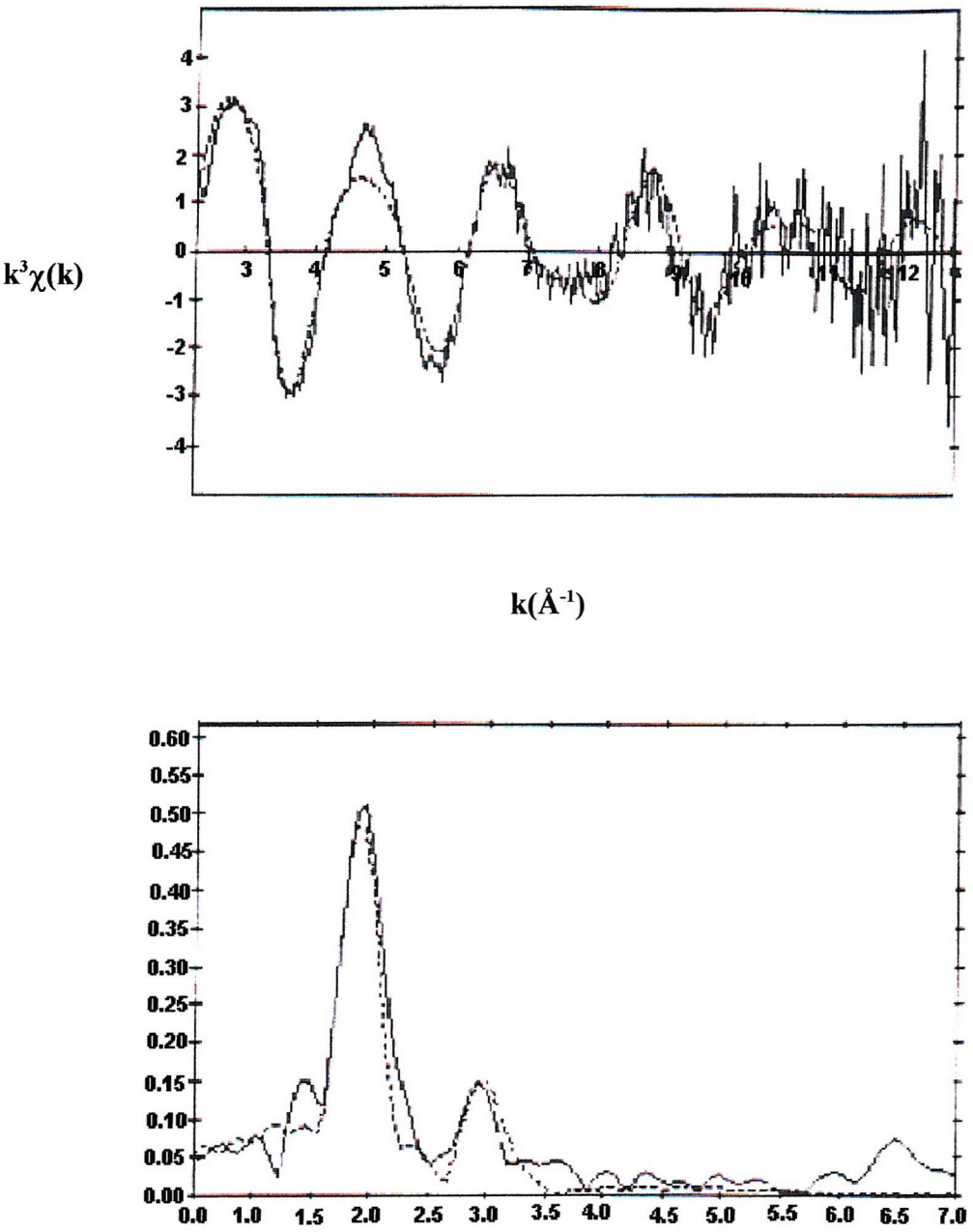

Figure 4.7 Ga k^3-weighted EXAFS data and Fourier transform of MCM-41(A)/ $Ga(CH_3)_3$ vapour/under vacuum; phase shift corrected for C. (— Experimental, ----- Theory)

MCM-41(A)/Ga(CH$_3$)$_3$ vapour/under vacuum

In this stage of the experiment, the EXAFS chamber was placed under vacuum (1.5 x10^{-3} atm) to remove excess trimethylgallium vapour. Figure 4.7 shows the EXAFS data and Fourier transform. The best fit for the data (table 4.5) was with four shells corresponding to model F. This consisted of a first shell of two carbon atoms at 1.920(5) Å and the second shell of two oxygen atoms at 1.828(2) Å. Placing the system under vacuum and removing excess trimethylgallium meant that a shell of 2 silicon atoms could be fitted at 3.308(4) Å with a fourth shell of gallium at 2.906(1) Å. The inclusion of a fourth shell was statistically significant and resulted in positive Debye-Waller factors and a reduction in the R-factor from 45.7% to 36.2%.

N[a]	R/Å	A/Å^{2}[b]
2C	1.920(5)	0.008(1)
2O	1.828(2)	0.012(2)
2Si	3.308(4)	0.031(3)
1Ga	2.906(1)	0.024(2)
R-factor = 36.2%; E_f = -7.50 eV		

[a]Coordination number; [b]Debye-Waller factor A = $2\sigma^2$, σ = mean square internuclear separation. Statistical errors derived in excurv92 given in parentheses.

Table 4.5 Ga K-edge EXAFS derived structural parameters for MCM-41(A)/Ga(CH$_3$)$_3$ vapour/under vacuum.

MCM-41(A)/Ga(CH$_3$)$_3$ vapour/vacuum/100°C

In the next stage of the experiment, the sample was heated to 100°C. The EXAFS data and Fourier transform for the experiment are presented in figure 4.8. Analysis of this data (table 4.6) was very similar to the previous experiment in as much as it, too, fit to model F with slight variations in bond lengths. The data fit to a first shell of two carbon atoms at 1.911(3) Å and a second shell of two oxygen atoms at 1.871(1) Å. A shell of two silicon atoms at 3.279(1) Å and a fourth shell of gallium at 2.909(1) Å completed the fit. The Debye-Waller factors were slightly higher than previously due to the increased temperature and a deterioration in the quality of the data.

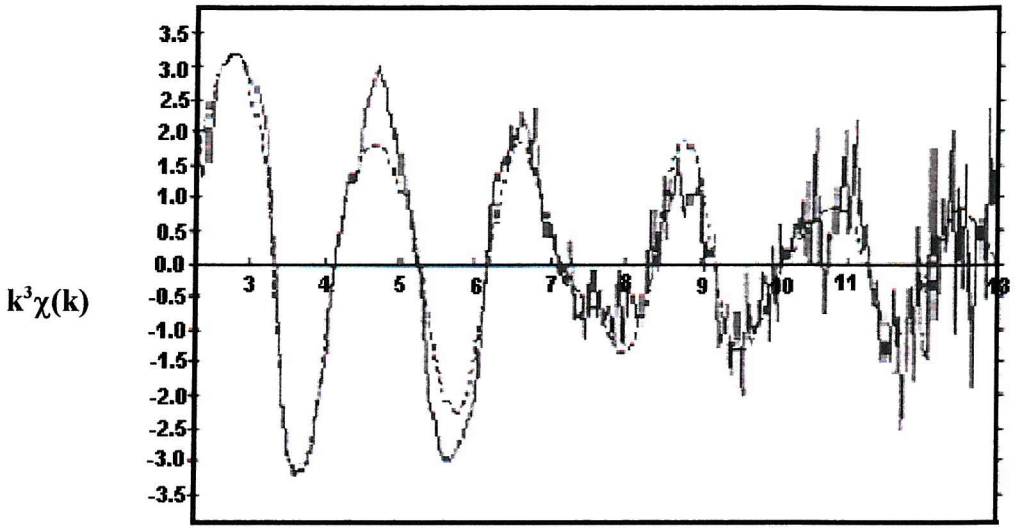

k(Å^{-1})

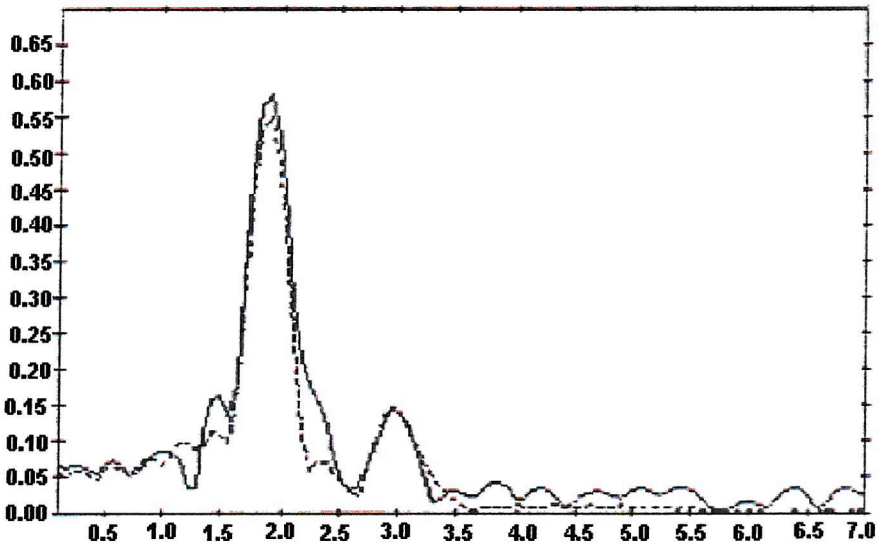

R(Å)

Figure 4.8 Ga k^3-weighted EXAFS data and Fourier transform of MCM-41(A)/ $Ga(CH_3)_3$ vapour/vacuum/100°C; phase shift corrected for C. (— Experimental, ----- Theory)

N[a]	R/Å	A/Å^{2b}
2C	1.911(3)	0.006(1)
2O	1.871(1)	0.037(2)
2Si	3.279(1)	0.038(2)
1Ga	2.909(1)	0.023(1)
R-factor = 30.6%; E_f = -7.99 eV		

[a]Coordination number; [b]Debye-Waller factor A = $2\sigma^2$, σ = mean square internuclear separation. Statistical errors derived in excurv92 given in parentheses.

Table 4.6 Ga K-edge EXAFS derived structural parameters for MCM-41(A)/Ga(CH$_3$)$_3$ vapour/100 °C.

MCM-41(A)/Ga(CH$_3$)$_3$/200°C

In the final stage of the experiment, the sample was heated to 200°C. The EXAFS data and Fourier transform are presented in figure 4.9. At 200°C, the data quality was poor but analysis of the data (table 4.7) gave a different gallium environment than the previous analyses. A best fit for the data was obtained for a first co-ordination sphere of two carbon atoms at 1.919(2) Å but the second shell contained only one oxygen atom at 1.772(2) Å. The third shell reflected this change by fitting to one silicon atom at 3.227(1) Å and a gallium species was still detected at 2.914(1) Å. This fit corresponded to model E suggesting that the increased temperature destabilised the structure preferring linkage to the surface via one silanol group rather than two and thereby retaining gallium's preferred three-coordinate state.

N[a]	R/Å	A/Å^{2b}
2C	1.919(2)	0.003(1)
1O	1.772(2)	0.042(2)
1Si	3.227(1)	0.039(2)
1Ga	2.914(1)	0.027(3)
R-factor = 28.2%; E_f = -3.85 eV		

[a]Coordination number; [b]Debye-Waller factor A = $2\sigma^2$, σ = mean square internuclear separation. Statistical errors derived in excurv92 given in parentheses.

Table 4.7 Ga K-edge EXAFS derived structural parameters for MCM-41(A)/Ga(CH$_3$)$_3$ vapour/200°C

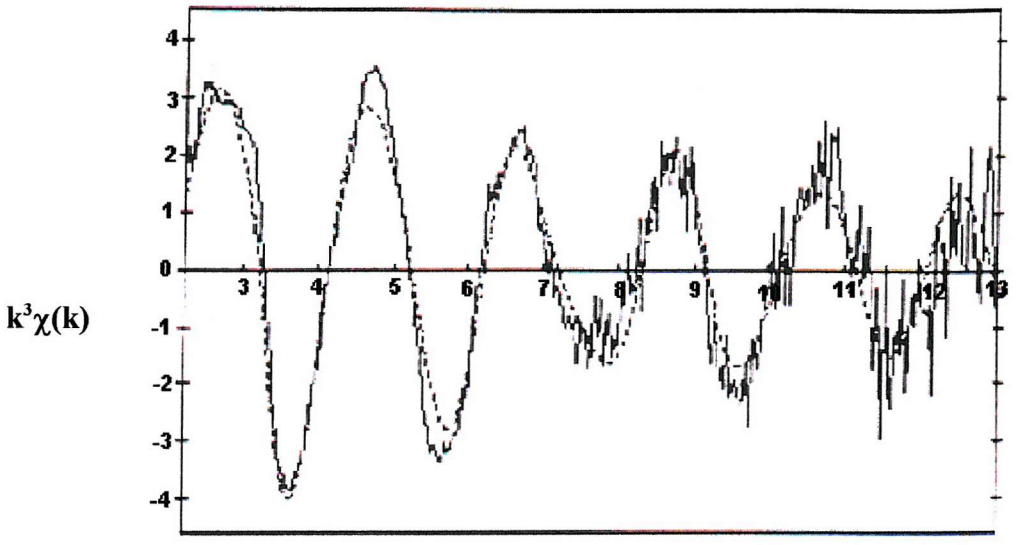

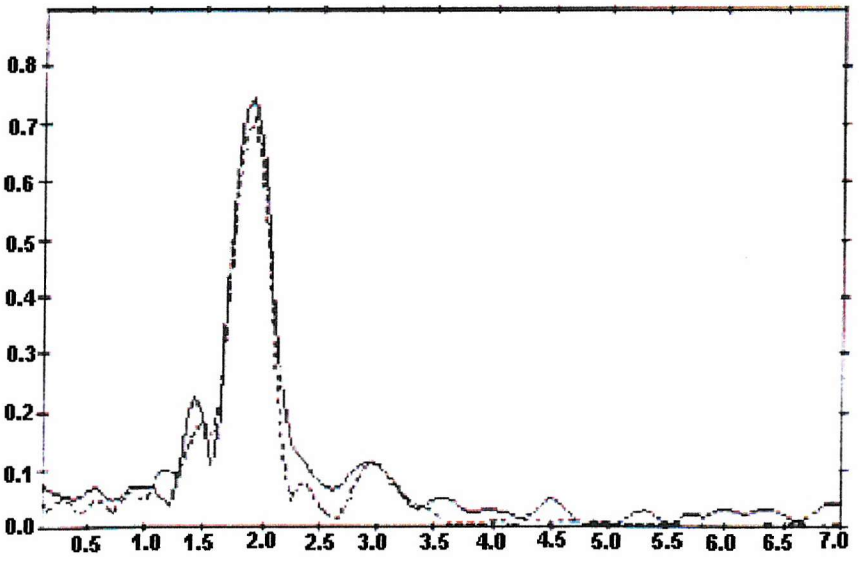

Figure 4.9 Ga k^3-weighted EXAFS data and Fourier transform of MCM-41(A)/ $Ga(CH_3)_3$ vapour/200°C; phase shift corrected for C.

(— Experimental, ----- Theory)

4.3 MCM-41(A) modified with $Zn(C_2H_5)_2$ – vapour phase reaction

The XAS experiments on this system were carried out on Station 7.1 at the Daresbury Laboratory. All manipulations took place in a glove box and sample preparation was identical to that for the gallium system. MCM-41(A) (0.20 g) was dehydrated under vacuum at 200°C for 2 h and stored under argon. The silica was loaded onto the EXAFS cell by slurrying with anhydrous pentane to form a suspension and pipetting onto the surface of the cell to form an even layer. Once the sample was securely attached to the cell, the cell was placed in the path of the beam and attached to the vacuum system and a heating implement (see figure 4.4). A sealed cell containing liquid diethylzinc was connected to the EXAFS cell and the system was systematically evacuated and flushed with an inert gas to remove any contaminants.

4.3.1 EXAFS Analysis of MCM-41(A) modified with $Zn(C_2H_5)_2$ – vapour phase reaction

As before, the cell containing the diethylzinc was heated with an air gun to vaporise the liquid. The process of introducing the vapour to the system was identical to that for the trimethylgallium, however, diethylzinc was found to be less inclined to vaporise, therefore introduction to the EXAFS cell took considerably longer than in previous experiments.

MCM-41(A)/$Zn(C_2H_5)_2$ – vapour

The reaction with diethylzinc was not as easy to achieve as with trimethylgallium. The data quality was poorer and harder to fit. The EXAFS data and Fourier transform for the system under vacuum are presented in figure 4.10. Analysis of the data (table 4.8) shows that a first co-ordination sphere of two separate shells of carbon and oxygen could not be fitted to this data. A best fit of four carbon atoms was possible at 1.94(1) Å. The presence of a longer Zn-C bond fitted at 3.25(8) Å suggests that an ethyl group remains attached to the zinc atom.

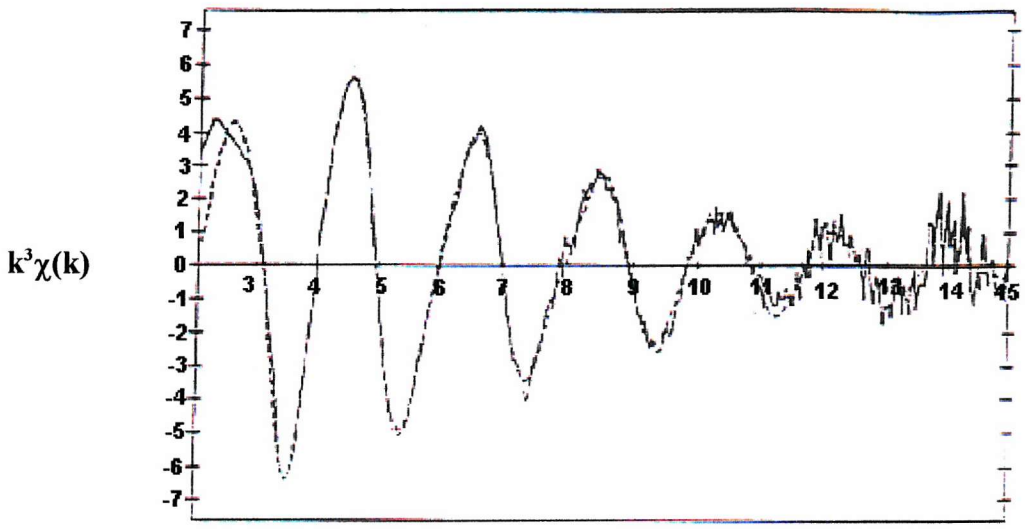

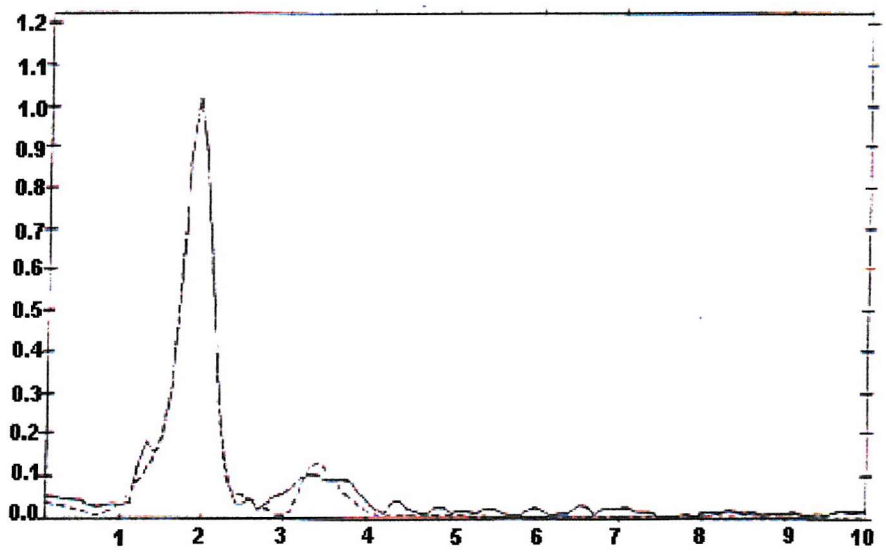

Figure 4.10 Zn k^3-weighted EXAFS data and Fourier transform of MCM-41(A)/ $Zn(C_2H_5)_2$ vapour/under vacuum; phase shift corrected for C. (— Experimental, ----- Theory)

N[a]	R/Å	A/Å^{2b}
4C	1.94(1)	0.012(1)
1C	3.25(8)	0.012(3)
2Si	3.56(9)	0.023(3)
R-factor = 15.5%; E_f = -5.31 eV		

[a]Coordination number; [b]Debye-Waller factor A = $2\sigma^2$, σ = mean square internuclear separation. Statistical errors derived in excurv92 given in parentheses.

Table 4.8 Zn K-edge EXAFS derived structural parameters for MCM-41(A)/Zn(C_2H_5)$_2$ vapour/under vacuum

This shell was statistically significant at a 95% probability level and allowed a reduction of 15% in the R-factor. Thus the remaining three atoms of the first co-ordination sphere are assigned to oxygen. However, only two silicon atoms could be further fitted to this data at 3.56(9) Å. It is possible that two types of interaction are occurring and the two possible species are presented in figure 4.11. Model A suggests an ethylzinc species with three silanol attachments to the silica surface. Model B suggests an ethylzinc species with two silanol attachments and interaction from a surface siloxane group.

MCM-41(A)/Zn(C_2H_5)$_2$ – vapour/vacuum/100°C.

On heating the sample up to 100°C and placing the system under vacuum (1.5 x10^{-3} atm), the data becomes more manageable. The EXAFS data and Fourier transform are presented in figure 4.12. Analysis of the data, (table 4.9) shows that it is now possible to separate the oxygen and carbon atoms of the first co-ordination sphere and fit the data to two shells of three oxygen atoms and one carbon atom at 1.937(2) Å and 2.067(7) Å, respectively. A third statistically significant shell of one carbon atom at 3.363(9) Å suggests that an ethyl group remains attached to the zinc at this increased temperature. Furthermore, it now becomes possible to fit a shell of three silicon atoms at 3.593(9) Å. This allows model B to be discarded and to assume that the ethylzinc co-ordinates with the silica via three surface silanol groups.

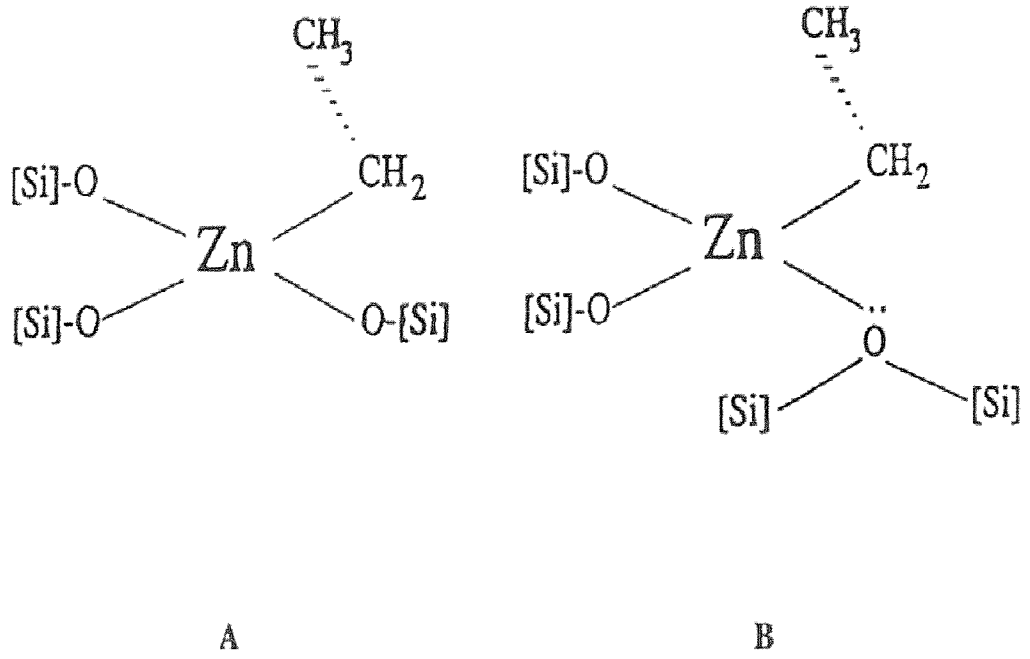

Figure 4.11 Diethylzinc interactions with silica surface

N[a]	R/Å	A/Å^{2b}
3O	1.937(2)	0.007(3)
1C	2.067(7)	0.005(1)
1C	3.363(9)	0.004(2)
2Si	3.593(9)	0.038(3)
R-factor = 15.8%; E_f = -5.31 eV		

[a]Coordination number; [b]Debye-Waller factor A = $2\sigma^2$, σ = mean square internuclear separation. Statistical errors derived in excurv92 given in parentheses.

Table 4.9 Zn K-edge EXAFS derived structural parameters for MCM-41(A)/Zn(C_2H_5)$_2$ vapour/100°C.

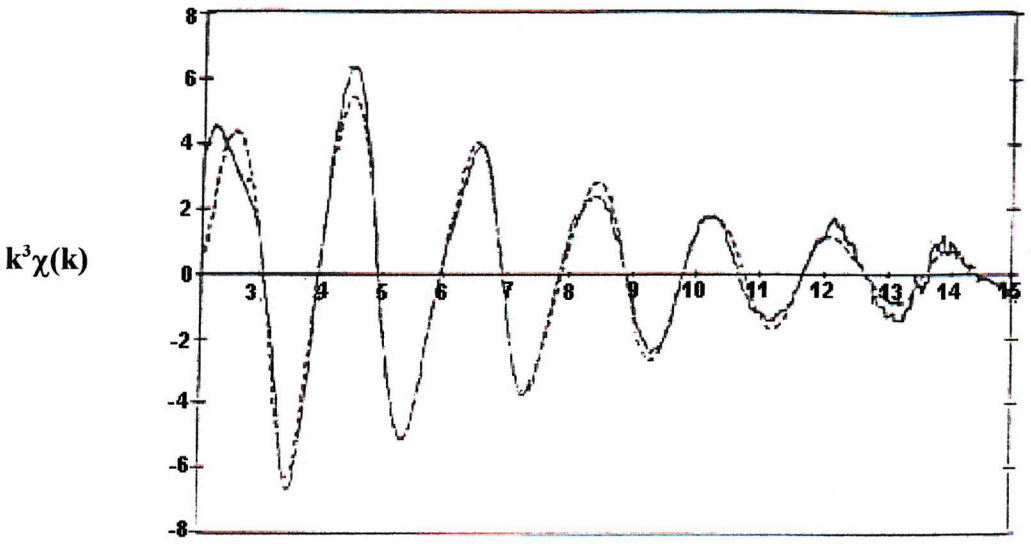

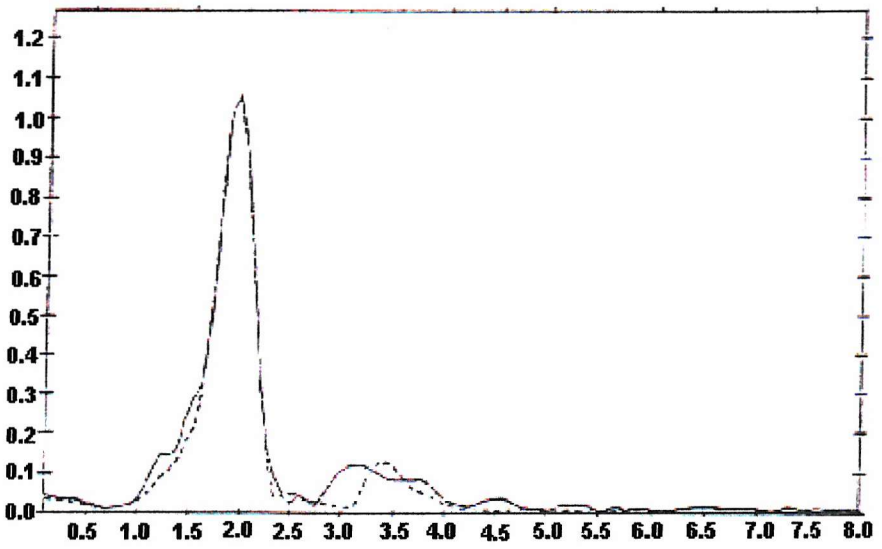

Figure 4.12 Zn k^3-weighted EXAFS data and Fourier transform of MCM-41(A)/ $Zn(C_2H_5)_2$ vapour/vacuum/100°C; phase shift corrected for C

(— Experimental, ----- Theory)

4.4 MCM-41(B), MESLC and KMES modified with $Ga(CH_3)_3$ and $Zn(C_2H_5)_2$ - vapour phase reaction

The XAS experiments on MCM-41(B), MESLC and KMES mesoporous silicas were carried out on Station 9.2 [for $Ga(CH_3)_3$] and on Station 7.1 [for $Zn(C_2H_5)_2$] at the Daresbury Laboratory. In each case samples (0.2-0.3 g) were dehydrated under vacuum at 200°C for 2 h and stored in an inert atmosphere. The samples were loaded onto the EXAFS cell as described above by applying a suspension of the samples in anhydrous pentane to the surface of the cell forming even layers.

4.4.1 EXAFS analysis of MCM-41(B), MESLC and KMES modified with $Ga(CH_3)_3$ - vapour phase reaction

For each of the three types of silica, samples were exposed to $Ga(CH_3)_3$ vapour for 1 h, the EXAFS cell was heated under vacuum (1.5×10^{-3} atm) to 200°C and held at this temperature for the duration of the experiments. The EXAFS derived structural parameters for the samples at 200°C are presented in table 4.10. The EXAFS spectrum and Fourier transform of each of the samples were very similar to those of MCM-41(A) and are not presented.

The EXAFS data were initially fitted to the models suggested in section 4.2.1 (see figure 4.5) and applying the same logic, the number of possible models was reduced to two: the loss of a methyl group and interaction with the silica surface via either one or two surface silanol groups (models E and F, respectively). The EXAFS data for the MCM-41(B)/$Ga(CH_3)_3$ system was best fitted to three shells of two carbon atoms at 1.908(1) Å, one oxygen atom at 1.801(2) Å and one silicon atom at 3.23(3) Å suggesting interaction with the silica surface via one silanol group with the gallium atom remaining in a tri-coordinate state. The Debye-Waller factors were within acceptable parameters for this fit and an R-factor of 44.6% was achieved.

	N[a]	R/Å	A/Å^{2b}
MCM41(B)/Ga(CH$_3$)$_3$ *R-factor =44.6%*	2C 1O 1Si	1.908(1) 1.801(2) 3.23(3)	0.01(2) 0.005(3) 0.032(1)
MESLC/Ga(CH$_3$)$_3$ *R-factor =16.6%*	2C 2O 2Si 1Ga	1.912(1) 1.763(3) 3.25(9) 2.91(1)	0.003(1) 0.011(3) 0.026(2) 0.031(3)
KMES/Ga(CH$_3$)$_3$ *R-factor =29.7%*	2C 1O 1Si	1.916(2) 1.81(1) 3.213(1)	0.011(1) 0.007(2) 0.028(1)

[a]Coordination number; [b]Debye-Waller factor A = $2\sigma^2$, σ = mean square internuclear separation. Statistical errors derived in excurv92 given in parentheses.

Table 4.10 Ga K-edge EXAFS derived structural parameters for MCM-41(B), MESLC and KMES modified with Ga(CH$_3$)$_3$ vapour/200°C

A fourth shell of one gallium atom at 2.89(3) Å was also fitted to the data but this shell resulted in low Debye-Waller factors and was not statistically significant. For the MESLC/Ga(CH$_3$)$_3$ system, a best fit was obtained with four shells of two carbon atoms at 1.912(1) Å, two oxygen atoms at 1.763(3) Å, two silicon atoms at 3.25(9) Å and a fourth shell of one gallium atom at 2.91(1) Å. In this instance, the gallium shell was statistically significant at the 95% probability level and resulted in a reduction of 16.5% in the R-factor to 16.6%. A best fit was obtained for the KMES/Ga(CH$_3$)$_3$ system with three shells of two carbon atoms at 1.916(2) Å, one oxygen atom at 1.81(1) Å and a silicon atom at 3.213(1) Å. Although a fourth shell of one gallium atom could be fitted to this data indicating the presence of neighbouring gallium species, the shell resulted in negative Debye-Waller factors and had little impact on the R-factor.

The results of these experiments for MCM-41(B) and KMES are comparable to those obtained for the MCM-41(A)/$Ga(CH_3)_3$ system at 200°C suggesting that following the loss of a methyl group, a dimethylgallium species interacts with the surface of the silica via one silanol group with some interaction with neighbouring gallium species (model E). However, in the case of the MESLC/$Ga(CH_3)_3$ system, although the atomic distances are comparable, the dimethylgallium species is anchored to the surface of the silica via two silanol groups resulting in a four-coordinate gallium centre (model F). At 100°C for the MCM-41(A)/$Ga(CH_3)_3$ system a best fit was obtained corresponding to that of model F but increasing the temperature to 200°C resulted in a best fit corresponding to model E. It is possible that the increased crystallinity of the MESLC structure provides greater stability for the four-coordinate model to exist.

4.4.2 EXAFS analysis of MCM-41(B), MESLC and KMES modified with $Zn(C_2H_5)_2$ - vapour phase reaction

Samples of MCM-41(B), MESLC and KMES were exposed to $Zn(C_2H_5)_2$ vapour for 1 h and then the cell was heated under vacuum (1.5 $x10^{-3}$ atm) to 100°C and held at this temperature for the duration of the experiments. The EXAFS derived structural parameters for the samples at 100°C are presented in table 4.11; the EXAFS spectra and Fourier transform are not presented.

The data was initially modelled to a diethylzinc species to eliminate the possibility that no reaction had taken place. The data was then modelled to the two forms of interaction suggested earlier (see figure 4.11), *i.e.*, the loss of an ethyl group and the interaction of ethylzinc species with either three silanol attachments to the silica surface or two silanol attachments and interaction from a surface siloxane group. At 100°C it was possible to resolve a first co-ordination sphere of carbon and oxygen atoms. For the EXAFS data of the MCM-41(B)/$Zn(C_2H_5)_2$ system, a best fit was obtained with only two shells of three oxygen atoms at 1.933(1) Å and one carbon atom at 2.078 Å. An attempt was made to fit a third shell

of silicon atoms but this resulted in negative Debye-Waller factors and was found to be not statistically significant.

	N[a]	R/Å	A/Å^{2b}
MCM41(B)/Zn(C_2H_5)$_2$ *R-factor = 37.3%*	3O 1C	1.933(1) 2.078(3)	0.005(1) 0.011(1)
MESLC/Zn(C_2H_5)$_2$ *R-factor =21.6%*	3O 1C 3Si 1C	1.936(1) 2.06(3) 3.59(2) 3.359(1)	0.007(3) 0.009(1) 0.015(3) 0.022(1)
KMES/Zn(C_2H_5)$_2$ *R-factor = 31.2%*	3O 1C 2Si	1.93(4) 2.058(1) 3.58(9)	0.009(1) 0.016(2) 0.031(1)

[a]Coordination number; [b]Debye-Waller factor A = $2\sigma^2$, σ = mean square internuclear separation. Statistical errors derived in excurv92 given in parentheses.

Table 4.11 Zn K-edge EXAFS derived structural parameters for MCM-41(B), MESLC and KMES modified with Zn(C_2H_5)$_2$ vapour/100°C.

For the MESLC/Zn(C_2H_5)$_2$ system, it was possible to model the data to four shells. This consisted of a first co-ordination sphere of three oxygen atoms at 1.936(1) Å and one carbon atom at 2.06(2) Å. A third shell of three silicon atoms at 3.59(2) Å and a fourth shell of one carbon atom corresponding to the second carbon of the ethyl group. This shell was statistically significant at the 95% probability level and resulted in a reduction of the R-factor by 10.6% to 21.6%. The EXAFS data of the KMES/Zn(C_2H_5)$_2$ system was best fitted to three shells of three oxygen atoms at 1.93(4) Å, one carbon atom at 2.058(1) Å and two silicon atoms at 3.58(9) Å. In each of the three systems an attempt was made to model a shell of zinc atoms to the data but these shells were not statistically significant and had little impact on the R-factors.

For each of the three systems, the results were comparable to the results obtained for the MCM-41(A)/$Zn(C_2H_5)_2$ system at 100°C corresponding to the loss of an ethyl group and attachment to the surface of the silica via two or three silanol groups. For MCM-41(B) silica it was not possible to resolve the silicon atoms but for MESLC silica three silicon atoms in the same environment were resolved corresponding to interaction with the silica surface via three silanol groups, and for KMES silica it was only possible to fit two silicon atoms of the same environment to the data suggesting interaction with the silica surface via two silanol groups with the siloxane group interaction unresolved.

4.5 Discussion

The modification of mesoporous silicas with trimethylgallium was relatively straightforward. The results were very similar, with the trimethylgallium reacting to form tri-coordinate species with the loss of one methyl group and attachment via one silanol group at a temperature of 200°C for MCM-41(A), MCM-41(B) and KMES silicas with evidence of a four-coordinate species (dimethylgallium interacting with the silica via two silanol groups) for MESLC at this temperature and for MCM-41(A) at 100°C. Interaction with other gallium species was detected by Ga-Ga distances of between 2.52 - 3.0 Å for MCM41(A) and MESLC which is consistent with literature values of Ga-Ga distances.[9,10] These Ga-Ga bond lengths fall within metal bonding ranges which suggests that a direct metal-metal bond is formed rather than a non-bonding interaction caused by proximity. This places the gallium centre in a stable four-coordinate environment for MCM-41(A) and a five-coordinate environment for MESLC.

Much of the study on the trimethylgallium species has concentrated on its thermal decomposition. Trimethylgallium is frequently used as a starting material to form semiconductors such as GaN and to grow thin films of alloy semiconductors such as GaAs both of which are formed using metal organic chemical vapour deposition techniques (MOCVD). One of the earliest experiments on thermal decomposition was by Jacko and Price[12] who studied the pyrolysis of trimethylgallium in a toluene carrier flow. They proposed

a stepwise mechanism where the first and second methyl groups were released as radicals with the remaining methylgallium forming a polymer on the reactor surface. Subsequent studies by Yoshida *et al*[13] and Denbaars *et al*[14] have shown that trimethylgallium decomposes in H_2 and N_2 atmospheres to give off methane as a major product with no evidence of methylgallium polymers. This seeming contradiction was explored by Masataka Hoshino[15] whose research showed that pressure affected the decomposition. At lower pressures (<3 x 10^{-3} atm) decomposition took place heterogeneously but at pressures higher than this, decomposition occurred homogeneously in the gas phase. However, all these researchers worked at temperatures higher than those used in this research. Low temperature studies (<300°C) done by Lee *et al*[16] and Mazzarese *et al*[17] found no differences between H_2 and N_2 atmospheres and confirmed that methane production occurs with decomposition in the gas phase. This study further states that the final step of the reaction occurs on the substrate surface. In all cases, it is clear that the decomposition of trimethylgallium is affected by carrier flow, pressure and the catalytic effect of the surface substrate.[18,19]

The relatively low pressures used in this research suggests a heterogeneous decomposition of trimethylgallium which in the first experiment (4.1) is a distinct possibility, but introducing the vapour directly to the silica without using a carrier flow eliminates the carrier flow effects and suggests a homogenous decomposition in the gas phase. Trimethylgallium does not decompose cleanly and adsorbed trimethylgallium most likely eliminates a methyl group which reacts with the hydrogen ion from the silanol species to form methane. This leaves a film of dimethylgallium which would account for the prominent Ga-Ga interactions noted in the EXAFS analyses. Literature suggests that the trimethylgallium should decompose via loss of two methyl groups but in this work this was not seen to be the case. It is possible that at temperatures higher than 200°C, further decomposition to a mono-methylgallium species would occur.

The reaction of diethylzinc with the mesoporous silicas was achieved in an identical manner as with the equivalent gallium experiments, however, vaporising the liquid diethylzinc within the cell proved more difficult. The experiment was repeated with different mesoporous silicas and the results were found to be similar. In all the EXAFS analyses, the Zn-C bond length was between 1.949 - 2.08 Å which is consistent with literature values for the zinc to

carbon distance in diethylzinc species.[20,21] The second carbon atom detected in some of these experiments was assigned to the second carbon of the ethyl group, working on the assumption that due to its steric position and proximity to the zinc atom, it would be detected in the EXAFS experiment. In recent developments of semiconductors and lasers, diethylzinc has become of increasing importance[22,23] and this has lead to increased interest in the reaction of species such as diethylzinc on the surface of thin films such as GaAs(110) and ZnSe.[24,25] From these and other studies, it has been deduced that the diethylzinc dimer adsorbs onto clean surfaces and upon the application of heat, it undergoes dissociation by elimination of an ethyl species as ethylene. In this work, on introduction to the mesoporous silica, the diethylzinc does dissociate and elimination of an ethyl group does occur, but the other ethyl group remains attached to the zinc atom. There is, however, no evidence of Zn-Zn interactions to suggest a film being formed. Instead, the zinc forms strong bonds with the surface silanol groups placing the zinc atom in a stable four-coordinate environment. It is possible that at temperatures higher than those used in this study, the ethylzinc species may further decompose to leave zinc metal ions on the surface of the silica.

4.6 Conclusions

MCM-41(A) was alkylated in a direct reaction by trimethylgallium and indirectly via a vapour phase technique by trimethylgallium and diethylzinc. The vapour phase reactions were deemed more successful and were used for subsequent reactions with MCM-41(B), MESLC and KMES mesoporous silicas. The results were similar for all four types of silica and from the EXAFS experiments it can be concluded that trimethylgallium reacts with the loss of one methyl group to attach to the silica surface via one silanol group (at 200°C) for MCM-41(A), MCM-41(B) and KMES, and via two silanol groups for MCM-41(A) and MESLC at 100°C and 200°C, respectively forming a film on the surface by strong interaction with neighbouring gallium species. Diethylzinc reacts at a slower rate with the loss of one ethyl group and links to the silica surface via three silanol groups for MCM-41(A), MCM-41(B) and KMES, and via two silanol groups for MESLC with no interactions with neighbouring zinc atoms.

4.7 References

1. Takai, K., Oshima, K., Nozaki, H., *Tetrahedron Lett.*, 1980, 1657.
2. Boireau, G., Abenheim, D., Henry-Bausch, E., *Tetrahedron Lett.*, 1979, **35**, 1457.
3. Pasynkiewicz, S., *Polyhedron*, 1990, **9**, 429.
4. Mason, M. R., Smith, J. M., Bott, S. G., Barron, A. R., *J. Am. Chem. Soc.*, 1993, **115**, 4971.
5. Harlan, C. J., Mason, M. R., Barron, A. R., *Organometallics*, 1994, **13**, 2957.
6. Schumann, H., Frick, M., Heymer, B., Girgsdies, F., *J. Organomet. Chem.*, 1996, **512**, 117.
7. Schauer, S. J., Lake, C. H., Watkins, L. L., Krannich, L. K., *Organometallics*, 1996, **15**, 5641.
8. Kim, S. H., Kim, H. S., Hwang, J. S., Choi, J. G., Chong, P. J., *Chem. Mater.*, 1994, **6**, 278.
9. Dillingham, M. D. B., Burns, J. A., Byer-Hill, J., Gripper, K. D., Pennington, W. T., Robinson, G. H., *Inorg. Chim. Acta*, 1994, **216**, 267.
10. Uhl, W., Layh, M., Hildenbrand, T., *J. Organomet. Chem.*, 1989, **364**, 289.
11. Francis, J. T., Benson, S. W., Tsotsis, T.T., *J. Phys. Chem.*, 1991, **95**, 4583.
12. Jacko, M. G., Price, S. J. W., *Can. J. Chem.*, 1963, **41**, 1560.
13. Yoshida, M., Watanabe, H., Uesuge, F., *J. Electrochem. Soc.*, 1985, **132**, 677.
14. Denbaars, S. P., Maa, B. Y., Dapkus, D. P., Danner, A. D., Lee, H. C., *J. Cryst. Growth*, 1986, **77**, 188.
15. Hoshino, M., *J. Appl. Phys.*, 1990, **68**, 2538.
16. Lee, P. W., Omstead, T. R., Makenna, D. R., Jensen, K. F., *J. Cryst. Growth*, 1987, **85**, 165.
17. Mazzarese, D., Tripathe, A., Conner, W. C., Jones, K. A., Calderon, L., Eckart, D. W., *J. Electron. Mater.*, 1989, **18**, 369.
18. Mazzarese, D., Tripathe, A., Conner, W. C., *J. Electron. Mater.*, 1989, **18**, 45.
19. Lee, F., Gow, T. R., Masel, R. I., *J. Electrochem. Soc.*, 1989, **136**, 2640.
20. Malik, K. A., O'Brien, P., Motevalli, M., Jones, A. C., *Inorg. Chem.*, 1997, **36**, 5076.
21. Fabicon, R. M., Parvez, M., Richey, H. G., *J. Am. Chem. Soc.*, 1991, **113**, 1412.

22. Kisker, D. W., *J. Cryst. Growth*, 1989, **98**, 127.

23. Tsang, W. T., *J. Cryst. Growth*, 1992, **120**, 1.

24. Lasky, P. J., Lu, P. H., Luo, Y., Slater, D. A., Osgood, R. M., *Surf. Sci.*, 1996, **364**, 312.

25. Rueter, M. A., Vohs, J. M., *Surf. Sci.*, 1994, **301**, 165.

CHAPTER FIVE

Organopalladium-Modified Mesoporous Silicas

5.0 Introduction

This chapter describes post-synthetic modification of mesoporous silicas with organopalladium complexes. As the interest in immobilizing catalysts on solid supports increases,[1-3] so too does the method by which the support takes place. Silica is one of the most common supports because its surface properties have been well characterized,[4] however, direct reaction between silica and catalyst complexes can be difficult and inefficient. There are two main approaches to supporting metal complexes on silica supports. The first is a direct reaction of the metal centre with the silanol groups of the support and the second is an indirect reaction involving functionalization of the support with phosphines or amines prior to the introduction of the metal species. In this second approach, the interaction is then between the metal centre and the functionalising species. Both methods involve post-synthesis modification of the mesoporous or functionalized mesoporous silicas via vapour deposition methods or via a solution interaction of the organopalladium species with the silica supports. This chapter looks at the modification of MCM-41(A), MESLC and KMES with Pd(allyl)cp and studies the direct interaction of Pd(allyl)cp and $Pd(CH_3CN)_2(NO_2)Cl$ with MCM-41(A), and the indirect interaction of tetrakis(triphenylphosphine)palladium with phosphine-functionalized MCM-41(A).

The modified mesoporous silicas were difficult to analyse due to the moisture sensitivity of the supports and the low loading of the organopalladium complexes. Therefore, several techniques were utilized; Atomic Absorption Spectroscopy (AAS) was used to obtain the loading measurements, TEM was used to verify the mesoporous structure of the silicas post-reaction with the organopalladium species and EXAFS was used as the main investigative tool to determine the environment around the palladium centres.

Palladium(II) catalysed oxidations of unsaturated hydrocarbons to form oxygenates such as epoxides, α,β-unsaturated acids and esters are of great importance in organic syntheses and homogeneous catalysis[5,6] and many examples exist in the liquid phase.[7,8] Palladium is a commonly used transition metal for organic catalytic reactions due to its versatility in that it has the ability to coordinate to a variety of organic substrates and can be used in a wide range of organometallic reactions. Examples of well-defined organopalladium species supported on

inorganic silica supports are, however, relatively few. Palladium-containing titanium silicates[9] which catalyse the hydroxylation of benzene and hexane by hydrogen peroxide under mild conditions to give phenols and hexanols has been reported as has the reaction of $Pd(\eta^3\text{-}C_3H_5)_2$ with silica, leading to the species $[Si]\text{-}O\text{-}Pd(\eta^3\text{-}C_3H_5)$.[10] Strong spectroscopic evidence supporting this species was, however, not reported. There are numerous active palladium catalysts and the pores and cavities of the mesoporous materials are wide enough to accomodate them. If it is proved to be possible to cleanly attach a palladium catalyst to a mesoporous material, a new hybrid catalyst would be formed with the potential for oxidation catalysis.

5.1 Modification of mesoporous silicas with Pd(allyl)cp

Pd(allyl)cp is a volatile species which sublimes at 25°C, 2 mmHg and is therefore suitable for vapour deposition methods. It is a relatively small, discrete molecule which can easily enter the pores of the mesoporous silicas. Upon reaction, the labile allyl ligand is released and can be detected.

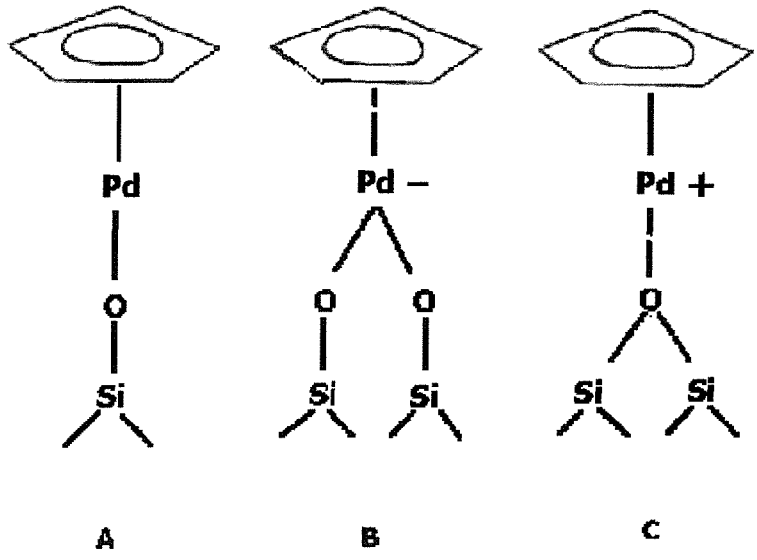

Figure 5.1 Models of Pd-cp interactions with silica surfaces.

5.1.1 Modification of MCM-41(A), MESLC and KMES with Pd(allyl)cp

The Pd(allyl)cp complex was made according to the method of Tatsuno, Yoshida and Seiotsuku[11] from $[Pd(allyl)Cl]_2$ and sodium cyclopentadienyl, resulting in red needle-like crystals of Pd(allyl)cp. The purity of the Pd(allyl)cp complex was verified by ^{1}H and ^{13}C solution NMR.

Preparation of mesoporous silica/Pd(allyl)cp

The mesoporous silica was dehydrated to 500°C prior to the introduction of the organopalladium species. Manipulation of both the silica and Pd(allyl)cp took place in a glove box. The silica was placed in a large ceramic boat and the Pd(allyl)cp was loaded into a smaller ceramic boat. Both these boats were placed in a large tube fitted with a Young's tap. The tube was placed under vacuum and the end containing the Pd(allyl)cp was heated to approximately 30°C using an air gun. The Pd(allyl)cp sublimed onto the silica; visibly seen as a change in colour from white to pink/red to yellow. The tube was left under vacuum for 3-4 h until all the Pd(allyl)cp had sublimed. This method was used for depositing Pd(allyl)cp on each of the three types of mesoporous silicas, MCM-41(A), MESLC and KMES.

EXAFS analysis

Palladium K-edge X-ray absorption spectra were recorded for the Pd(allyl)cp complex and for MCM-41(A), MESLC and KMES modified with Pd(allyl)cp. Figure 5.2 shows the EXAFS data and Fourier transform of Pd(allyl)cp and table 5.1 lists the corresponding EXAFS derived parameters. The Fourier transform shows two peaks corresponding to two shells of carbon atoms. The first shell is of three carbon atoms at 2.127(5) Å corresponding to the allyl group and the second shell is of five carbon atoms at 2.247(3) Å which is due to the cyclopentadienyl ligand. The inter-atomic distances derived from the EXAFS data are comparable to those in literature from single crystal X-ray diffraction data which give distances of 2.06 Å for the allyl group and 2.25 Å for the cyclopentadienyl ligand.[12]

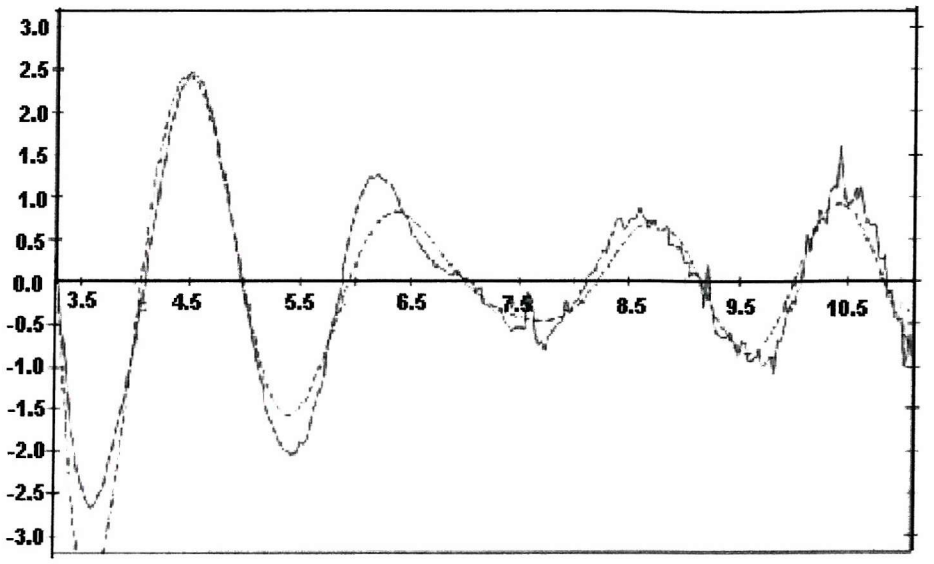

$k^3\chi(k)$

$k(Å^{-1})$

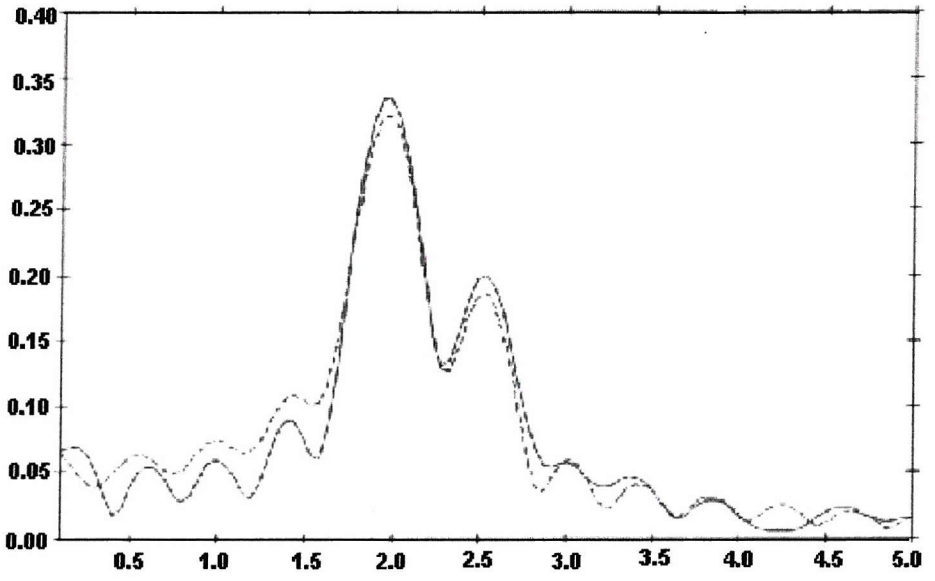

R(Å)

Figure 5.2 Pd K-edge k^3-weighted EXAFS data and Fourier transform of Pd(allyl)cp, phase shift corrected for C. (— Experimental, ----- Theory)

N[a]	R/Å	A/Å^{2b}
3C	2.127(5)	0.008(3)
5C	2.247(3)	0.0162(2)
R-factor = 27.7%; E_f = -2.31 eV		

[a]Coordination number; [b]Debye-Waller factor A = $2\sigma^2$, σ = mean square internuclear separation. Statistical errors derived in Excurve92 given in parentheses.

Table 5.1 Pd K-edge EXAFS derived structural parameters for Pd(allyl)cp

The EXAFS and Fourier transform spectra of the MCM-41(A)/Pd(allyl)cp system are presented in figure 5.3. In attempting to fit this data to the system several models of the interaction of the Pd-cp units with silica surfaces were considered (figure 5.1). Model A assumes the loss of the labile allyl group and the interaction of the Pd-cp unit with a surface silanol group. Model B assumes the loss of the allyl group followed by the interaction of the Pd-cp unit with two closely spaced surface silanol species resulting in a negative charge on the palladium atom. Model C assumes interaction of the Pd-cp unit with framework oxygen species resulting in a positive charge on the palladium atom. The EXAFS data for the system was fitted in turn to each of the three models. In each fit, a first shell corresponding to the five carbon atoms of the cp unit was possible but a second shell of one oxygen atom resulted in very high R-factors (>60%) with very low Debye-Waller factors. This eliminated models A and C. The best fit was obtained by fitting the data to model B with a first coordination sphere of five carbon atoms at 2.271(3) Å and two oxygen atoms at 2.419(4) Å. The validity of this fit was supported by a third shell of two silicon atoms at 3.125(5) Å. This shell was statistically significant at a 95% probability level and was further validated by a reduction in the R-factor from 54% to 28.5% and Debye-Waller factors within acceptable parameters. Figure 5.4 shows the EXAFS and Fourier transform spectra of the KMES/Pd(allyl)cp system measured at room temperature. The data was fitted to models A-C and a best fit was obtained for a shell of five carbon atoms at 2.126(1) Å and a second shell of two oxygen atoms at 2.454(3) Å again corresponding to model B as a second shell containing one oxygen atom was not statistically significant. It was also possible to fit a statistically significant third shell of two silicon atoms at 3.31(2) Å which resulted in the reduction of the R-factor by 9% to 32.3%. The reaction of MESLC with Pd(allyl)cp resulted in EXAFS and Fourier transform spectra as seen in figure 5.5. On fitting the models to the data from this system it was found that in this case a second shell of two oxygen atoms was not possible, resulting in negative

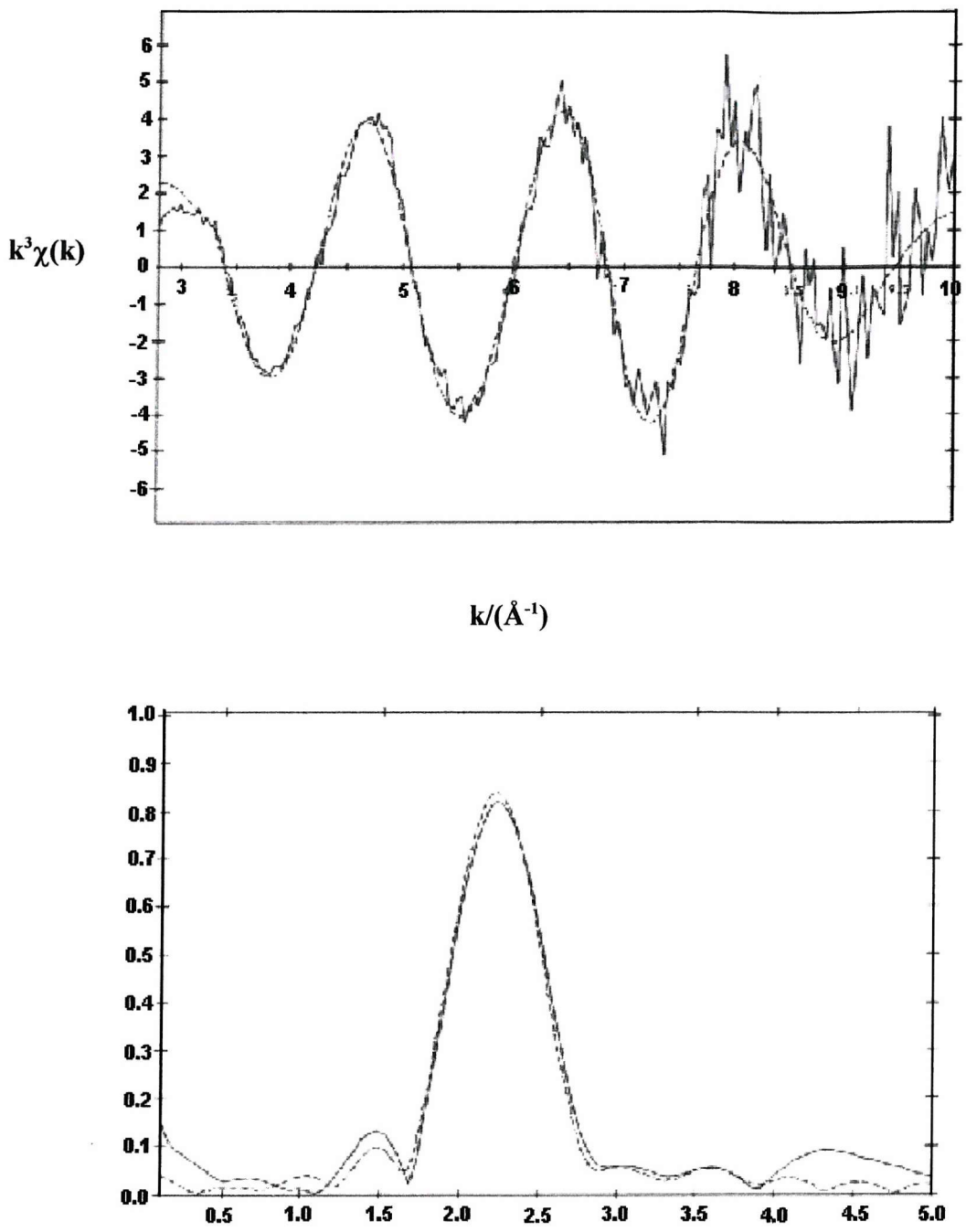

Figure 5.3 Pd K-edge k^3-weighted EXAFS data and Fourier transform of MCM-41(A)/Pd(allyl)cp, phase shift corrected for C.

(— Experimental, ----- Theory)

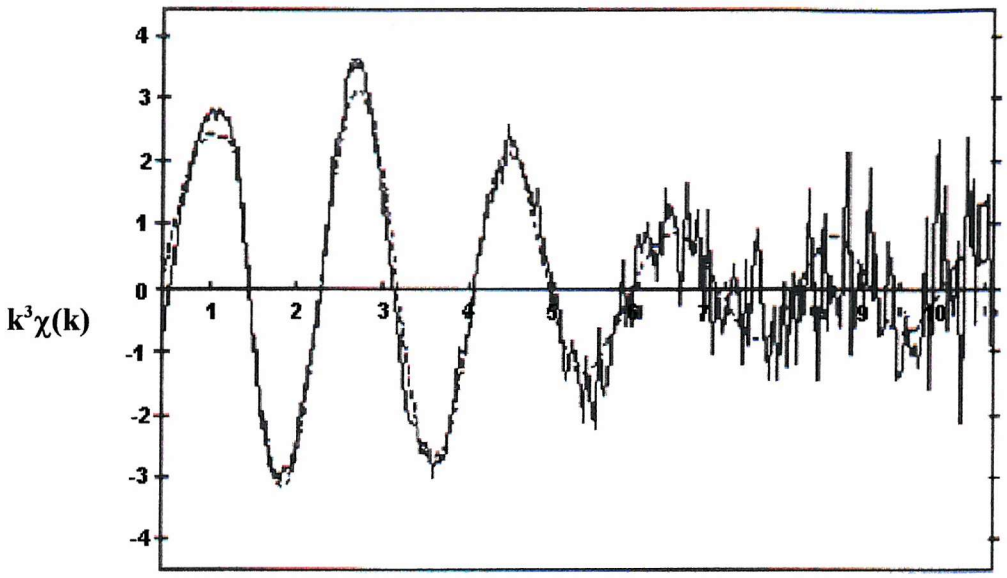

k/(Å^{-1})

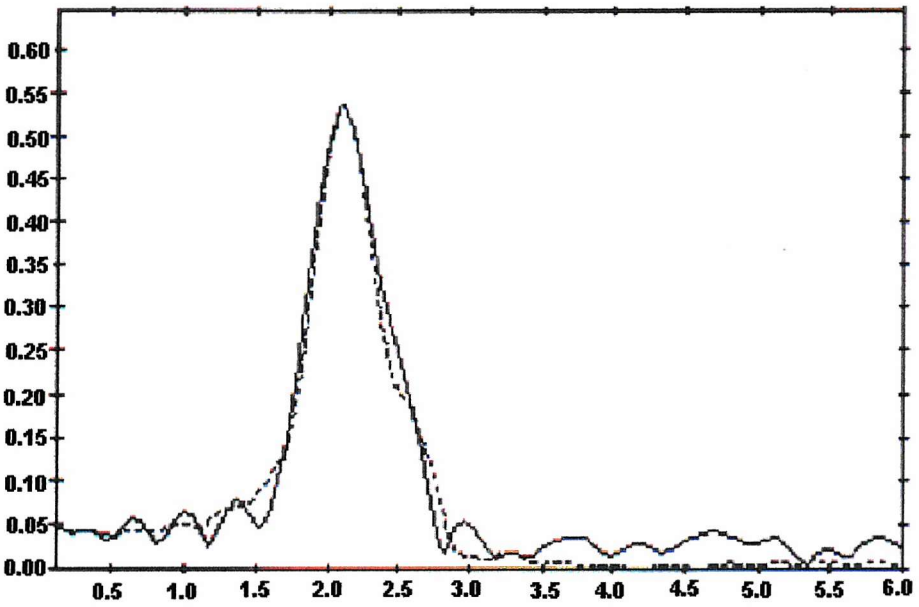

R/Å

Figure 5.4 Pd K-edge k^3-weighted EXAFS data and Fourier transform of KMES/Pd(allyl)cp, phase shift corrected for C.

(— Experimental, ----- Theory)

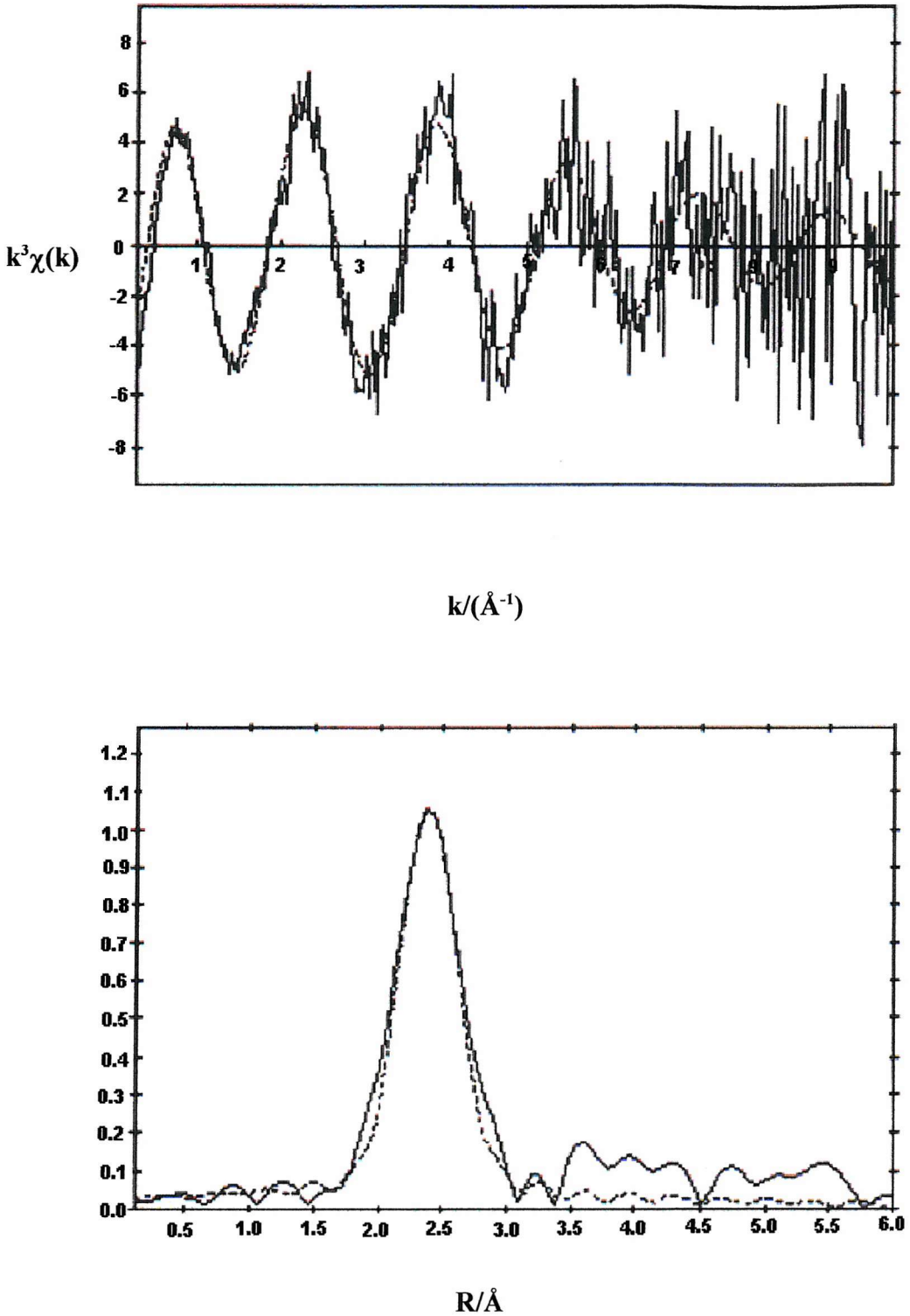

Figure 5.5 Pd K-edge k^3-weighted EXAFS data and Fourier transform of MESLC/Pd(allyl)cp, phase shift corrected for C.

(— Experimental, ----- Theory)

	N[a]	R/Å	A/Å^{2b}
MCM-41(A)/Pd(allyl)cp	5C	2.271(3)	0.005(2)
	2O	2.419(4)	0.013(1)
R-factor = 28.5%	2Si	3.125(5)	0.028(4)
KMES/Pd(allyl)cp	5C	2.126(1)	0.015(4)
	2O	2.454(3)	0.016(2)
R-factor = 32.3%	2Si	3.31(2)	0.085(2)
MESLC/Pd(allyl)cp	5C	2.124(1)	0.008(3)
	1O	2.482(1)	0.029(9)
R-factor = 21.8%	1Si	3.12(7)	0.031(1)

[a]Coordination number; [b]Debye-Waller factor A = $2\sigma^2$, σ = mean square internuclear separation. Statistical errors derived in Excurve92 given in parentheses.

Table 5.2 Pd K-edge EXAFS derived structural parameters for MCM-41(A), KMES and MESLC modified with Pd(allyl)cp

Debye-Waller factors and a relatively high R-factor of 56%. This eliminated the interaction of the Pd-cp unit with a two surface silanol groups (model B). Fitting the data to models A and C resulted in a best fit of one shell of five carbon atoms at 2.124(1) Å, a second shell of one oxygen atom at 2.482(1) Å making both interactions viable. On fitting a third shell of silicon atoms, a best fit was achieved with one silicon atom at 3.12(7) Å. This shell was statistically significant at a 95% probability level and resulted in a low R-factor of 21.8%. Fitting two silicon atoms increased the R-factor and made the Debye-Waller factors very low. This eliminates model C and suggests that in the MESLC system, the Pd-cp unit interacts with the silica surface via one single silanol linkage (model A). The EXAFS derived parameters for the reaction of all three systems are listed in table 5.2.

The EXAFS and Fourier transform spectra obtained for each system were similar to each other and best fits were obtained for modelling a Pd-cp unit attached to the surface of the silica via two oxygen interactions (model B) for MCM-41(A) and KMES, and a Pd-cp unit attached to the silica surface via one oxygen interaction (model A) for the MESLC system.

The structural parameters were within optimum specifications and the R-factor was <33% in all cases. The structures of the modified silicas were examined by TEM and the hexagonal structures were found to be intact. Examination of some enlarged photographs showed some blockage in the channels but it was impossible to emphatically correlate this to the Pd-cp units, however, the pore diameter of the channels were 15-18 Å, 25-28 Å and 24-28 Å for MCM-41(A)/pd(allyl)cp, MESLC/Pd(allyl)cp and KMES/Pd(allyl)cp, respectively. The pore diameters of the unmodified silicas were more discrete. The surface area of each modified sample was also measured and a marked increase of 120-170 m^2 g^{-1} was noted for each sample compared to the unmodified silica. The initial pink/red coloration on introduction of the organopalladium species to dry silica indicates physisorbtion on the surface of the silica but the change to yellow indicates a reaction between the silica support and the organopalladium species. The palladium loading on each sample was examined by AAS and was found to be approximately 0.9-1.8 weight % Pd which is low but as expected for these types of materials.

5.2 EXAFS study of the MCM-41(A)/Pd(allyl)cp system

The modification of MCM-41(A) with Pd(allyl)cp was monitored by EXAFS using the adapted cell shown in figure 4.4. The silica was dehydrated for 2 h at 200°C and mixed with dry pentane (in a glove box) to form a slurry which was applied to the foil covered surface of the plunger in layers allowing time between each application for the layer to dry. Pd(allyl)cp was introduced to the system using the same method as that used for the introduction of volatile organogallium and organoaluminium species (see section 4.2). Each segment of the apparatus was placed under vacuum and filled with an atmosphere of argon prior to the introduction of Pd(allyl)cp from a sealed cell by gently heating the cell and allowing sublimation onto the silica to take place.

EXAFS analysis

The EXAFS and Fourier transform were derived from X-ray absorption spectra (figure 5.6) obtained at room temperature after 1 h of exposure during which time the change in colour from pink/red to yellow was observed. The spectra were similar to those seen in figure 5.3 and was indicative of the loss of the allyl group leaving a Pd-cp unit anchored to the silica support via surface silanol groups. The data was best fitted to a shell of five carbon atoms at 2.19(6) Å, two oxygen atoms at 2.57(9) Å and a third shell of two silicon atoms at 3.2(1) Å with an R-factor of 47.1%. The third shell for this and subsequent analyses were tested for statistical significance and were found to be significant at the 95% probability level. The cell was placed under vacuum and the spectra recorded are presented in figure 5.7. The best fit was obtained with a shell of five carbons at 2.10(6) Å, a shell of two oxygen atoms at 2.58(3) Å and a third shell of two silicon atoms at 3.21(4) Å with a R-factor of 48.2%.

The system was kept under vacuum ($1.5x10^{-3}$ atm) and the cell was heated from room temperature to 80°C, 120°C and then to 180°C, holding the cell at each temperature for several hours during which time the spectra were recorded (figures 5.8, 5.9 and 5.10). In each case the data was modelled to three shells of five carbon atoms, two oxygen atoms and two silicon atoms, respectively, (corresponding to model B, figure 5.1) and the derived bond-lengths were similar to those derived for the system under vacuum. The Debye-Waller factors were within acceptable parameters and R-factors were all <51%. In previous studies, it was reported that at temperatures above 150°C, the stability of the Pd-cp unit is compromised and the organometallic species decomposed to metallic palladium however, in this study, it was found that even at 180°C, the Pd-cp unit remained intact. An attempt was made to fit the data obtained at this temperature (figure 5.10) to metallic palladium but this fit was not statistically significant. It was also noted that the best fit obtained for this data had a lower R-factor (31.7%) than those obtained for the other conditions in this series of experiments. An attempt was also made to model the data obtained from these experiments to a model of the Pd-cp unit attached to the surface of the silica via a single silanol group (model A, figure 5.1) but this resulted in higher R-factors of approximately 20-30% and either high or negative Debye-Waller factors so this model was discarded.

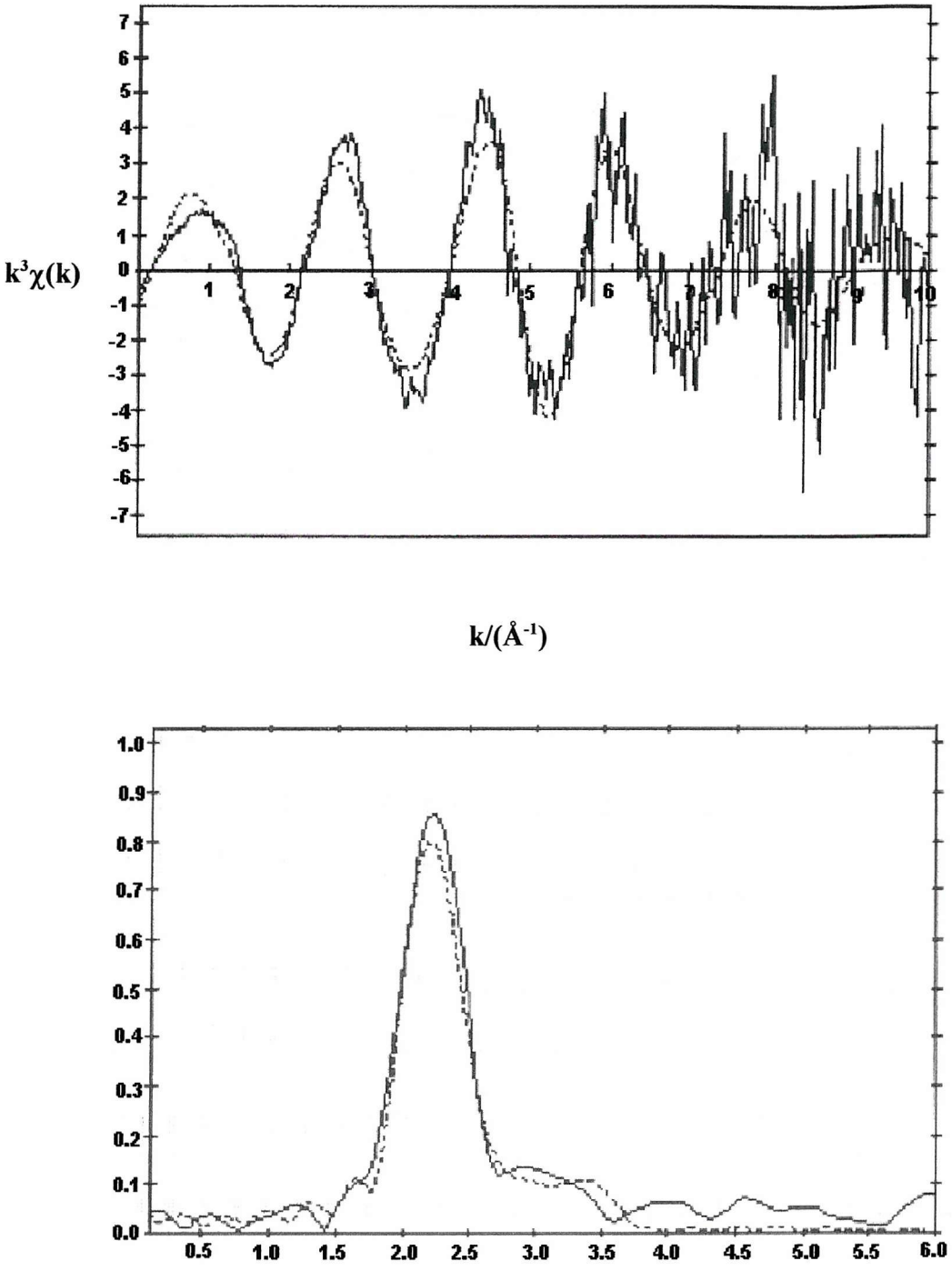

Figure 5.6 Pd K-edge k^3-weighted EXAFS data and Fourier transform of MCM-41(A)/ Pd(allyl)cp/room temperature, phase shift corrected for C.

(— Experimental, ----- Theory)

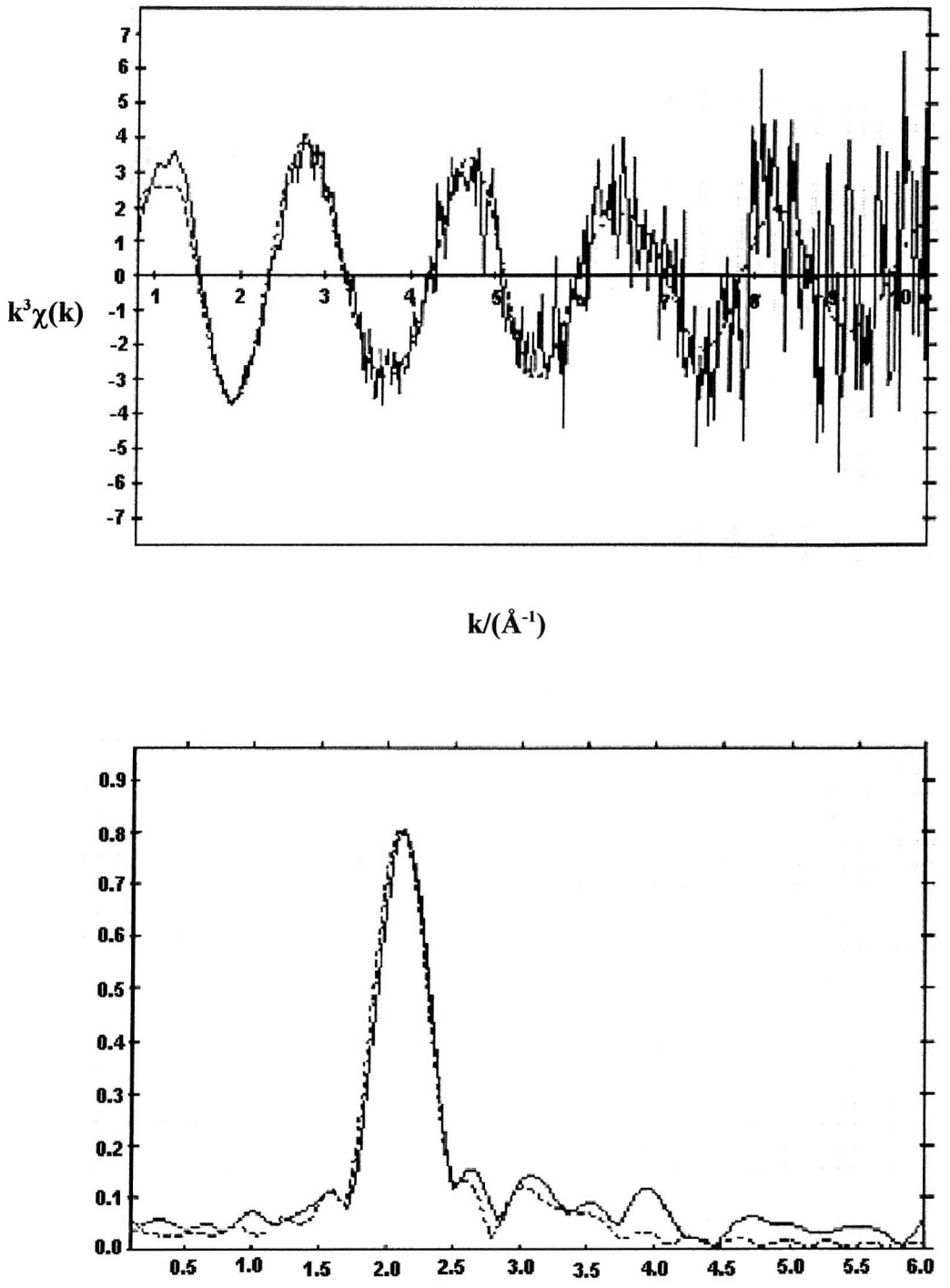

Figure 5.7 Pd K-edge k^3-weighted EXAFS data and Fourier transform of MCM-41(A)/Pd(allyl)cp/under vacuum, phase shift corrected for C. (— Experimental, ----- Theory)

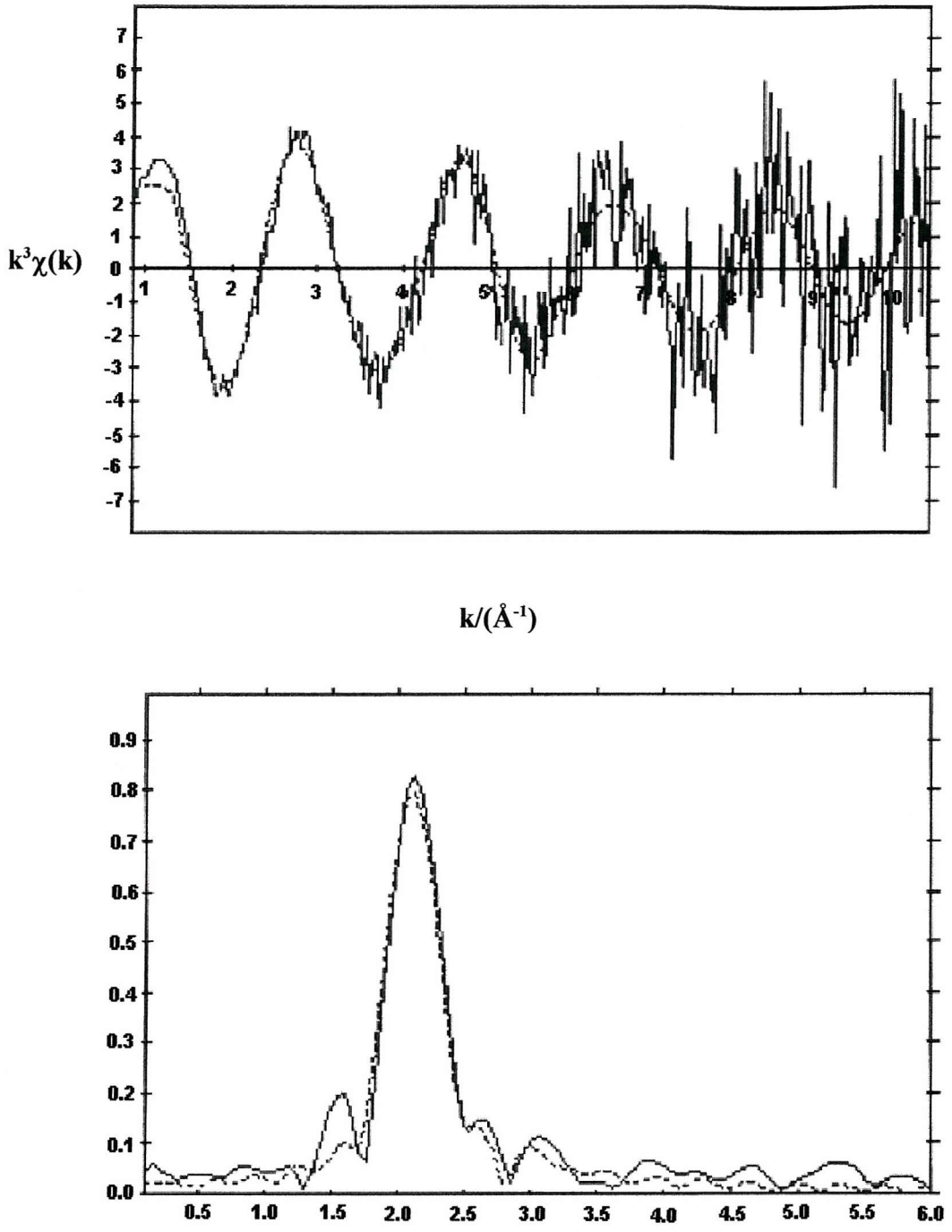

Figure 5.8 Pd K-edge k^3-weighted EXAFS data and Fourier transform of MCM-41(A)/Pd(allyl)cp/under vacuum/80°C, phase shift corrected for C. (— Experimental, ----- Theory)

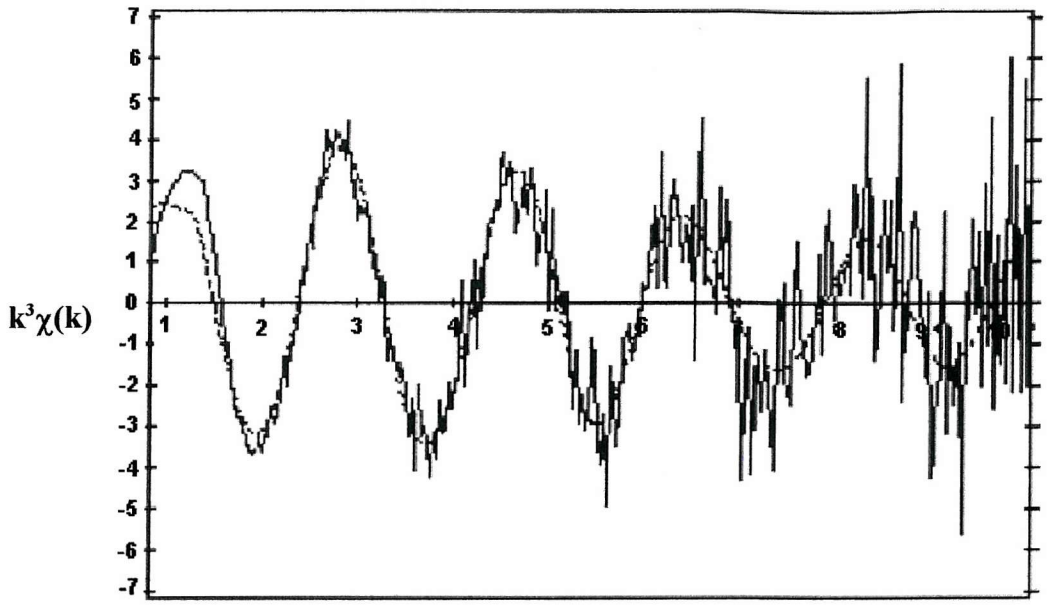

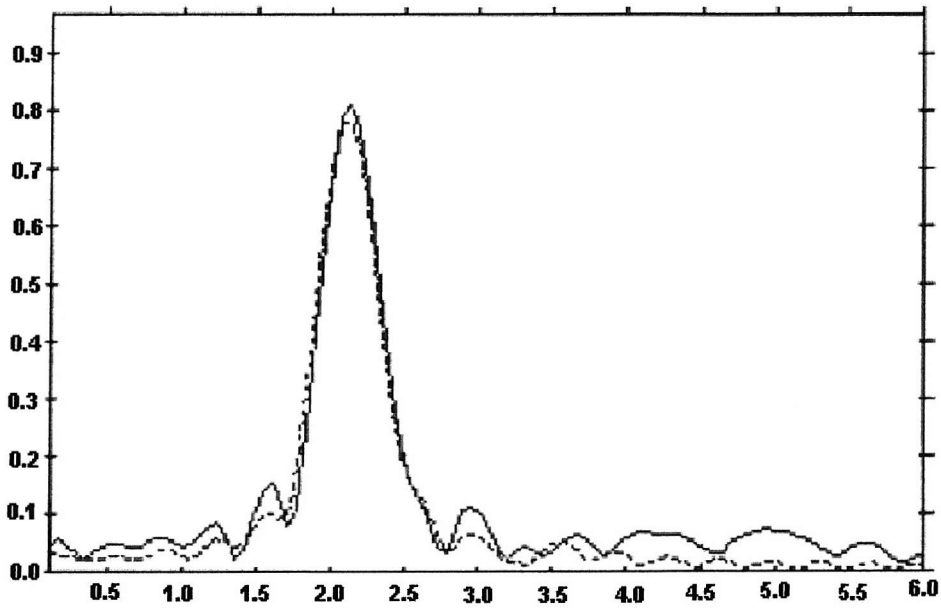

Figure 5.9 Pd K-edge k^3-weighted EXAFS data and Fourier transform of MCM-41(A)/Pd(allyl)cp/under vacuum/120°C, phase shift corrected for C. (— Experimental, ----- Theory)

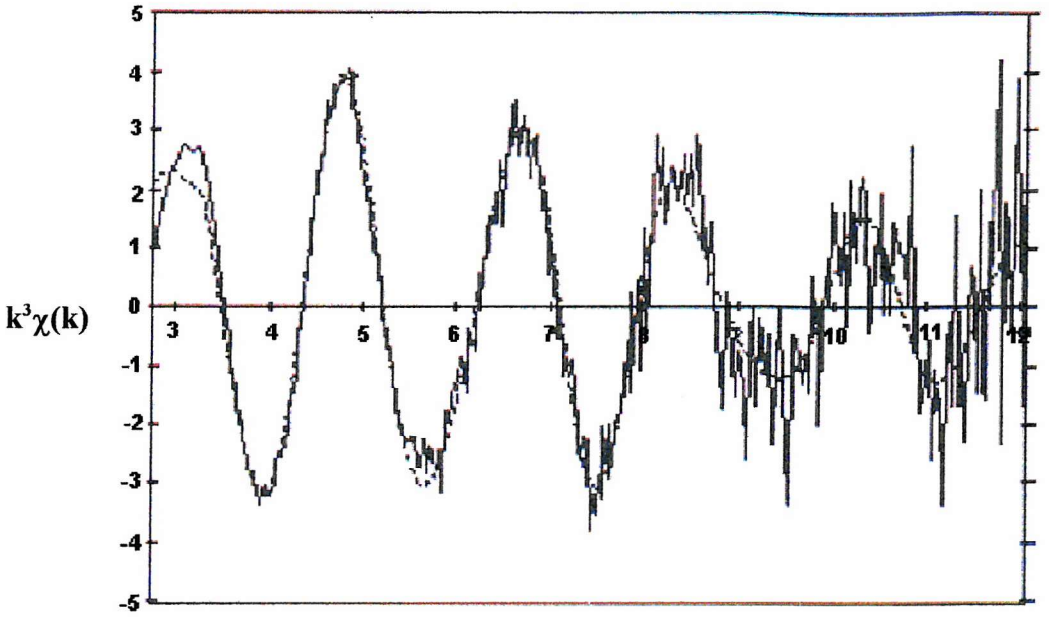

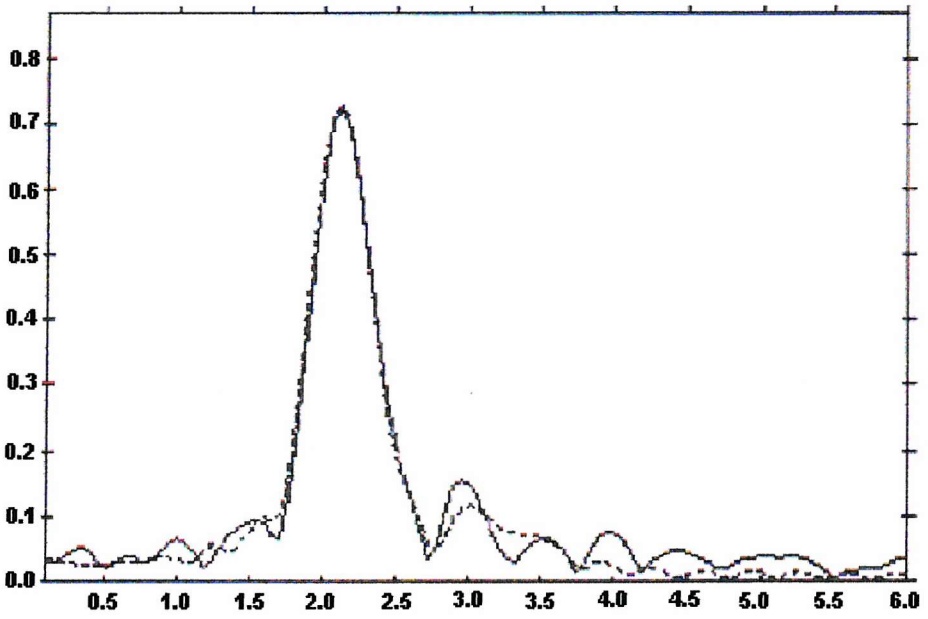

Figure 5.10 Pd K-edge k^3-weighted EXAFS data and Fourier transform of MCM-41(A)/Pd(allyl)cp/under vacuum/180°C, phase shift corrected for C. (— Experimental, ----- Theory)

At the next stage of the experiment, the temperature of the system was reduced to 100°C and $Zn(C_2H_5)_2$ was introduced to the cell as described previously (see section 4.3). In an atmosphere of $Zn(C_2H_5)_2$ vapour, the EXAFS and Fourier transform spectra (figure 5.11) were noisy and the R-factor was relatively high at 68% but it was still possible to fit the data to the model with a first co-ordination sphere of five carbon atoms at 2.04(2) Å, indicating an intact cp unit. The best fit was achieved with shell of two oxygen atoms at 2.4(2) Å and a shell of two silicon atoms at 3.009(3) Å both of which are shorter than those derived prior to the addition of $Zn(C_2H_5)_2$. It was also possible to statistically fit a fourth shell of 1.7 zinc atoms at a distance of 3.40(2) Å from the palladium centre.

The temperature of the system was then increased to 180°C and a marked change in the recorded EXAFS and Fourier transform spectra could be seen (figure 5.12). The data did not fit well to the previous models but analysis of the data (table 5.3) resulted in a best fit consisting of five carbon atoms at 2.09(4) Å and a second shell of nine palladium atoms at 2.762(2) Å suggesting that at the higher temperature some of the Pd-cp units have decomposed leaving a mixture of metallic palladium and some intact Pd-cp units. It was also possible to fit a shell of two zinc atoms at 3.41(6) Å which was statistically significant at a 95% probability level. It is unlikely that the zinc atoms are directly interacting with the palladium species and this shell is probably due to residual zinc species within the silica pores.

The final stage of this experiment looked at the sample from the Zn metal edge. Figure 5.13 shows the Zn K-edge EXAFS spectrum and its Fourier transform. Analysis of the data resulted in a best fit of three oxygen atoms at 1.92(7) Å, a single carbon atom at 2.416 Å and three silicon atoms at 3.54(2) Å, all of which are consistent with an ethylzinc species anchored to the surface of the silica via three oxygen species forming a stable four-coordinate centre. It was also possible to fit a fourth shell of 1.5 palladium atoms at 2.50(4) Å which may be due to metallic palladium particles. The Debye-Waller factors were within acceptable parameters and the R-factor for the analysis was 32.5%. The EXAFS derived structural parameters for this series of experiments (corresponding to figures 5.6-5.13) are presented in table 5.3.

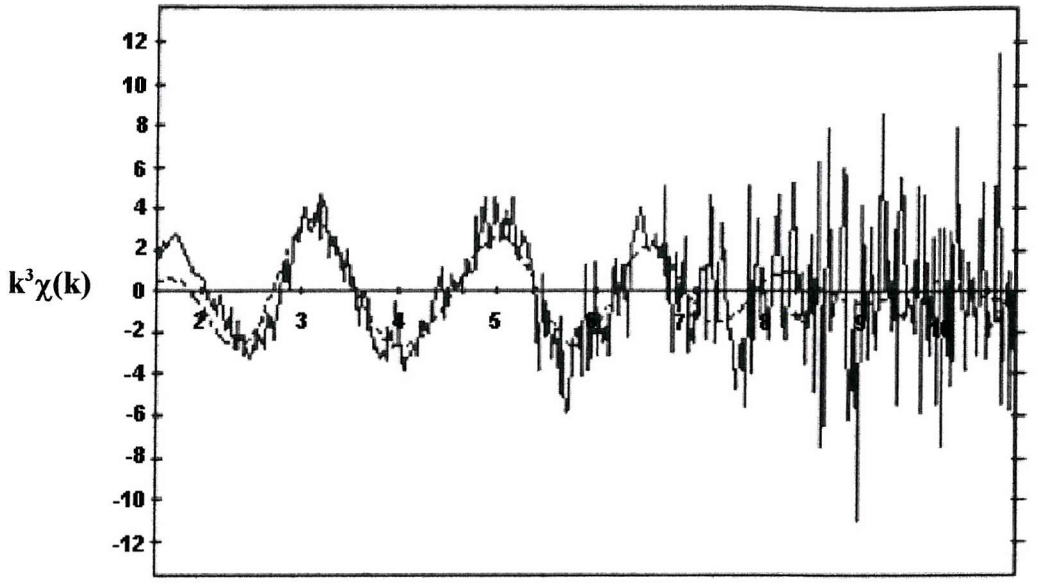

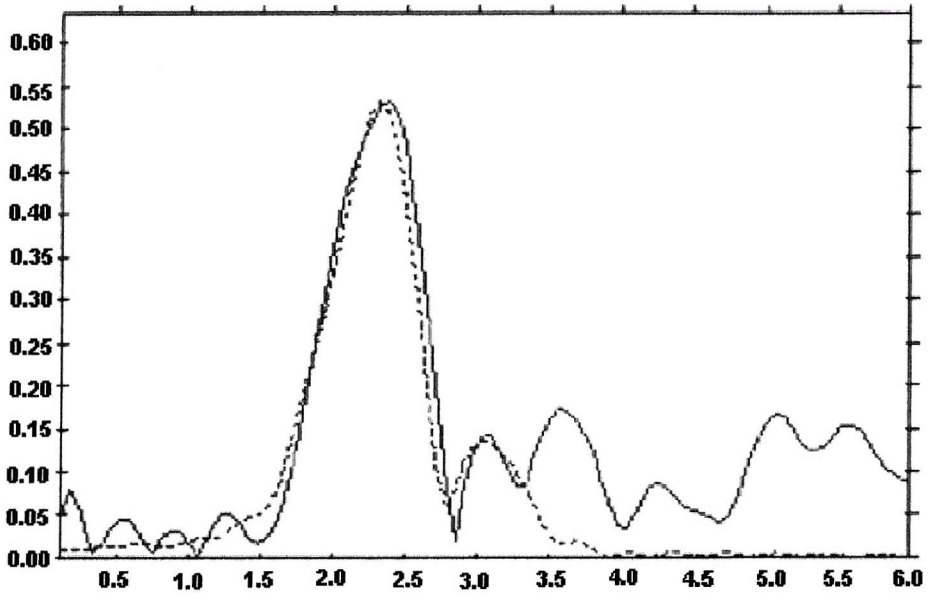

Figure 5.11 Pd K-edge k^3-weighted EXAFS data and Fourier transform of MCM-41(A)/Pd(allyl)cp/under vacuum/180°C/$Zn(C_2H_5)_2$/100°C, phase shift corrected for C. (— Experimental, ----- Theory)

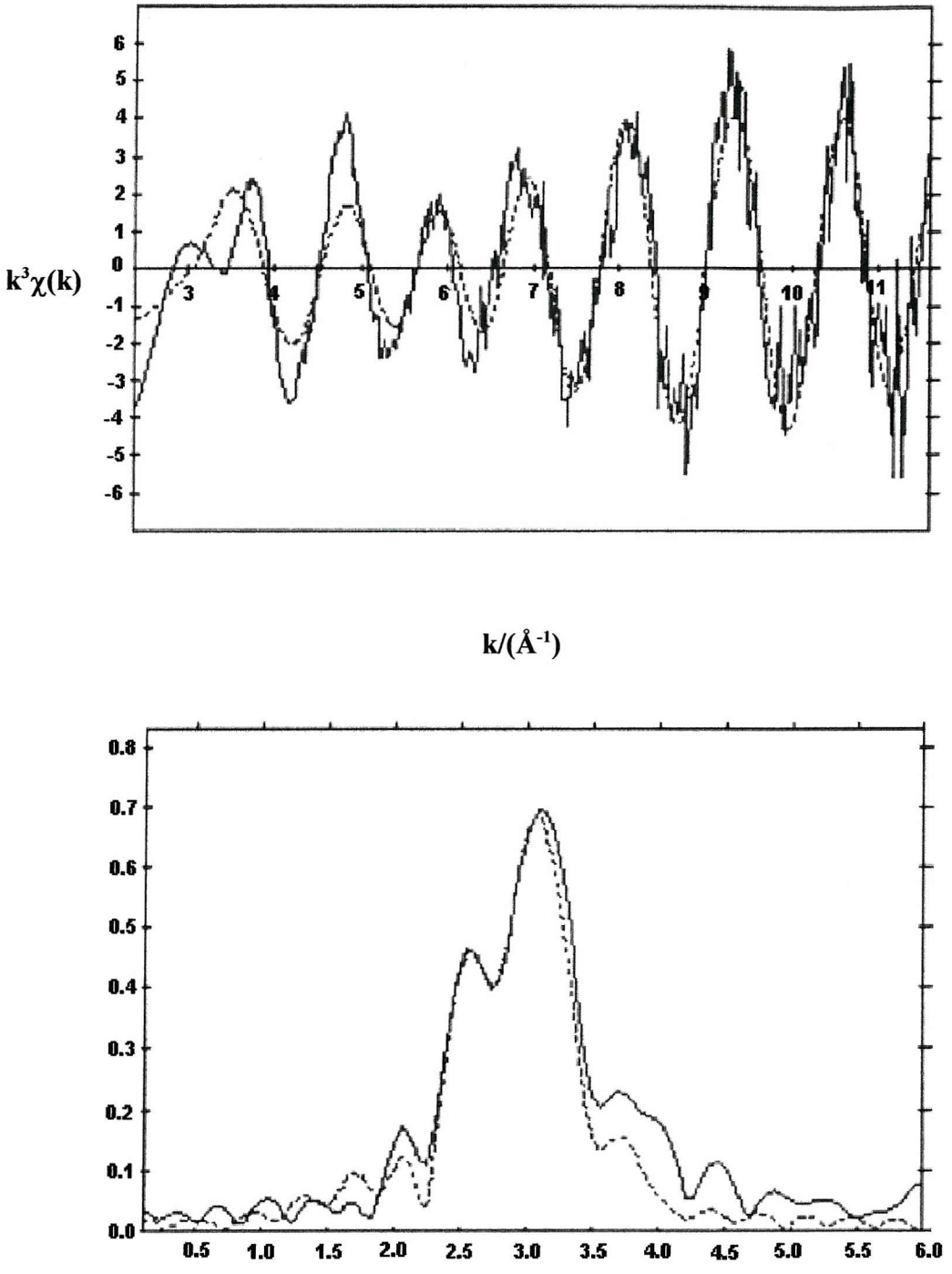

Figure 5.12 Pd K-edge k^3-weighted EXAFS data and Fourier transform of MCM-41(A) /Pd(allyl)cp/under vacuum/180°C/Zn(C_2H_5)$_2$/180°C, phase shift corrected for C. (— Experimental, ----- Theory)

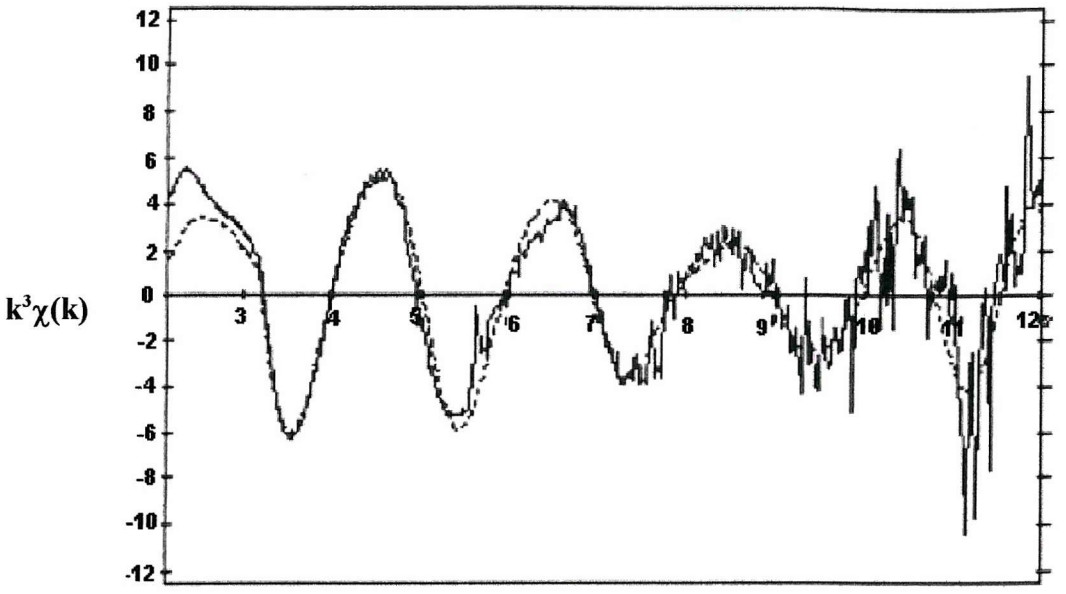

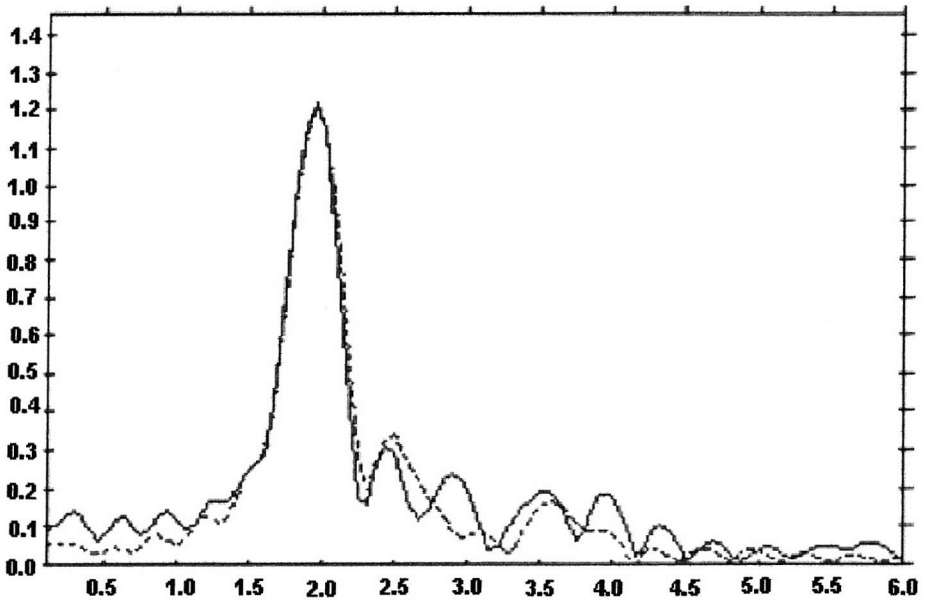

Figure 5.13 Zn K-edge k^3-weighted EXAFS data and Fourier transform of MCM-41(A) /Pd(allyl)cp/under vacuum/180°C/$Zn(C_2H_5)_2$/100°C, phase shift corrected for C. (— Experimental, ----- Theory)

	N[a]	R/Å	A/Å^{2b}
MCM-41(A)/Pd(allyl)cp/RT *R-factor = 47.1%*	5C 2O 2Si	2.19(6) 2.57(9) 3.2(1)	0.005(8) 0.00(4) 0.01(5)
MCM-41(A)/Pd(allyl)cp/under vacuum *R-factor = 48.2%*	5C 2O 2Si	2.10(6) 2.58(3) 3.2(2)	0.006(8) 0.025(9) 0.019(5)
MCM-41(A)/Pd(allyl)cp/under vacuum/ 80 °C *R-factor = 50.1%*	5C 2O 2Si	2.109(6) 2.58(3) 3.21(4)	0.006(8) 0.023(9) 0.028(1)
MCM-41(A)/Pd(allyl)cp/under vacuum/ 120 °C *R-factor* = 46.7%	5C 2O 2Si	2.10(6) 2.55(2) 3.1(4)	0.007(7) 0.015(4) 0.038(1)
MCM-41(A)/Pd(allyl)cp/under vacuum/ 180 °C *R-factor = 31.7%*	5C 2O 2Si	2.11(4) 2.55(9) 3.15(1)	0.009(6) 0.015(3) 0.019(4)
MCM-41(A)/Pd(allyl)cp/under vacuum/ 100 °C/$Zn(C_2H_5)_2$ *R-factor = 68.0%*	5C 2O 2Si 1.7Zn	2.04(2) 2.4(2) 3.009(3) 3.40(2)	0.025(5) 0.010(3) 0.019(7) 0.015(5)
MCM-41(A)/Pd(allyl)cp/under vacuum/ 180 °C/$Zn(C_2H_5)_2$ *R-factor = 44.6%*	5C 9Pd 2Zn	2.09(4) 2.762(2) 3.41(6)	0.012(2) 0.021(6) 0.014(2)
MCM-41(A)/Pd(allyl)cp/under vacuum/ 180 °C/$Zn(C_2H_5)_2$ (Zn edge) *R-factor = 32.5%*	1C 3O 3Si 1.5Pd	2.016(1) 1.92(7) 3.54(2) 2.50(4)	0.005(1) 0.012(2) 0.023(4) 0.03(1)

[a]Coordination number; [b]Debye-Waller factor A = $2\sigma^2$, σ = mean square internuclear separation. Statistical errors derived in Excurve92 given in parentheses.

Table 5.3 EXAFS derived structural parameters for MCM-41(A)/Pd(allyl)cp system; Pd K-edge unless otherwise stated.

5.3 EXAFS study of the MCM-41(A)/$Pd(CH_3CN)_2(NO_2)Cl$ system

The modification of mesoporous silica MCM-41(A) with the organopalladium species $Pd(CH_3CN)_2(NO_2)Cl$ was studied by EXAFS. $Pd(CH_3CN)_2(NO_2)Cl$ was chosen due its known ability to catalyse the oxidation of alkenes.[14,15] The organometallic species is expected to react with the silanol groups of the silica support with the loss of the two labile acetonitrile ligands[16] leaving a stable $Pd(NO_2)Cl$ unit anchored to the silica support (figure 5.14).

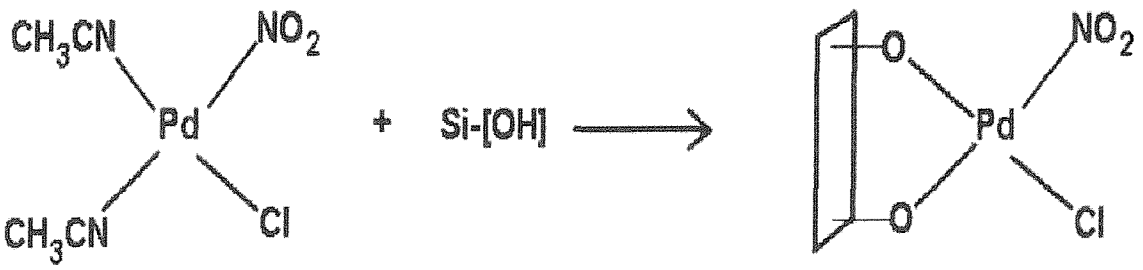

Figure 5.14 Reaction of $Pd(CH_3CN)_2(NO_2)Cl$ with MCM-41(A)

Preparation of MCM-41(A)/$Pd(CH_3CN)_2(NO_2)Cl$

MCM-41(A) silica (0.25 g) was dehydrated at 200°C for 2 h under vacuum and then mixed with dry, degassed tetrahydrofuran (5 ml) to form a suspension. $Pd(CH_3CN)_2(NO_2)Cl$ (0.025 g, 9.26 x 10^{-5} mol) was dissolved in 10 ml dry tetrahydrofuran and this solution was transferred to the silica suspension. The reaction mixture was allowed to stir overnight and then the solid was allowed to settle. The upper solution layer was removed and fresh dry, degassed tetrahydrofuran was added and the mixture was stirred for 10 min. This process was repeated several times and the resulting pale beige-brown solid was dried under vacuum over several hours. The sample was Soxhlet-extracted with dry, degassed acetonitrile and then dried under vacuum. The solid residue (0.18 g) was stored in an inert atmosphere.

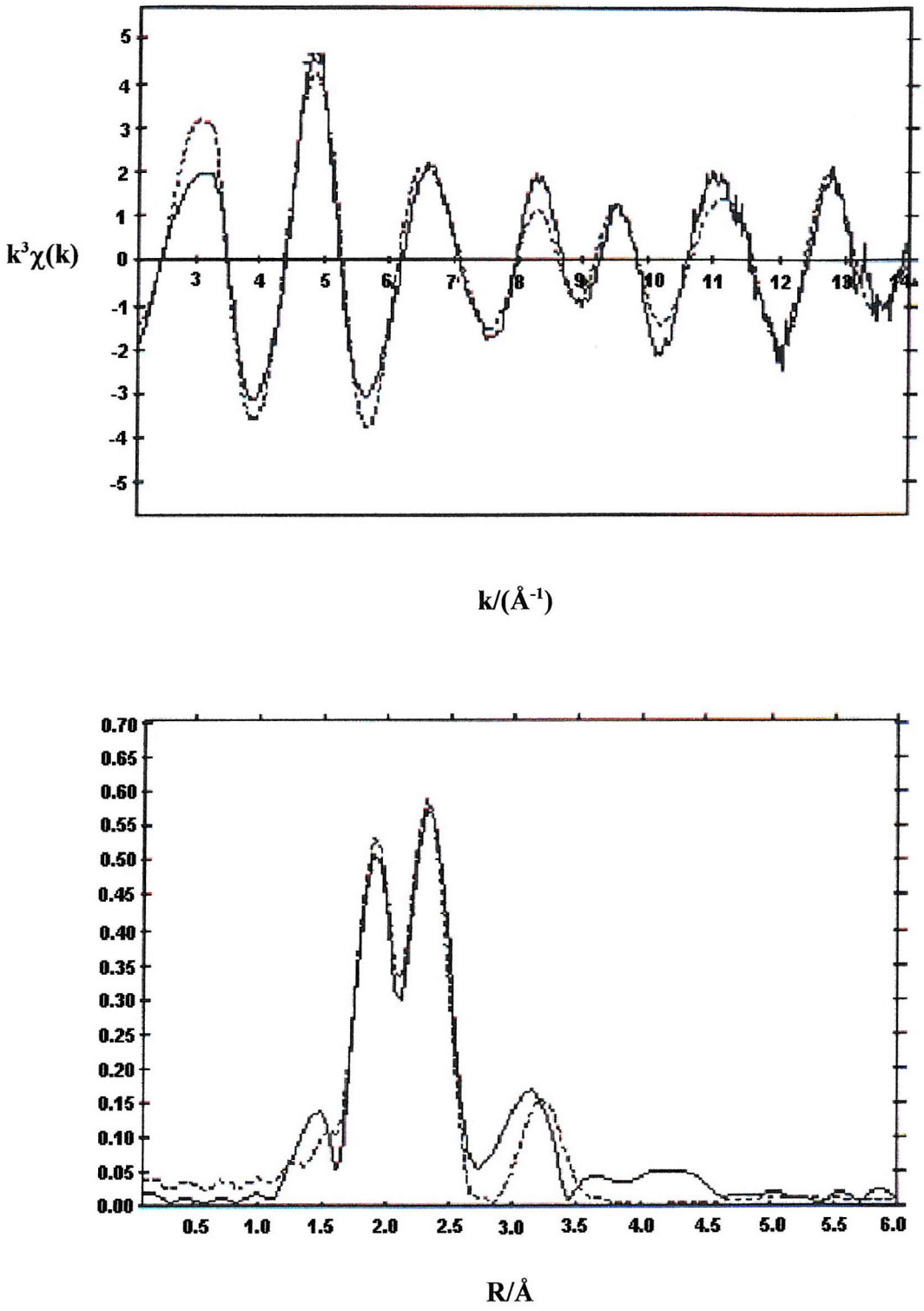

Figure 5.15 Pd K-edge k^3-weighted EXAFS data and Fourier transform of $Pd(CH_3CN)_2(NO_2)Cl$/BN, phase shift corrected for N.

(— Experimental, ----- Theory)

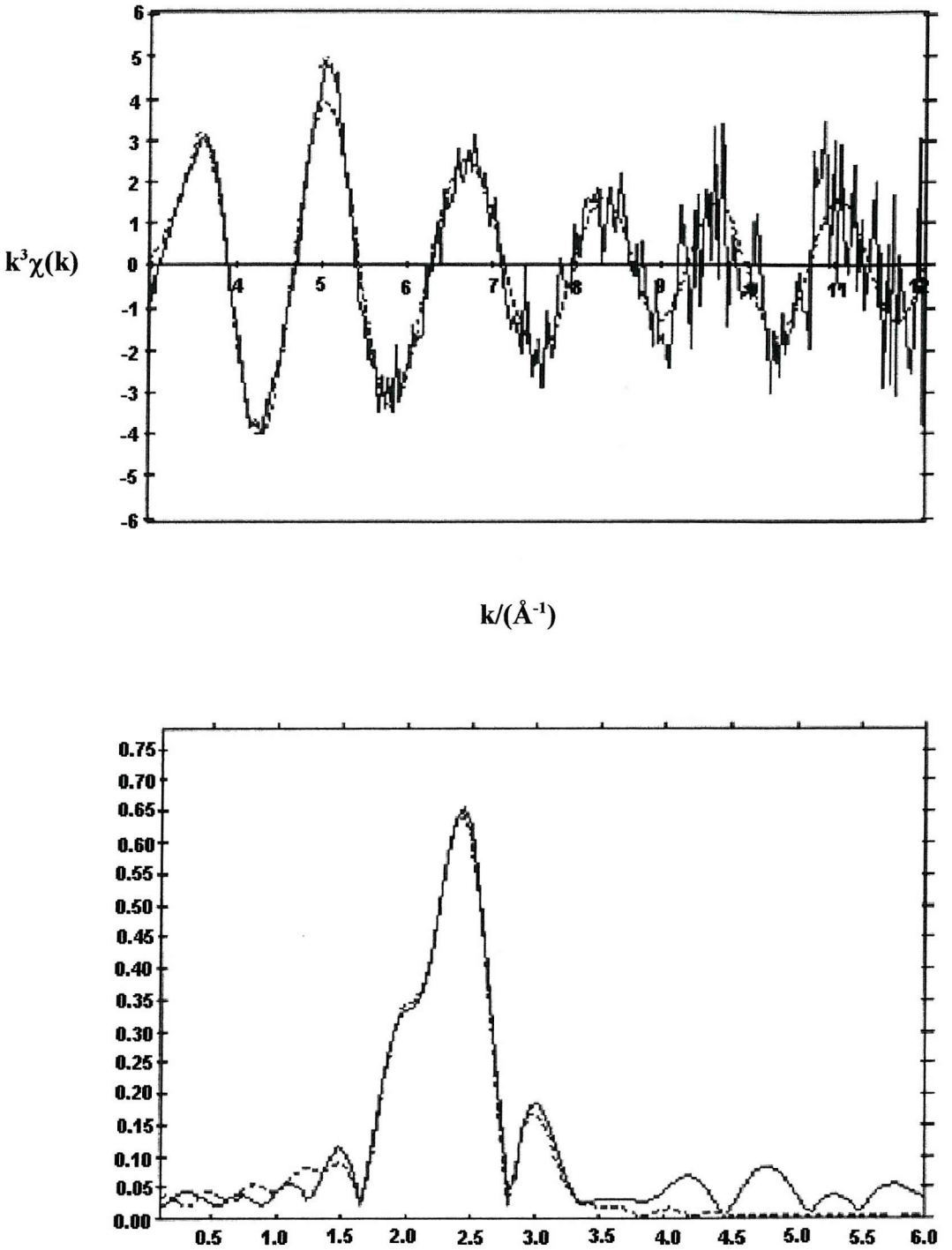

Figure 5.16 Pd K-edge k^3-weighted EXAFS data and Fourier transform of MCM-41(A)/Pd(CH_3CN)$_2$(NO_2)Cl, phase shift corrected for N. (— Experimental, ----- Theory)

Characterisation

The structure of the MCM-41(A)/$Pd(CH_3CN)_2(NO_2)Cl$ system was studied by TEM and the characteristic hexagonal structure of MCM-41(A) was noted. Some blockage in the channels were observed. The pore diameter was determined from enlarged TEM photographs as 16-19 Å. The BET surface area of the modified silica was 1572 m^2g^{-1} [1422 m^2g^{-1} for unmodified MCM-41(A)]. The palladium loading, as determined by AAS, was approximately 2.1 weight% Pd.

EXAFS analysis

The EXAFS spectra and Fourier transform of $Pd(CH_3CN)_2(NO_2)Cl$ mixed with 10 wt.% BN was recorded and is presented in figure 5.15. The EXAFS derived structural parameters are listed in table 5.4. The data was fitted to a first shell of two nitrogen atoms at 1.98(3) Å and a second shell of two carbon atoms at 3.15(9) Å which correspond to the two acetonitrile ligands in the organometallic complex. The NO_2 group was fitted to shell of one nitrogen atom at 2.11(4) Å and a shell of two oxygen atoms at 3.21(4) Å. The chlorine atom was fitted at 2.32(2) Å. Each shell was statistically significant at the 95% probability level and had Debye-Waller factors which were within reasonable parameters. The R-factor was 23.5%. Comparison of the interatomic distances to literature values was favourable with Pd-N distances of 1.95 Å and Pd....C distances of 2.98 Å for acetonitrile-type ligands[17], and a Pd-N distance of 1.98 Å[18] for NO_2 ligands. The Pd-Cl interatomic distance also compares favourably to that of 2.37 Å for Pd-Cl in $Pd(NH_3)_4Cl_2$ embedded in γ-Al_2O_3 catalysts.[19]

N[a]	R/Å	A/Å[2b]
2N	1.98(3)	0.002(5)
2C	3.15(9)	0.032(7)
1N	2.11(4)	0.003(8)
2O	3.21(4)	0.005(8)
1Cl	2.32(2)	0.002(4)
R-factor = 23.5%; E_f = -3.81 eV		

[a]Coordination number; [b]Debye-Waller factor A = $2\sigma^2$, σ = mean square internuclear separation. Statistical errors derived in Excurve92 given in parentheses.

Table 5.4 Pd K-edge EXAFS derived structural parameters for $Pd(CH_3CN)_2(NO_2)Cl$/BN

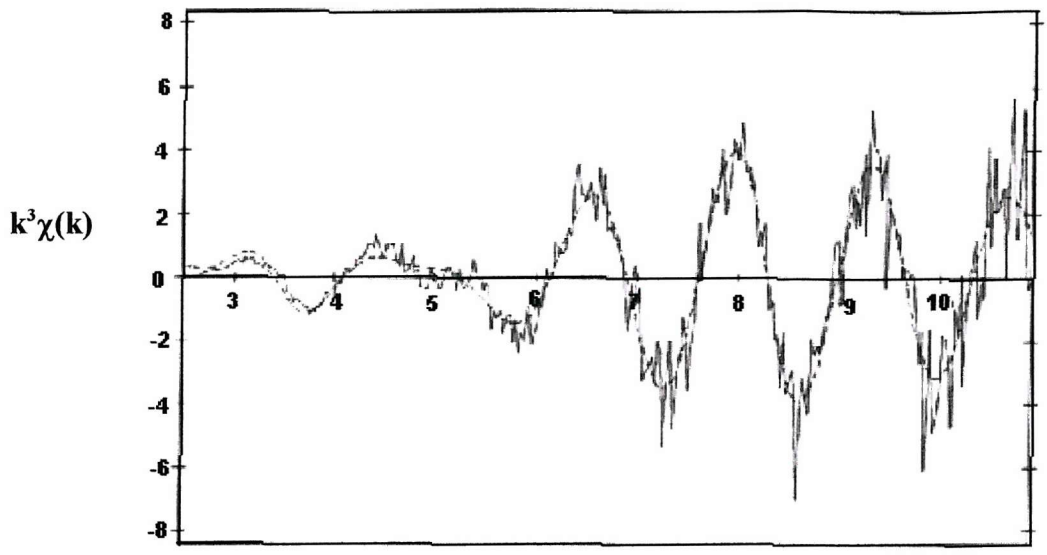

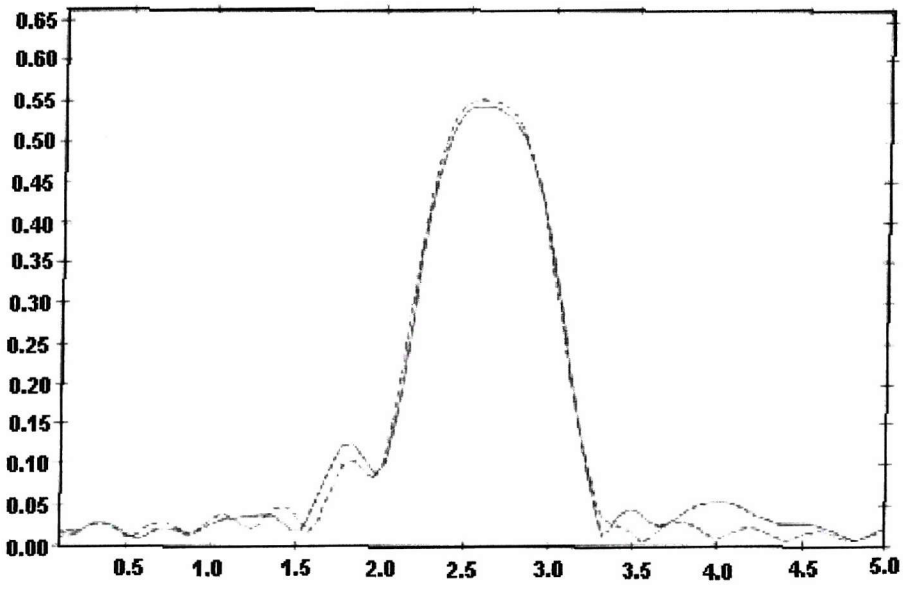

Figure 5.17 Pd K-edge k^3-weighted EXAFS data and Fourier transform of MCM-41(A)/Pd(CH_3CN)$_2$(NO_2)Cl/Ga(CH_3)$_3$/100°C, phase shift corrected for Pd. (— Experimental, ----- Theory)

The prepared MCM-41(A)/Pd(CH_3CN)$_2$(NO_2)Cl samples were mixed with dry pentane in a glove box and the resulting slurry was pipetted onto the aluminium-coated surface of the plunger of the EXAFS cell, as described previously for the Pd(allyl)cp system, forming a layer of solid material. The cell was placed in the path of the beam and X-ray absorption spectra were recorded at 25°C with the system under vacuum (1.5×10^{-3} atm). Figure 5.16 shows the EXAFS spectrum and Fourier transform of the supported organometallic species. The EXAFS derived parameters are listed in table 5.5. It is evident from the spectra that a reaction has occurred and the results suggest that the two acetonitrile groups are removed on reaction leaving a Pd(NO_2)Cl unit interacting with the surface via two silanol groups (see figure 5.14). The data was best fitted to four shells consisting of a shell of one nitrogen atom at 2.10(3) Å and a second shell of two oxygen atoms at 3.00(4) Å which corresponds to the NO_2 group, a single chlorine atom at 2.25(2) Å and a fourth shell of 2 oxygen atoms at 2.052(6) Å. It was also statistically possible to fit a fifth shell of two silicon atoms at 3.22(2) Å, further indication of interaction with the silica support. The interatomic distances correspond well with those obtained for the organometallic species alone. The R-factor was 38.1% and the Debye-Waller factors were within reasonable parameters.

The effect of trimethylgallium on the modified support was examined *in situ* by EXAFS with the trimethylgallium vapour being introduced to the system as described previously in chapter four. The trimethylgallium was expected to react with the silica of the support resulting in the loss of a methyl group with the remaining dimethylgallium unit interacting with the support via two silanol groups. The EXAFS spectrum and its Fourier transform of the system at 100°C are presented in figure 5.17. It is evident from the marked change in the spectra that a change in the co-ordination around the metal centre has occurred. Analysis of the data suggested decomposition of the organometallic species to metallic palladium. The data was best fitted to shell of six palladium atoms at 2.691(3) Å. It was also possible to fit a second shell of one oxygen atom at 1.86(4) Å and a third shell at 3.01(5) Å corresponding to one silicon atom indicating a mixture of metallic palladium and some Pd-O species interacting with the silica surface. An attempt was made to fit gallium atoms to the spectra and although this was possible, it resulted in very high Debye-Waller values and the shell was not statistically significant. The EXAFS derived structural parameters are listed in table 5.5.

	N[a]	R/Å	A/Å^{2b}
MCM-41(A)/Pd(CH_3CN)$_2$(NO_2)Cl *R-factor = 38.1%*	1N 2O 1Cl 2O 2Si	2.10(3) 3.00(4) 2.25(2) 2.052(6) 3.22(2)	0.024(5) 0.005(8) 0.013(2) 0.002(1) 0.003(2)
MCM-41(A)/Pd(CH_3CN)$_2$(NO_2)Cl/Ga(CH_3)$_3$/100 °C *R-factor = 39.4%*	6Pd 1O 1Si	2.691(3) 1.86(4) 3.01(5)	0.007(2) 0.029(3) 0.027(4)
MCM-41(A)/Pd(CH_3CN)$_2$(NO_2)Cl/Ga(CH_3)$_3$/100 °C (Ga edge) *R-factor = 40.6%*	2C 2O 2Si 1Pd 1Ga	2.03(2) 1.83(2) 3.31(1) 2.35(5) 2.87(5)	0.017(1) 0.026(2) 0.013(4) 0.014(3) 0.029(1)

[a]Coordination number; [b]Debye-Waller factor A = $2\sigma^2$, σ = mean square internuclear separation. Statistical errors derived in Excurve92 given in parentheses.

Table 5.5 EXAFS derived structural parameters for MCM-41(A)/Pd(CH_3CN)$_2$(NO_2)Cl system; Pd K-edge unless otherwise stated.

The station was recalibrated to look at the same system at the gallium edge and the EXAFS spectrum and its Fourier transform were recorded under the same conditions and are presented in figure 5.18. Analysis of the data showed that the trimethylgallium had reacted with the silica support forming a dimethylgallium species. The best fit was obtained with a shell of two carbon atoms at 2.03(2) Å, a second shell of two oxygen atoms at 1.83(2) Å and a third shell of two silicon atoms at 3.31(1) Å which correspond to the interaction of a dimethylgallium species with the silica support via two silanol groups. The interatomic distances are comparable to the interatomic distances obtained for the interaction of trimethylgallium with the unmodified support. A fourth shell of one palladium atom at a distance of 2.35(5) Å was also fitted to the data which reduced the R-factor to 45% from 59%. A statistically significant fifth shell of gallium at 2.87(5) Å was also fitted which further reduced the R-factor to 40.6%. The EXAFS derived structural parameters are listed in table 5.5.

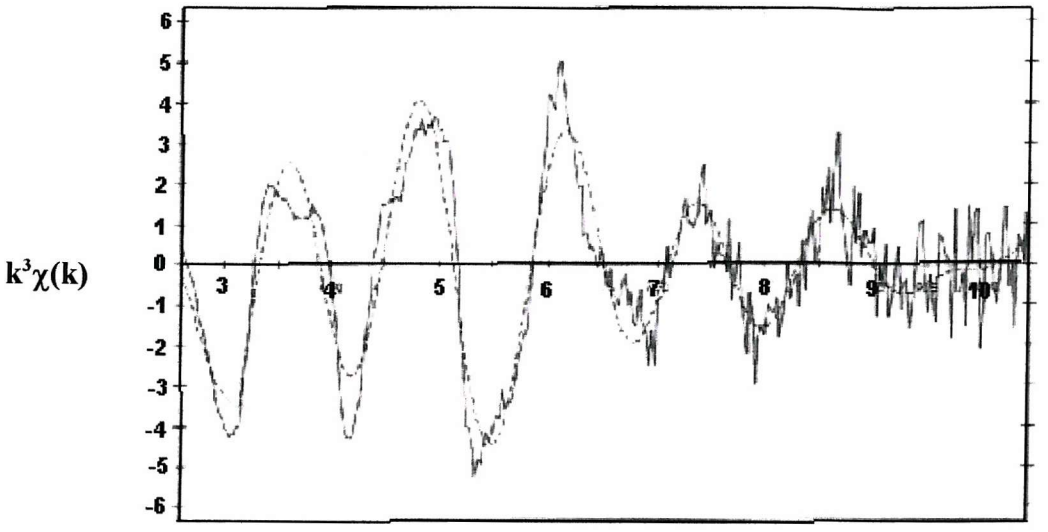

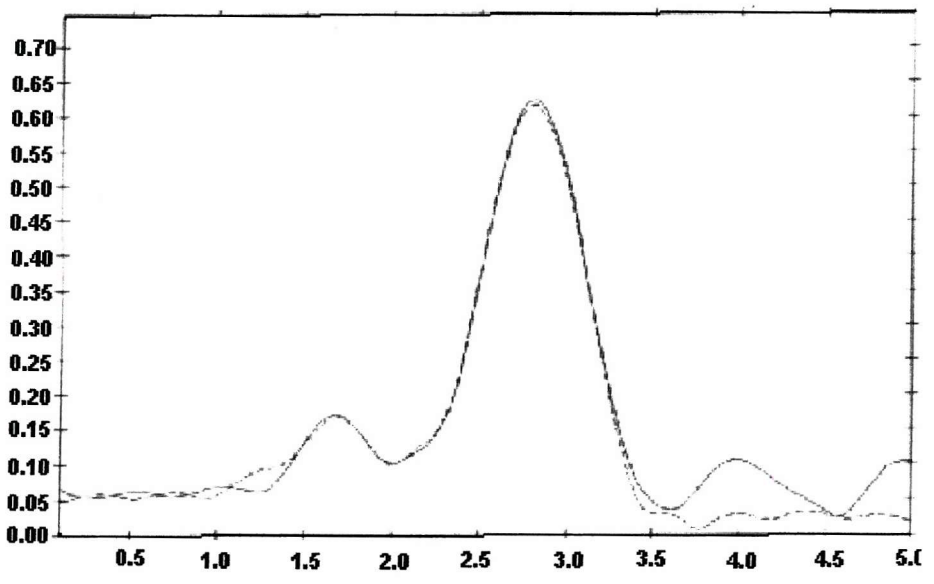

Figure 5.18 Ga K-edge k^3-weighted EXAFS data and Fourier transform of MCM-41(A)/Pd(CH_3CN)$_2$(NO_2)Cl/Ga(CH_3)$_3$/100 °C, phase shift corrected for C. (— Experimental, ----- Theory)

5.4 Phosphine-functionalized mesoporous silica

One method of binding organometallic species to the surface of mesoporous silica is to use a linking compound. This would then bind to both the silica surface and the organometallic species. The aim of this part of the research was to find out whether phosphine ligands other than bi-functional phosphine siloxanes could act as linkers between the surface of the silicas and the organometallic species.

As most transition metals form stable complexes with phosphines, it has been suggested[20] that bifunctional phosphines such as $Ph_2P(CH_2)_3Si(OEt)_3$ and $Ph_2P(CH_2)_2Si(OEt)_3$ would make good linkers as not only are they relatively easy to synthesize[21] and form strong linkages to the support via condensation of the three ethoxy groups but they also reduce unwanted side reactions with the silica surface (figure 5.19).

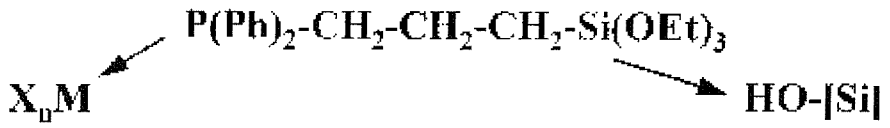

Figure 5.19 Reaction of metal complexes with bifunctional phosphines

Similarly, the reaction of trifunctional phosphines such as tri(hydroxypropyl)phosphine $[P(C_3H_6OH)_3]$, which contains -OH moieties should cause the phosphine to bind to the surface of mesoporous silicas at one end and to transition metal complexes at the other end (figure 5.22). The interactions of several phosphines with mesoporous silicas were investigated but only one example is presented here.

5.4.1 MCM-41(A) functionalized with $P(C_3H_6OH)_3$

The phosphine $P(C_3H_6OH)_3$ was an extremely moisture-sensitive viscous oil which was commercially available. All manipulations of the phosphine took place in a glove box.

Synthesis

MCM-41(A) silica (0.2 g) was dehydrated at 200°C for 2 h under vacuum and dry, degassed ethanol (5 ml) was added to form a suspension. Dry, degassed ethanol (10 ml) was added to $P(C_3H_6OH)_3$ (0.22 g; weighed by difference) and the resulting solution was transferred to the silica suspension. The mixture was stirred overnight and then the solid phase was allowed to settle. The upper solvent layer was removed, dry ethanol (10 ml) was added and the mixture was stirred for a further 10 min. This process was repeated several times, the suspension was filtered (under argon) and the residue was placed under vacuum for several hours. The sample was Soxhlet-extracted with dry, degassed acetonitrile, dried under vacuum and the resultant off-white solid (0.18 g) was stored in an inert atmosphere.

Characterisation

The BET surface area measurement (obtained from the Gemini 2375) for the phosphine-functionalized silica was 1376 m^2g^{-1}, which at slightly less than that of the unmodified MCM-41(A) [1422 m^2g^{-1}], is still well within the mesoporous range. The reduction in surface area could be due to some blockage of the channels at the channel entrances which would prevent access to the inner space, however, this would manifest itself as a larger decrease in the internal surface area due to the vast internal surface area of the silica than is noted in this case.

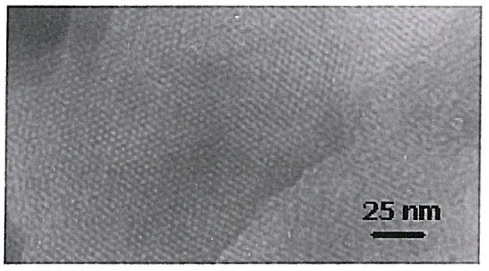

Figure 5.20 TEM (enlarged) of MCM-41(A) functionalized with $P(C_3H_6OH)_3$

Preparing a sample of the phosphine-functionalized silica for transmission electron microscopy proved difficult due to the phosphine being so air-sensitive, however, the electron micrograph (figure 5.20) shows that the integrity of the structure remains unchanged and the hexagonal pores are clearly visible. The pore diameter, estimated from the enlarged picture, was 22-25 Å.

Figure 5.21 shows three signals indicating three different phosphorus environments in the ^{31}P MAS NMR spectra of MCM-41(A) functionalized with $P(C_3H_6OH)_3$ [referenced to 85 weight% H_3PO_4]. The signal at δ -30.7 ppm is assigned to the phosphine ligand (phosphorus chemical shift of δ -23.11 ppm) and the broadening at the base of the signal is indicative of some immobilization. Chemical bonding to silica surfaces via the -OH moiety of a phosphine ligand is relatively unusual compared to chemical bonding via the phosphorus atom or the incorporation of phosphorus centres (as phosphine ligands) into the mesoporous structure.[22,23] However the signal for the immobilized phosphine is close to that of immobilized framework phosphorus nuclei within zeolite type structures which exhibit shift ranges of δ -14 to δ -31 ppm,[24-26] whereas surface bonded phosphines attached to the silica via the phosphorus atom show shift ranges further downfield[27,28] and are usually positive. The signal at δ 37.8 ppm is assigned to unreacted $P(C_3H_6OH)_3$ [*cf.* phosphinoalkenes at δ 36-70 ppm[29] and hydroxymethylphosphine at δ 20.8 ppm[30]] and the signal at δ 57.1 ppm could be due to phosphine oxide contaminants[31] or surface bonded phosphines. A likely scenario for this

reaction is that a mixture of phosphorous environments are present in the silica as undoubtedly some P-C bonds in the $P(C_3H_6OH)_3$ compound may have been broken on some phosphorus atoms and thereby allowing chemical bonding via the phosphorus atoms.

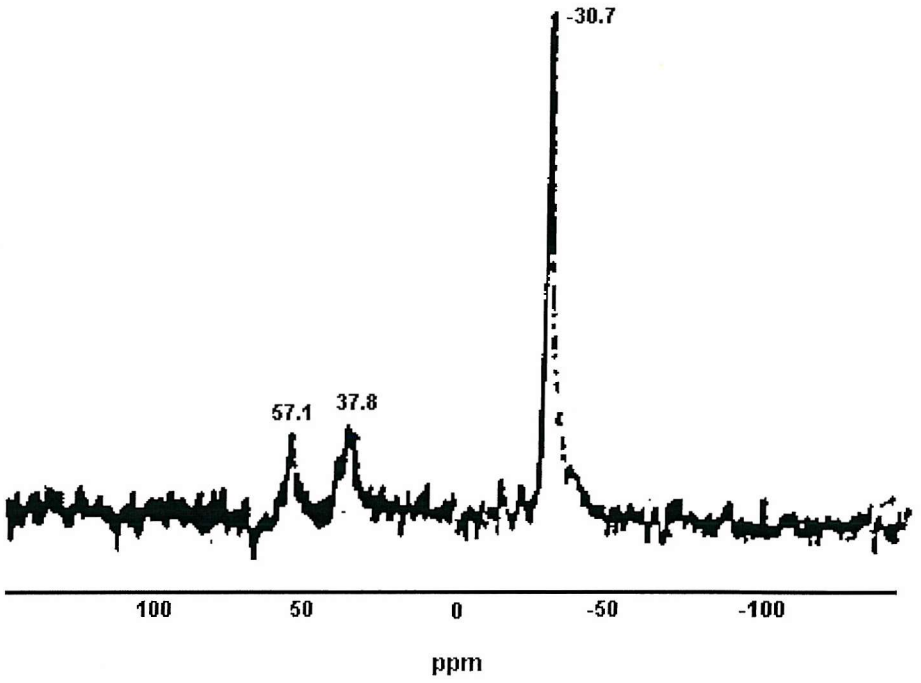

Figure 5.21 ^{31}P MAS NMR (5.2 kHz) of MCM-41(A) functionalized with $P(C_3H_6OH)_3$

By using tri-functional phosphine ligands, the object is to increase the area covered by the phosphine, thereby increasing the potential linkage to the silica surface and leaving less silanol sites for side reactions to take place with. Attempts were made to functionalize MESLC and KMES silicas with (trihydroxypropyl)phosphine and the characterisation of these materials yielded very similar results to those presented here, however, the cleanest reaction seemed to occur with MCM-41(A) so this was used to support the organopalladium species.

5.5 EXAFS study of the MCM-41(A)/P(C_3H_6OH)$_3$/Pd(PPh_3)$_4$ system

Tetrakis(triphenylphosphine)palladium(0) [Pd(PPh_3)$_4$] is a well known catalyst used in coupling reactions such as the coupling of phenyltellurotris(trimethylsilyl)silane with chloroformates to form (aryltelluro)formates[32] and the heteroannulation of vinylic compounds.[33] The immobilization of Pd(PPh_3)$_4$ on the phosphine-functionalized MCM-41(A) was investigated by EXAFS. The reaction was expected to take place via the loss of a single triphenylphosphine ligand to form a chemical bond between the palladium centre and the phosphorus atom of the immobilized phosphine (figure 5.22).

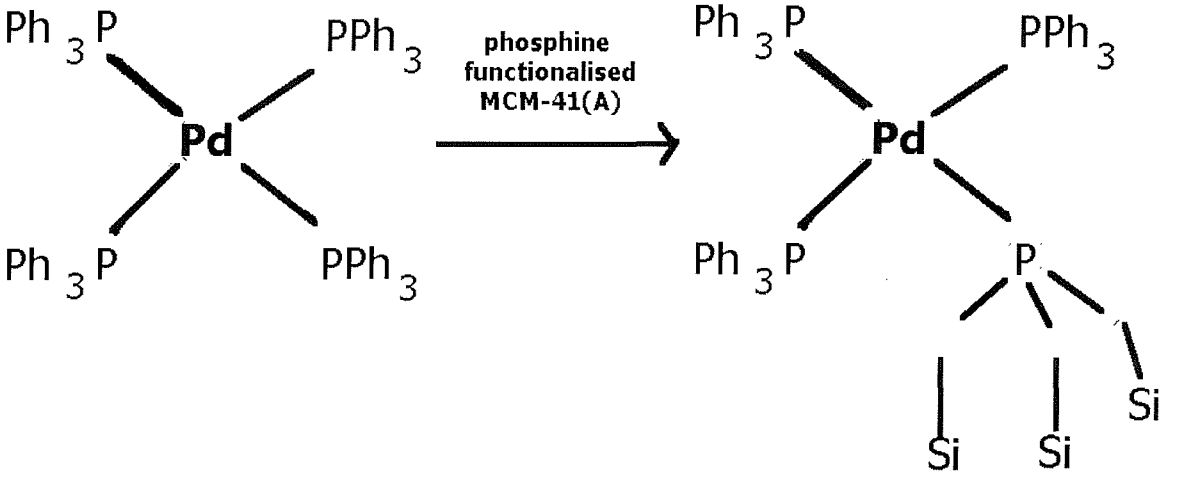

Figure 5.22 Reaction of Pd(PPh_3)$_4$ with phosphine functionalised silica

Synthesis

All manipulations of both the functionalized silica and the air-sensitive organopalladium complex were carried out in a glove box. MCM-41(A) functionalized with P(C_3H_6OH)$_3$ [0.1 g] was mixed with dry toluene (10 ml) to form a suspension. Commercially available Pd(PPh_3)$_4$ [0.01 g, 8.65 x 10^{-6} mol] was mixed with dry toluene (10 ml) and the resulting solution was added to the silica suspension. The mixture was stirred overnight and then the

solvent layer was removed. Fresh, dry toluene (10 ml) was added and the mixture was filtered, the residue was dried under vacuum for several hours. The sample was then Soxhlet-extracted with dry, degassed acetonitrile, dried under vacuum and the resulting yellow-white solid (0.12 g) was stored in an inert atmosphere.

Characterisation

Transmission electron micrographs of MCM-41(A)/P($C_3H_6OH)_3$/Pd($PPh_3)_4$ showed characteristic hexagonal mesostructure and the pore diameter was measured from enlarged photographs as 23.5 Å. The BET surface area measurement was 1656 m^2g^{-1} which is considerably higher than both those obtained for unmodified silica (1422 m^2g^{-1}) and phosphine functionalized silica (1376 m^2g^{-1}). This could be due to the presence of the bulky organopalladium species anchored to the functionalized silica surface but it is impossible at this level to be certain. The palladium loading was determined by AAS as 1.6 weight% Pd.

EXAFS analysis

Figure 5.23 shows the EXAFS spectrum and its Fourier transform of Pd($PPh_3)_4$/BN (10 weight% BN) which was prepared and loaded onto aluminium sample holders in a glove box. Analysis of the data resulted in a first coordination sphere of four phosphorus atoms at 2.404(3) Å corresponding to the phosphorus atoms of the triphenylphosphine ligand. This is comparable with literature values for palladium to phosphorus interatomic distances of 2.293 Å[34] in $Pd_2(Se_2C_2R_2)(PPh_3)_2$, 2.337 Å in $Pd(PPh_3)_2Cl_2$[35] and 2.247 Å in $PdCl_2(R)(PPh_3)$.[36] It was also possible to fit a statistically significant second shell of four carbon atoms at 3.73(8) Å which was due to the phenyl groups on the ligands. The fit resulted in characteristic Debye-Waller values and an R-factor 42.7%.

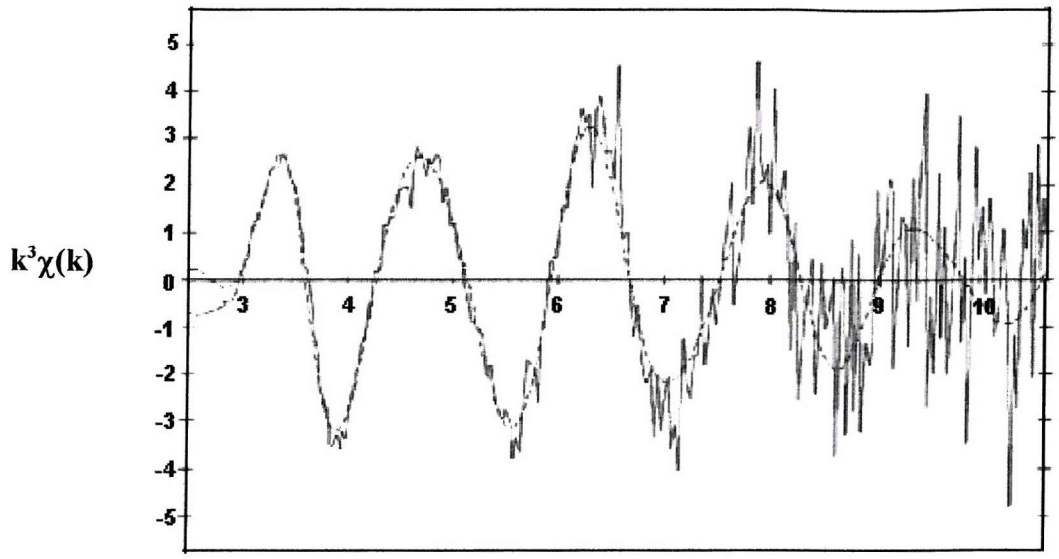

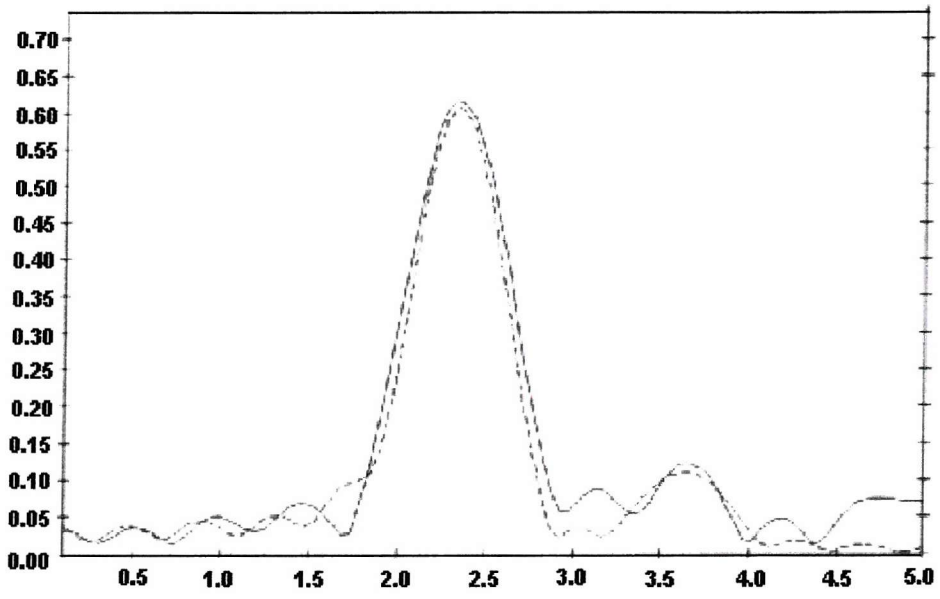

Figure 5.23 Pd K-edge k^3-weighted EXAFS data and Fourier transform of $Pd(PPh_3)_4$/BN phase shift corrected for P.

(— Experimental, ----- Theory)

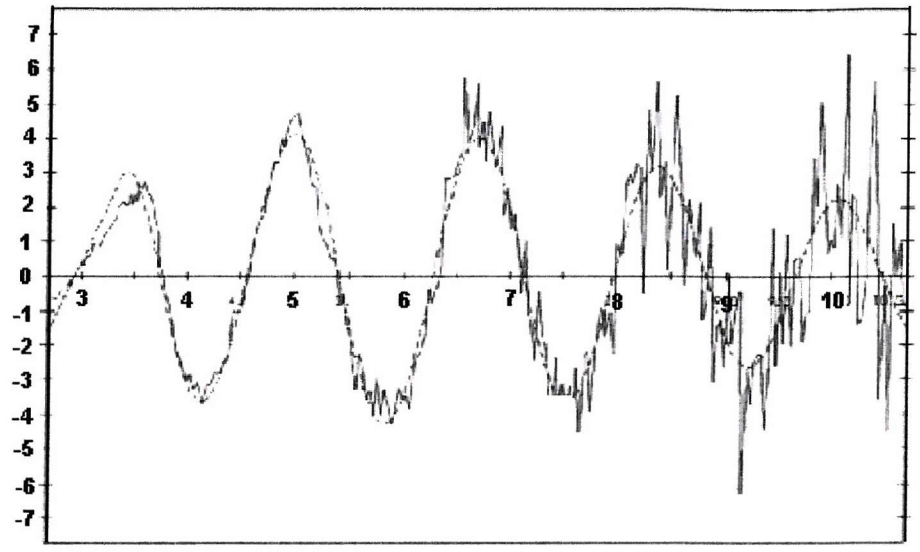

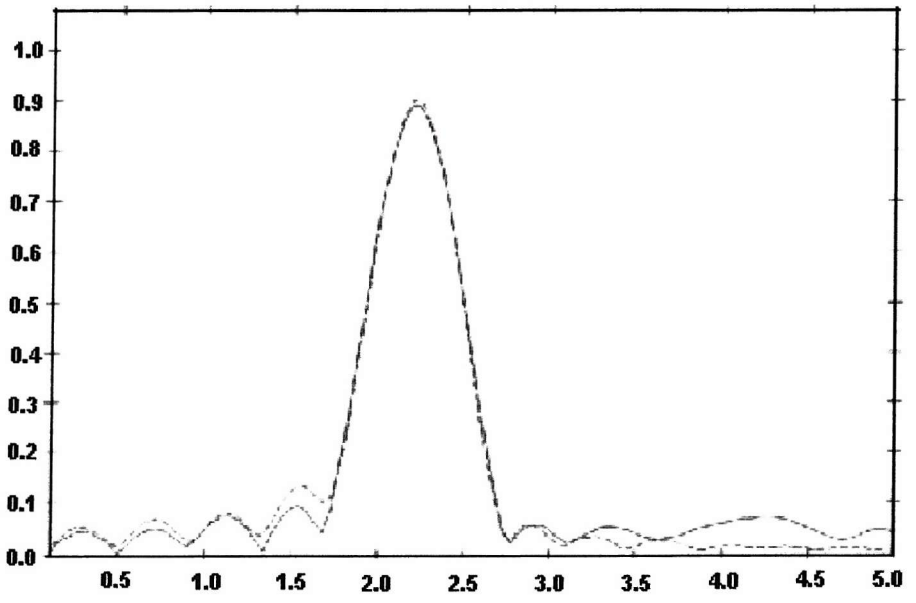

Figure 5.24 Pd K-edge k^3-weighted EXAFS data and Fourier transform of MCM-41(A)/P($C_3H_6OH)_3$/Pd($PPh_3)_4$, phase shift corrected for P. (— Experimental, ----- Theory)

	N[a]	R/Å	A/Å^{2b}
$Pd(PPh_3)_4/BN$ *R-factor = 42.7%*	4P 4C	2.404(3) 3.73(8)	0.020(1) 0.016(3)
$MCM\text{-}41(A)/P(C_3H_6OH)_3/Pd(PPh_3)_4$ *R-factor = 36.5%*	4P	2.393(7)	0.006(2)

[a]Coordination number; [b]Debye-Waller factor $A = 2\sigma^2$, σ = mean square internuclear separation. Statistical errors derived in Excurve92 given in parentheses.

Table 5.6 EXAFS derived structural parameters for $Pd(PPh_3)_4$ anchored on $P(C_3H_6OH)_3$-functionalized MCM-41(A).

The EXAFS spectrum and its Fourier transform of $Pd(PPh_3)_4$ supported on phosphine functionalized MCM-41(A) is presented in figure 5.24. It was only possible to fit this data to a single shell of four phosphorous atoms at 2.393(7) Å with an R-factor of 36.5%. In attempting to identify a different phosphorous environment the data was also modelled to 2 shells of phosphorous atoms but although the second shell was statistically significant and the Debye-Waller values were acceptable, the interatomic bond distances for the two phosphorus environments were too similar to categorically assume two different environments. An attempt was made to model the data to include the different carbon environments of the triphenylphosphine groups and the propyl backbone of the phosphine ligand but this proved unsuccessful. The EXAFS derived structural parameters for the supported and unsupported organopalladium complex are listed in table 5.6.

5.6 Conclusions

Mesoporous silicas MCM-41(A), KMES and MESLC were modified with Pd(allyl)cp in vapour phase reactions and the resulting materials were characterized by a combination of EXAFS, transmission electron microscopy, BET surface area measurements and AAS. The environment around the palladium centre of each supported complex was investigated by

EXAFS analysis and this confirmed the loss of the ally group to leave Pd-cp units anchored to the surface of MCM-41(A) and KMES via two oxygen interactions and a Pd-cp unit attached to the surface of MESLC via one oxygen interaction. The silica MCM-41(A) modified with Pd(allyl)cp was studied *in situ* by EXAFS over a range of temperatures and in the presence of diethylzinc. From room temperature to 120°C, under vacuum, the Pd-cp unit formed stable links to the silica surface via two silanol groups. The addition of diethylzinc to the system at 100°C had no impact on the validity of this structure and in itself reacted with the silica surface via three silanol groups. On increasing the temperature to 180°C some of the Pd-cp units decomposed to leave metallic palladium particles on the surface of the silica.

MCM-41(A) was modified with $Pd(CH_3CN)_2(NO_2)Cl$ and studied by EXAFS at 25°C and at 100°C in the presence of trimethylgallium. At 25°C the system exhibited the loss of two acetonitrile groups resulting in the remaining $Pd(NO_2)Cl$ subunits anchored to the surface of the silica via two silanol groups. The addition of trimethylgallium to the system at 100°C resulted in the decomposition of the organometallic species to metallic palladium. the trimethylgallium vapour also reacted with the silica surface forming a dimethylgallium species linked to the silica surface via two silanol groups

An attempt was made to functionalize MCM-41(A) silica with tri(hydroxypropyl)phosphine. The resulting material was characterized using a combination of MAS NMR, transmission electron microscopy and BET surface area measurements and was found to have hexagonal channels of 22-25 Å, a surface area of 1376 m^2g^{-1} and a mixture of phosphorus environments. The phosphine-functionalized silica was then further reacted with $Pd(PPh_3)_4$ and this system was studied by EXAFS to investigate the possible use of tri-functional phosphine ligands to act as linkers between the surface of the silicas and the organometallic species. The results proved inconclusive as it was not possible to model the data beyond a first co-ordination sphere of phosphorous atoms.

5.7 References

1. Lindner, E., Glaser, E., Mayer, H. A., Wegner, P., *J. Organomet. Chem.*, 1990, **398**, 323.
2. Allum, K.G., Hankock, R. D., Howell, N., McKenzie, S., Pitkethly, R. C., Robinson, P.J., *J. Organomet. Chem.*, 1975, **87**, 203.
3. Liu, D. K., Wrighton, M.S., McKay, D. R., Maciel, G. E., *Inorg. Chem.*, 1984, **23**, 212.
4. Rocha, J., Welch, M. D., Klinowski, J., *J. Am. Chem. Soc.*, 1991, **113**, 7100.
5. Grennberg, H., Gogoll, A., Backvall, J.-E., *Organometallics*, 1993, **12**, 1790.
6. Backvall, J.-E., Hopkins, R. B., Grennberg, H., Mader, M. M., Awasthi, A. K., *J. Am. Chem. Soc.*, 1990, **112**, 5160.
7. Deganello, G., Duca, D., Liotta, L. F., Martorana, A., Venezia, A. M., Benedetti, A., Fagherazz, G., *J. Catal.*, 1995, **151**, 125.
8. Backvall, J.-E., *Pure & Applied Chemistry*, 1992, **64**, 429.
9. Tatsumi, T., Yuasa, K., Tominaga, H., *J. Chem. Soc., Chem. Commun.*, 1992, 1446.
10. Backvall, J.-E., *Acc. Chem. Res.*, 1983, **16**, 335.
11. Tatsuno, Y., Yoshida, T., Seiotsuka, N., *Inorg. Synth.*, 1979, **19**, 217.
12. Minasyan, M., *Zh. Strukt Khim.*, 1966, **7**, 906.
13. Moore, W. J., Jr. and Pauling, L., *J. Am. Chem. Soc.*, 1941, **63**, 1392.
14. Andrews, M. A., Cheng, C. W. F., *J. Am. Chem. Soc.*, 1982, **104**, 4268.
15. Andrews, M. A., Chang, T. C. T., Cheng, C. W. F., Kelly, K. P., *Organometallics*, 1984, **3**, 1777.
16. Wendt, O. F., Kaiser, N.-F. K., Elding, L. I., *J. Chem. Soc., Dalton Trans.*, 1997, 4733.
17. Gebauer, T., Frenzen, G., Dehnicke, K., *Z. Naturforsch. Teil B*, 1992, **47**, 1505.
18. Keirs, N. H., Feringa, B. L., Kooijman, H., Spek, A. L., van Leeuwen, P. W. N. M., *J. Chem. Soc., Chem. Commun.*, 1992, 1169.
19. Kili, K., Hilaire, L., Le Normand, F., *Phys. Chem. Chem. Phys.*, 1999, **1**, 1623.
20. Blumel, J., *Inorg. Chem.*, 1994, **33**, 5050.
21. Capka, M., *Syn. React. Inorg. Met. Org. Chem.*, 1977, **7**, 347.

22. Bezombes, J.-P., Chuit, C., Corriu, R. J. P., Reye, C., *J. Mater. Chem.*, 1999, **9**, 1727.
23. Corriu, R. J. P., Hoarau, C., Mehdi, A., Reye, C., *Chem. Commun.*, 2000, 71.
24. Engelhardt, G., *Introduction to Zeolite Science and Practice*, van Bekkum, H., Flanigen, E. M., Jansen, J.C., (Eds.), Elsevier, 1991, **58**, 285.
25. Grobet, P.J., Geerts, H., Martens, J. A., Jacobs, P. A., *Recent Advances in Zeolite Science*, Klinowski, J., Barrie, P. J., (Eds.), Elsevier, 1989, **52**, 193.
26. Akolekar, D. B., Howe, R. F., *J. Chem. Soc., Faraday Trans.*, 1997, **93**, 3263.
27. Slinn, R. N., Salt, M. C., *Organophosphorus Chemistry*, The Royal Society of Chemistry, 1999, **29**, 300.
28. Bezombes, J.-P., Chuit, C., Corriu, R. J. P., Reye, C., *J. Mater. Chem.*, 1998, **8**, 1749.
29. Bookham, J. L., Smithies, D. M., Wright, A., Thornton-Pett, M., McFarlane, W., *J. Chem. Soc., Dalton Trans.*, 1998, 811.
30. Smith, C. J., Reddy, V. S., Katti, K. V., *J. Chem. Soc., Dalton Trans.*, 1998, 1365.
31. Bemi, L., Clark, H. C., Davies, J. A., Fyfe, C. A., Wasylishen, E., *J. Am. Chem. Soc.*, 1982, **104**, 438.
32. Schiesser, C. H., Skidmore, M. A., *J. Chem. Soc., Perkins Trans. 1*, 1997, **18**, 3555.
33. Mahanty, J. S., De, M., Kunda, N. G., *Chem. Soc., Perkins Trans. 1*, 1997, **17**, 2577.
34. Ford, S., Khanna, P. K., Morley, C. P., Di Vaira, M., *J. Chem. Soc., Dalton Trans.*, 1999, 791.
35. Fawcett, J., Hope, E. G., Kemmitt, D. W., Paige, D. R., Russell, D. R., Stuart, A. M., *J. Chem. Soc., Dalton Trans.*, 1998, 3751.
36. Albert, J., Gonzalez, A., Granell, J., Moragas, R., Solans, X., Font-Bardia, M., *J. Chem. Soc., Dalton Trans.*, 1998, 1781.

Appendix One - Additional Experimental Methods

Infra-red Spectrometry

IR spectra of MCM-41(A) and MCM-41(B) were recorded in transmission mode on a Perkin Elmer FTIR spectrometer from 400-4000 cm^{-1}. Silica samples were dehydrated under vacuum at 200°C for 2 h and then loaded into a disk press in a glove box. The press was placed under pressure (>1500 psi) and the resulting disk was placed in the sample holder of a purpose built IR cell (figure A1) which could be heated to 500°C and allowed a vacuum to be applied.

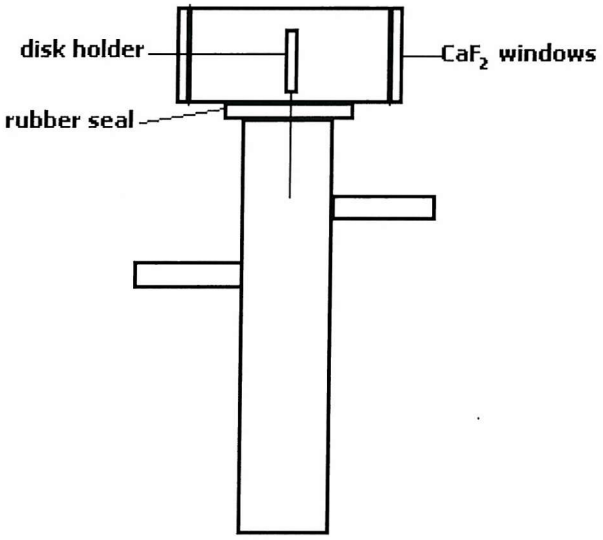

Figure A1 Infrared cell

Powder X-ray Diffraction

Powder X-ray diffraction was mainly used as a fingerprint technique to verify the presence of a hexagonal lattice in the mesoporous materials. The powder X-ray diffraction data was collected on a Siemens θ-2θ D5000 diffractometer and was managed using the SIEMENS DIFFRAC 500 software package.

Appendix Two - BET Data Printout

BET surface area measurements were performed on a Micromeritics Gemini 2375 analyser relative to an empty tube at 77.5 K. The sample was evacuated for 15 min, and then 10 measurements were taken at 10 adsorb pressures and 10 desorb pressures with 5 s intervals for equilibrium to take place. The data printout for a typical mesoporous material can be seen in A2.

Gemini 2375 V1.01
Instrument ID: 444

Sample ID: 20
Sample Weight: 0.0637 g
Evacuation Rate: 500.0 mmHg/min
No Free Space Correction Applied
Analysis Mode: Equilibration

Started: 29/03/95 13:12:15
Completed: 29/03/95 17:19:57
Evacuation Time: 15.0 min
Saturation Pressure: 760.00 mmHg
Equilibration Time: 5 sec

BET Multipoint Surface Area Report

Surface Area:	1182.6089 sq. m/g
Slope:	0.003424
Y-Intercept:	0.000257
C:	14.341968
Vm:	271.664337
Correlation Coefficient:	9.7395e-001

Analysis Log

Relative Pressure	Pressure (mmHg)	Vol. Adsorbed (cc/g STP)	Elapsed Time (h:m)	Surface Area Point
0.0301	22.89	145.608	0:22	
0.0601	45.69	168.713	0:30	*
0.0901	68.51	185.757	0:38	*
0.1202	91.33	200.435	0:46	*
0.1502	114.17	214.621	0:54	*
0.1803	136.99	229.739	1:03	*
0.2103	159.82	251.213	1:52	*
0.2403	182.65	287.986	1:30	*
0.2704	205.49	333.765	1:52	*
0.3004	228.30	351.465	2:01	*
0.2911	221.23	350.005	2:08	
0.2706	205.68	337.089	2:23	
0.2406	182.84	291.543	2:54	
0.2106	160.02	251.524	3:14	
0.1805	137.18	229.558	3:25	
0.1505	114.36	214.632	3:33	
0.1204	92.52	200.409	3:40	
0.0904	68.70	185.817	3:47	
0.604	45.88	169.006	3:59	
0.0304	23.08	145.970	4:07	

A2 BET data printout for a typical mesoporous silica